



PONTIFICIA UNIVERSIDAD CATOLICA DE CHILE
SCHOOL OF ENGINEERING

**NUMERICAL AND EXPERIMENTAL
MODELING OF EXTREME FLOOD WAVES
AND INUNDATION ZONES**

MARICARMEN GUERRA PARÍS

Thesis submitted to the Office of Research and Graduate Studies
in partial fulfillment of the requirements for the degree of
Master of Science in Engineering

Advisor:
RODRIGO CIENFUEGOS

Santiago de Chile, August 11th, 2010

© MMX, MARICARMEN GUERRA PARÍS



PONTIFICIA UNIVERSIDAD CATOLICA DE CHILE
SCHOOL OF ENGINEERING

**NUMERICAL AND EXPERIMENTAL
MODELING OF EXTREME FLOOD WAVES
AND INUNDATION ZONES**

MARICARMEN GUERRA PARÍS

Members of the Committee:

RODRIGO CIENFUEGOS

CRISTIÁN ESCAURIAZA

OSCAR LINK

MARIO DURÁN

.....

Thesis submitted to the Office of Research and Graduate Studies
in partial fulfillment of the requirements for the degree of
Master of Science in Engineering

Santiago de Chile, August 11th, 2010

© MMX, MARICARMEN GUERRA PARÍS

Gratefully to my parents

ACKNOWLEDGEMENTS

First of all I would like to thank my family for the constant support through the university years, during the undergraduate and graduate programs. They always have been right next to me, giving me the strength to accomplish my goals and encouraging me to do the best that I can.

I express my sincere recognition to my thesis advisor Rodrigo Cienfuegos. Thanks for believing and trusting in me, and for giving me the opportunity to work on this thesis. Rodrigo has been a great teacher, always proposing challenging new ideas and having great expectations about this work. I hope that all students can have the opportunity to have such a good advisor.

I'm also grateful to my co-advisor Cristian Escauriaza. His great motivating spirit is truly encouraging. I thank him for his constant interest on this work and all his great ideas, and for never let me do less than what I can.

Many thanks also to Fabien Marche, from Montpellier 2 University, who shared his work and knowledge with me, and help me through the development of the numerical model. Also, I'm very grateful for invited me to the 2nd Workshop of Mathematics and Oceanography in Montpellier, France.

Especial thanks to all of my “colleagues” and friends of the Hydraulic and Environmental Engineering Department, to many to name them all. Thank you for all the nice moments in the *Norht and South Wings* and at lunch time. Thanks for making hard work and research something fun, and for sharing crazy ideas and your happiness.

I also want to recognize my dear friends, who have become my family during this last 7 years, Cami and Euge, thank you for your support, for your trust, for listen to me, for give me advice, for encourage me to finish this thesis, and for everything that you and your families have given to me. Also I want to thanks to my forever friends Angela, Gaby, Nato, Felo, Tincho and Cristian, with whom I have grown and always enjoy life. They might not

understand at all what this work was about, but they have always been there to encourage me and to make me feel proud about it.

Finally, I want to thank the Arturo Cousiño Lyon scholarship and the financial aid provided by the Fondecyt project N°11060312, the ECOS-Conicyt project C07U01 and the IAHR-PUC student chapter. Also, acknowledge the measurement devices provided by the *Instituto Nacional de Hidráulica* and the help, technical support and interest of Enrique Rosa. At last, I especially thank everyone who helped to carry out the Dam-break laboratory experience.

TABLE OF CONTENTS

ACKNOWLEDGEMENTS	iv
LIST OF FIGURES	ix
ABSTRACT	xii
RESUMEN	xiii
1. INTRODUCTION	1
1.1. Methodology	6
1.1.1. Governing Equations	6
1.1.2. Numerical Method	7
1.1.3. Application	8
1.2. Thesis Outline	8
2. A curvilinear Finite Volume Model for shallow inertial flows including bathymetric variations, bottom friction and run-up	10
2.1. Abstract	10
2.2. Introduction	11
2.3. Governing Equations	13
2.4. Numerical Scheme	16
2.4.1. Semi-Implicit Friction Step	16
2.4.2. Hyperbolic NSWE Step	19
2.4.3. Boundary Conditions	27
2.4.4. Stability Criterion	28
2.5. Validation of the Model	29
2.5.1. Radial Dam-Break	29
2.5.2. Supercritical flow in a convergent channel	30
2.5.3. 1D Oscillating water column over a parabolic basin with friction	35

2.6. Conclusions	36
2.7. Acknowledgements	39
3. Physical and Numerical Modeling of Inertia-Dominated Flood Waves	40
3.1. Abstract	40
3.2. Introduction	41
3.3. Methods	43
3.3.1. Experimental Set-Up	43
3.3.2. Post-Processing of the data	45
3.3.3. Numerical Modeling	47
3.4. Results	49
3.5. Conclusions	51
3.6. Acknowledgements	53
4. CONCLUSION AND FUTURE PERSPECTIVES	54
REFERENCES	56
APPENDIX A. SHALLOW WATER EQUATIONS	61
A.1. Non-linear Shallow Equations	61
A.2. Dimensionless NSWE	62
A.2.1. Dimensional Scales	62
A.2.2. Dimensionless Equations	62
APPENDIX B. CURVILINEAR SWE	65
B.1. Generalized Curvilinear Coordinate System	65
B.1.1. Some Properties of the (ξ, η) system	65
B.1.2. Covariant and Contravariant Components of a Cartesian vector	66
B.2. Curvilinear NSWE	68
APPENDIX C. NON-CONSERVATIVE FORM OF THE CURVILINEAR NSWE	71
C.1. Non-Conservative form of the curvilinear NSWE	71
C.2. Eigenvalues of Jacobian matrices	73

APPENDIX D. THE VF <small>Roe</small> -ncv APPROXIMATE RIEMANN SOLVER	75
D.1. Formalism of the VF <small>Roe</small> -ncv scheme	75
APPENDIX E. WELL-BALANCED NUMERICAL SCHEME	77
E.1. 1st Order Hydrostatic Reconstruction	78
E.2. 2nd Order Hydrostatic Reconstruction	83
APPENDIX F. BOUNDARY CONDITIONS	87
F.1. Reflective solid wall	87
F.2. Transmissive boundary	88
F.3. Periodic boundary condition	88
F.4. Absorbing/Generating Boundary Condition	89
F.5. Ghost Cells Bathymetry	93
APPENDIX G. TIME INTEGRATION METHOD	94
APPENDIX H. BENCHMARK CASES	95
H.1. Steady State at rest	95
H.2. 1D Dam-break	96
H.3. 2D Dam-break	97
H.4. Thacker's curved solution	99

LIST OF FIGURES

1.1 Flow variables	3
1.2 Illustration of a Riemann problem	3
1.3 Illustration of a finite volume method for updating the cell-averaged value Q_i . .	4
1.4 Real domain (x, y) and transformed computational domain (ξ, η)	6
2.1 Schematic drawing of hydrodynamic variables and characteristic scales	14
2.2 Numerical Scheme: Flux Diagram for each time-step	17
2.3 Discretization cell and numerical fluxes	20
2.4 Radial dam-break. Discretization grids: (a) Cartesian grid, (b) Curvilinear grid .	30
2.5 Radial dam-break. Contour plot of computed free surface at $t=0.7$ s, (a) Using cartesian grid, (b) Using curvilinear grid	31
2.6 Radial dam-break. Computed velocity field at $t=0.7$ s, (a) Using cartesian grid, (b) Using curvilinear grid	31
2.7 Convergent channel. Geometry of the channel	32
2.8 Convergent channel. Boundary-fitted grid	33
2.9 Convergent channel. Steady state wave pattern. (a) & (b) Laboratory Experiments of Ippen and Dawson (1951), (c) & (d) Computed free surface	33
2.10 Convergent channel. Measured and computed water depths at steady state, (a) along the sidewall, (b) along the middle of the channel section	34
2.11 1D Oscillating water column. Free surface at different times	37
2.12 1D Oscillating water column. Time series for the water depth at $X = 2400$ m . .	38
3.1 Dam-break Experience: Longitudinal profile of the river reach bottom elevation, initial conditions and measurement points	43
3.2 Dam-break Experience: (a) Physical Model, (b) Experimental Set-up and Reservoir	44

3.3 Dam-break Experience: Resistive Gauges	44
3.4 Time Series of Free surface Measurements at different locations: (a) Reservoir, (b) Point 23, (c) Point 20, (d) Point 12	46
3.5 Dam-break Experience: Digital physical model bathymetry	49
3.6 Dam-break Experience: Effects of the dam-break over the river free surface at $t = 3.1$ s	50
3.7 Comparison between measured and predicted free surface elevation at different locations: (a) Reservoir, (b) Point 23, (c) Point 20, (d) Point 12	51
3.8 Comparison between measured and predicted results: (a) Arrival Time, (b) Maximum free surface elevation, (c) Volume of water per unit area	52
 B.1 Covariant and Contravariant Basis	67
E.1 Discretización en la celda i-ésima	78
E.2 Schematic drawing of the <i>Minmod</i> reconstruction method, Marche (2005) . . .	83
F.1 Schematic computational domain including ghost cells, Marche (2005)	87
F.2 Absorbing/Generating boundary condition scheme, Cienfuegos et al. (2007) . .	90
F.3 Absorbing/Generating boundary condition meshes	91
 H.1 Estado Estacionario: Batimetría y Condiciones Iniciales	95
H.2 Estado Estacionario $t=200$ s: (a) Corte transversal, (b) Serie de Tiempo de Caudal en $(x, y) = (0, 0)$	96
H.3 1D Dam-break: Schematic drawing of the initial conditions	97
H.4 1D Dam-break: Free surface profiles at different times	97
H.5 1D Dam-break: (a) Velocity profiles, (b) Discharge per unit width profiles . . .	98
H.6 2D dam-break: Schematic plan view of the domain	98
H.7 2D Dam-break, 7.2 s after breaking: (a) 3D view of the free surface elevation, (b) Contour map of the free surface	99

H.8	2D Dam-break: Velocity field	99
H.9	Thacker's curved solution: Parabolic basin	100
H.10	Thacker's curved solution: Geometry of the problem, Marche et al. (2007) . . .	101
H.11	Thacker's curved solution: Numerical and analytical solutions of the free surface in the center line of the basin at times: (a) $3T$, (b) $3T+T/6$, (c) $3T+T/3$, (d) $3T+T/2$	102
H.12	Thacker's curved solution: Zoom view of the shoreline	102

ABSTRACT

Nowdays, the increasing frequency of extreme and rapid floods caused by winter storms, glacial lake outburst floods or tsunamis, makes necessary to quantify associated hydrodynamic variables, such as water depth and velocity, in order to evaluate its consequences and to be able to elaborate appropriate action plans. This kind of events can be modeled through the shallow water equations, which have been commonly used to describe the dynamic of open flows, such as rivers, lakes and near-shore flow. The aim of this thesis is to obtain a robust tool capable of representing extreme and rapid flooding over complex geometries. An extended version in curvilinear coordinates of the SURF_WB model (Marche et al., 2007) is developed including bed-slope and friction source terms. The numerical model has shock-capturing ability, it correctly manages the wetting and drying processes, and preserves steady states at rest. Several validation tests have been simulated, involving complex geometries, strongly variable topography and moving shoreline problems. Excellent agreement is found when compared with analytical, experimental and other numerical data. Also, laboratory dam-break experiences were performed over a 1:60 scaled physical model of a river, in order to prove the abilities of the new model when simulating an extreme event over realistic topography.

This document presents the complete development of the numerical model and its validation with different benchmark cases. The details of the dam-break laboratory experience and the results of its simulation with the new numerical model are also presented. The numerical results show that the new model is capable of reproducing flooding processes and improvement is found when using a boundary-fitted discretization of the domain.

Keywords: Shallow water equations, finite volume schemes, well-balanced, shock capturing, boundary-fitted coordinates, floods.

RESUMEN

Actualmente, el aumento en la frecuencia de crecidas rápidas y extremas causadas por lluvias invernales, vaciamiento de lagos o tsunamis, hace necesario el cuantificar las variables hidrodinámicas asociadas, como altura de aguas y velocidad, con el objeto de evaluar sus consecuencias y poder elaborar planes de acción adecuados. Este tipo de eventos puede ser modelado utilizando las ecuaciones de aguas someras, las que son comúnmente usadas para describir la dinámica de escurrimientos abiertos, como ríos, lagos o el flujo en zonas cercanas a la línea de costa. El objetivo de esta tesis es obtener una herramienta robusta capaz de representar crecidas rápidas y extremas sobre topografías complejas. Se ha desarrollado una versión extendida en coordenadas curvilíneas del modelo SURF_WB (Marche et al., 2007), incluyendo términos fuente asociados a pendiente y a fricción de fondo. El modelo numérico tiene la habilidad de capturar shocks, manejar la interface seco-mojada y preservar los estados estacionarios. Varios casos de validación han sido simulados, incluyendo geometrías compejas, topografía fuertemente variable y línea de costa móvil, econtrándose excelentes resultados al comparar con soluciones analíticas, de laboratorio y otras soluciones numéricas. Además, se llevaron a cabo experiencias de vaciamiento de estanque en laboratorio, sobre un modelo físico de río a escala 1:60 para probar las habilidades del nuevo modelo al simular un evento extremo sobre topografía real.

Este documento presenta el desarrollo completo del modelo numérico y los casos de validación aplicados. Los detalles de la experiencia de laboratorio y los resultados de la simulación hecha con el modelo son también mostrados. Los resultados obtenidos muestran que el modelo es una herramienta robusta capaz de representar los procesos de inundación y mejoras son obtenidas al utilizar una discretización ajustada a la forma del dominio de estudio.

Palabras Claves: Ecuaciones de Aguas Someras, volúmenes Finitos, esquemas bien-balanceados, captura de shocks, coordenadas curvilíneas generalizadas, inundaciones.

1. INTRODUCTION

Numerical modeling plays an important role in all engineering disciplines owing to its rapid development, mostly due to the improvement of numerical methods and computational capabilities. In hydraulic engineering, numerical simulation of free surface flows covers a wide variety of applications, such as the design of river and coastal structures, environmental and hydrological studies, ocean circulation, etc.

Nowdays, there is an increasing need to predict the hydrodynamics of natural free surface flows, such as winter flooding, tsunamis, Glacial Lake Outburst Flood (GLOF), dam-breaks, wave propagation under extreme conditions, among many others. Mayor events, such as the Malpasset dam-break in 1959 in the south of France, the current winter floods in the areas of the Three Gorges dam in China, the recent GLOFs in the Aysén region in southern Chile or the February 27, 2010, tsunami along the Chilean coast, demonstrate the important consequences of these extreme events on both, economics and social costs.

These costs could be diminished if better predictions of the behaviour of the flow and its main variables (maximum water height, run-up and velocities) were available. Indeed, a good estimation of the flow features can lead to: better design of associated structures and hydraulic facilities, definition of risk zones, mitigation and evacuation plans in urbanized zones that could be at risk.

Most of the examples listed above can be classified as shallow inertial flows (Hogg & Pritchard, 2004), since inertial forces are more important than gravitational. To model those flows, advanced mathematical and numerical techniques are needed, since in its development a large number of discontinuities may appear (hydraulic jumps, breaking, wetting-drying).

When the typical wavelength of the flow is much bigger than the typical water depth, the Nonlinear Shallow Water Equations (NSWE), which describe the hydrodynamics in terms of water height variations and depth-averaged velocities, can be employed. These equations express the conservation of mass and momentum assuming that the fluid is homogeneous, incompressible and inviscid; and the long wave hypothesis implies that there

is a hydrostatic pressure profile in the water column (Cunge, 1991; Stoker, 1992; Toro, 2001). The NSWE are a time-dependant hyperbolic system of partial differential equations and are traditionally written, in a two dimensional Cartesian frame, as:

$$Q_t + F(Q)_x + G(Q)_y = S \quad (1.1)$$

where the subscripts denote partial derivatives with respect to t , x and y , Q is a vector containing the flow variables $Q = [h, hu, hv]$ (water depth h , and discharge per unit area hu and hv , where u and v are the horizontal depth-averaged velocities in each Cartesian direction). F and G account for the mass and conservation fluxes and S , is a source term that should be included to describe bottom variations and friction. In Fig. 1.1 a schematic drawing of the flow variables and geometric configuration of the flow is shown.

The NSWE can be written in a non-conservative form as,

$$Q_t + A(Q)Q_x + B(Q)Q_y = S \quad (1.2)$$

where $A(Q)$ and $B(Q)$ are known as the *Jacobian* matrices corresponding to the fluxes $F(Q)$ and $G(Q)$ (Toro, 2001). Due to the hyperbolic character of this set of conservation laws, the *Jacobian* matrices, A and B , are both diagonalizable and have real eigenvalues and a corresponding set of linearly independent eigenvectors (Leveque, 2002). The corresponding eigenvalues λ_i of A , or B , represent the wave speed at which a wave propagates in a given direction. An unique linear combination of the eigenvectors provides an unique solution to the NSWE, which consist in a linear combination of "waves" traveling at the characteristic speed λ_i (Leveque, 2002).

Although the NSWE seem to be adequate to model shallow inertial flows, analytical solutions exist only for highly simplified cases. The latter implies that for more realistic applications the equations must be solved numerically. Numerical solutions to the NSWE are not trivially found, thus an appropriate numerical scheme that can naturally capture all the complex features must be considered.

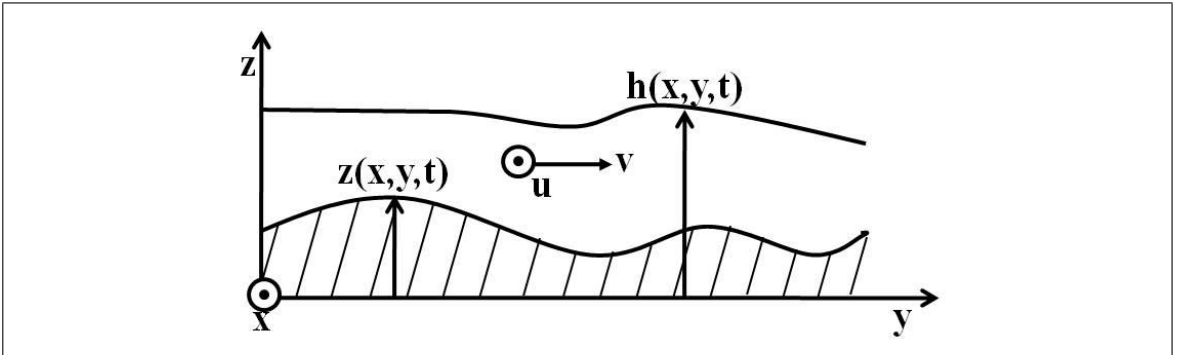


FIGURE 1.1. Flow variables

Finite volume methods, which are based in the integral form of conservation laws, consist in discretizing the physical domain into grid cells, average the total integral of Q over each cell, and then modify its value at each time step by computing the mass and momentum fluxes through the cell faces. The key issue is to accurately compute the flux functions at the boundaries of each cell using approximate cell averages. The flux functions can, for instance, be calculated by solving a **Riemann Problem** at the cell interfaces (Leveque, 2002). A Riemann Problem (RP) is basically defined by a hyperbolic homogeneous equation system plus a piecewise initial condition with a single jump discontinuity, Eq. (1.4). In Fig. 1.2 a schematic representation of a RP is shown.

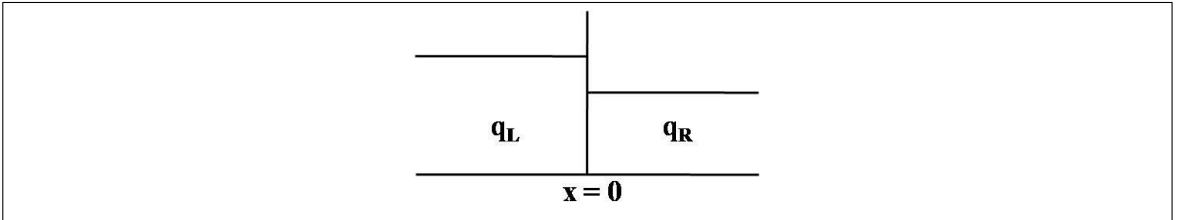


FIGURE 1.2. Illustration of a Riemann problem

$$q_t + f(q)_x = 0 \quad (1.3)$$

$$q(x, 0) = \begin{cases} q_L & si \quad x < 0 \\ q_R & si \quad x > 0 \end{cases}$$

In a finite volume grid, the fluxes through the interface of the $i - 1$ and i cells can be obtained by solving the RP with $Q_{i-1} = q_L$ and $Q_i = q_R$, where the subindices L &

R indicate the left and right states of the cell interface. Finite volumes schemes seeking the exact solution to the RP to calculate the flux function through the cell interface are known as Godunov type methods (Leveque, 2002). Due to the high computational cost of the exact solution of the Riemann problem, a wide range of approximate Riemann solvers have been developed (Toro, 1997, 2001; Leveque, 2002). Approximate Riemann solvers can be classified in two classes (Toro, 2001): i.) Solvers that compute an approximate solution of the RP, then the numerical flux is obtained by evaluating the exact flux function at this approximate state (Roe type schemes; ii.) Solvers that obtain an approximation of the flux directly. For a complete description of these classes of methods see Toro (1997).

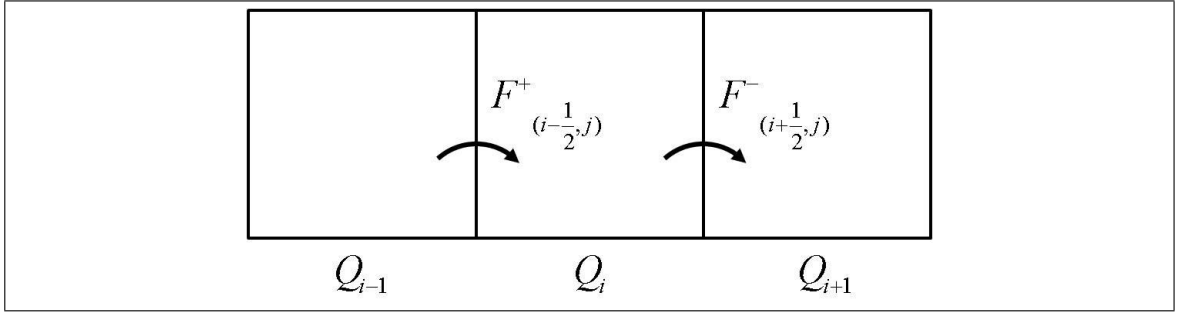


FIGURE 1.3. Illustration of a finite volume method for updating the cell-averaged value Q_i

The NSWE admit solutions that include discontinuities such as shocks (or bores), shear waves and vortices and wet/dry fronts (Toro, 2001). This discontinuous solutions represent the biggest challenge for numerical methods. If the numerical method does not correctly represent, these features the numerical predictions cannot be trustable. For example, numerical shock waves may have incorrect lengths and propagation speeds, thus the arrival time and the wave hydrodynamics will not be well computed. Also, spurious or unphysical oscillations may appear around numerical solutions, which can lead to instabilities, contaminating the solution (Toro, 2001). High resolution finite volume methods based on Riemann solvers can automatically deal with these discontinuities; they appear as a part of the complete solution, without adding any special mathematical technique. These schemes are known as *Shock-capturing* methods (Toro, 2001).

An additional problem that must be addressed when computing shallow water flows is the preservation of steady states at rest. Most of the geophysical flows develop from perturbations of the equilibrium state or converge to it. Thus, the numerical methods must be able to preserve this state in absence of external forces or disbalances. Well-balanced schemes are known for their ability to correctly manage the steady states at rest, they are based in the idea that the equilibrium described by the equations, considering momentum source terms, must be preserved in the numerical scheme that solve the equations. Well-balanced schemes rely in the balance between numerical fluxes and the bed-slope source term in order to accomplish the hydrostatic balance for flow at rest.

Several models have been developed using the techniques mentioned above in a Cartesian coordinate frame (“Greenberg”, n.d.; Gallouet et al., 2003b, 2003a; Audusse et al., 2004; Marche, 2005; Q. Liang & Marche, 2009).

Similarly, the numerical model should also be able to handle complex geometries, since natural shallow inertial flows often occur over rapidly varying topographies with irregular boundaries. Mountain rivers on steep slopes, or irregular shaped shorelines are good examples of these complexities. A rectangular representation of irregular boundaries requires approximations that can introduce large errors in the development of the flow, which can result in numerical instabilities (Shi et al., 2001; Baghlan et al., 2008). To solve those problems, finite volume methods with unstructured meshes or curvilinear meshes are best suited. Unstructured grids are more flexible than structured grids to fit complicated boundaries and deal with very complex geometries. However, structured curvilinear grids have the superiority of the programming simplicity and thus are widely used in Computational Fluid Dynamics (Shi et al., 2001; Baghlan et al., 2008).

The basis of the generalized boundary-fitted curvilinear coordinates method is to use a set of curvilinear grid points in which the boundaries of the domain follow a coordinate line. The mesh lines can be curved and their intersection is not necessarily orthogonal. This approach leads to a better representation of the domain boundaries. A better resolution can be considered in regimes of interest, resulting in a efficient discretization of the

flow domain. The curvilinear coordinate system is defined such that the curvilinear non-orthogonal mesh in the Cartesian plane is converted to a uniform and regular mesh in the transformed domain (Fig. 1.4). In order to use this kind of gridding, the governing equations, which are written for Cartesian variables, must be transformed to the new coordinate system. The equations written under the new set of coordinates can be discretized in a regular and uniform mesh using a suitable finite volume method, at the expense of solving a more complicated set of equations due to the transformation.

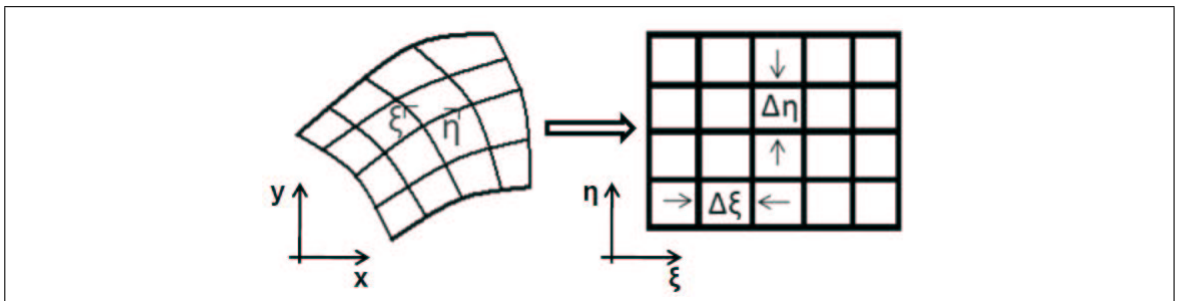


FIGURE 1.4. Real domain (x, y) and transformed computational domain (ξ, η)

The **main objective** of this thesis is to implement a robust tool capable of representing extreme and rapid flooding over complex geometries. In order to accomplish this objective, a numerical model to solve the shallow water equations under a curvilinear coordinate system will be developed, implemented, and validated.

1.1. Methodology

The numerical model developed in this thesis is a finite volume, shock-capturing, well-balance scheme to solve the NSWE written in a curvilinear coordinate system. The following methodology was used to implement and test the numerical model.

1.1.1. Governing Equations

First, the NSWE equations were transformed into the generalized boundary fitted curvilinear coordinate system presented in Bradford and Sanders (2002); Lackey and Sotiropoulos (2005); Loose et al. (2005). The coordinate transformation is partial, as the main flow variables, water depth and Cartesian velocities remain after the change of coordinates. The

transformation was done using the chain rule to expand the derivatives in terms of the new set of coordinates; the new set of equations is shown in Chapter 2 of this thesis and the details of the transformation can be found in Appendix B. The NSWE solved considered only friction and bed-slope source terms.

1.1.2. Numerical Method

The numerical model to be implemented in the NSWE is an extension of the SURF_WB model developed by Marche (2005). SURF_WB model is a Godunov-type finite volume scheme for the two-dimensional NSWE written in Cartesian coordinates with a bed-slope source term. It was first intended to simulate wave transformation over strongly varying topography. The model relies in the hydrostatic reconstruction method proposed by Audusse et al. (2004) to treat the bed-slope source term, and in the VFroe-ncv approximate Riemann solver (Gallouet et al., 2003b). This high-resolution numerical scheme is second order accuracy in space and fourth order in time. It has shock-capturing ability, is able to handle strong topography variations, preserves steady states at rest and can also deal with wet/dry fronts. It has been validated against several analytical solutions, involving varying topography, time dependant moving shorelines and convergence towards steady state (Marche et al., 2007). The friction source term was included in the numerical solutions using the splitting implicit recently proposed by Q. Liang and Marche (2009). The numerical algorithm was then computationally implemented and written in FORTRAN 90 programming language.

Several validation tests were carried out using regular and uniform grids as well as boundary-fitted grids. The studied cases include: steady state problems over a 2D varying topography, 1D classical dam-break problems, 2D partial dam-break, Cylindrical dam-break, 1D oscillating water column over a frictional basin, 2D nonlinear oscillations over a parabolic basin and Supercritical flow over a converging channel.

1.1.3. Application

Laboratory dam-break experiences were carried out to obtain high-resolution data to test the developed numerical model. Two laboratory campaigns were performed in the Hydraulic Engineering Laboratory of the *Pontificia Universidad Católica de Chile* to study the sudden emptying of a reservoir over a scaled physical model of a river reach. Measurement instruments and technical support was provided by the *Instituto Nacional de Hidráulica* (INH).

The experience consisted in rapidly open a reservoir gate in order to release the holded volume of water, which generates a shock-wave that propagates downstream, producing fast free surface variations that were recorded for 60 seconds. Then, the experience was simulated using the new numerical model and the results were compared with the recorded data.

This experience is a demanding test to any numerical model, since all the flow features that the numerical model is seeking to capture are present in the experience. Good estimation of the flow variables were obtained.

1.2. Thesis Outline

The following two chapters correspond to two articles which are devoted to detail the development of the curvilinear NSWE model and the laboratory experiences.

In the first article, the new model **SURF_WBUC** is described and validated. The article focuses on the governing equations transformation and on the application of model to solve the equations. Some of the validation tests involving frictional topographies and the use of a curvilinear discretization of the domain are presented. This article part allows us to demonstrate that the numerical method developed possess the sought shock-capturing and well-balancing abilities. The latter let us to hypothesize that it can be an effective tool to represent extreme flooding over complicated topographies, such as dam-breaks, GLOF, tsunamis or river overflows.

More realistic applications are considered in the second part. We focus on the abilities of the numerical model to represent the hydrodynamics of extreme flood waves produced over a scaled physical model of a river reach. A complete description of the experimental set-up and the post-processing of the data, that allow us to build the numerical application, are presented. Excellent numerical results are obtained in terms of amplitudes of the propagating waves, arrival times and the recession curves. The latter further demonstrates that the developed numerical model is a robust tool able to accurately represent the hydrodynamics of extreme floods in the framework of inertia-dominated flow.

Finally, conclusions and future perspectives are discussed. In the appendices, detailed information concerning the transformation of the governing equations, the numerical scheme, boundary conditions and complementary benchmark cases, are presented.

2. A CURVILINEAR FINITE VOLUME MODEL FOR INERTIA-DOMINATED SHALLOW WATER FLOWS INCLUDING BATHYMETRIC VARIATIONS, BOTTOM FRICTION AND RUN-UP

2.1. Abstract

Natural shallow flows take place over rough and varying topographies with arbitrary boundaries, and in many cases they are unsteady or characterized by important changes of velocity and water depth due to shock waves or wet-dry interfaces. Numerical models using conventional Cartesian discretizations, however, might not represent correctly the hydrodynamics of these complex flows since they cannot reproduce the geometrical details of natural domains. In order to predict efficiently and accurately the dynamics of shallow inertial flows, we develop a well-balanced and robust numerical model to solve the nonlinear shallow water equations (NSWE) in non-orthogonal boundary-fitted curvilinear coordinate systems. Curvilinear NSWE are solved with a shock-capturing finite-volume scheme that directly incorporates the effects of friction and bed-slope source terms in the momentum equations. The friction source term is accounted for through a semi-implicit fractional-step approach, while the bed-slope is discretized with a well-balanced hydrostatic reconstruction method in conjunction with the robust VF Roe-ncv approximate Riemann solver and a second order MUSCL approach (Gallouet et al., 2003b; Q. Liang & Marche, 2009). The resulting numerical scheme for curvilinear NSWE is second-order accurate in space and fourth-order in time. Together with shock-capturing ability, this method can compute flows over highly variable topography and preserve the positivity of the water depth, leading to accurate simulations of wetting and drying processes, and preserving motionless steady states. This new numerical method is validated against several benchmark cases that consider the use of a boundary-fitted discretization of the domain, and shows to be a robust tool to predict rapid and extreme flood processes such as dam-breaks, tsunamis, or river overflows.

2.2. Introduction

In hydraulic engineering and geophysics a wide variety of shallow flows, such as rivers, lakes or estuaries, can be modeled by the Nonlinear Shallow Water Equations (NSWE), which describe the dynamics of fairly long waves of homogeneous, incompressible, and non-viscous fluids. The system is obtained by vertically averaging the three-dimensional Navier-Stokes equations assuming a hydrostatic pressure distribution, resulting in a set of horizontal two-dimensional hyperbolic conservation laws that describe the evolution of the water depth and depth-averaged velocities (Cunge et al., 1980; Stoker, 1992; Toro, 2001).

Shallow inertial flows often occur over highly varying topography giving rise to complex unsteady free-surface dynamics where discontinuities may arise. An accurate numerical representation of those features remains as a challenging task to common finite-difference or finite-volume methods (Toro, 2001), since numerical strategies for solving the NSWE in shallow inertial flows should be able to deal with arbitrary geometries and capture their complex dynamics. Similarly, the discretization of the boundaries of the physical domain may have a strong influence in the development of the hydrodynamics, introducing large errors or numerical instability if not carefully performed (Baghlan et al., 2008). The use of boundary-fitted grids can address these problems (Shi et al., 2001), by improving the accuracy of the numerical solutions. They rely in partial transformation of the governing equations in generalized curvilinear coordinates, in order to maintain the flow variables referenced to the Cartesian frame. The resulting system can be discretized and solved by finite-difference methods (Molls & Chaudry, 1995; Molls & Zhao, 2000), finite-element methods (Berger & Stockstill, 1995; Tucciarelli & Termini, 2000), or standard finite-volume methods (Valiani et al., 2002; Zhou et al., 2004; Loose et al., 2005).

In the framework of finite volume methods, Godunov-type formulations have become very useful to solve the NSWE, since they can reproduce complex discontinuities such as shock-waves or wet-dry interfaces by solving a Riemann problem at each cell interface of the discretized domain (Toro, 2001; Leveque, 2002). These methods have been implemented to solve the curvilinear NSWE, having the advantage of grid adaptability to the

geometry of the problem, and the ability to produce quantitatively accurate results near the boundaries (Alcrudo & García-Navarro, 1993; Mingham & Causon, 1998; Causon & Mingham, 1999; Fujihara & Borthwick, 2000; D. Liang et al., 2007).

Another important issue that arises when discretizing NSWE over varying topographies is the preservation of the steady state, since most geophysical flows come from, or converge to this regime. Well-balanced schemes are specifically conceived to preserve the steady state, including the important class of motionless states, which need local and global mass conservation to machine accuracy. To achieve this requirement, it is necessary to discretize carefully the bed-slope source term as shown in previous investigations (Greenberg & Leroux, 1996; LeVeque, 1998; Gallouet et al., 2003b; Audusse et al., 2004; Q. Liang & Marche, 2009).

In this work, we develop an extended version of the NSWE model recently presented by Marche et al. (2007) in a non-orthogonal generalized curvilinear coordinate framework. We develop a finite volume well-balanced approach, based on a robust VF Roe Riemann solver (Gallouet et al., 2003b) to calculate mass and momentum fluxes at cell interfaces and the hydrostatic reconstruction method proposed by Audusse et al. (2004). The source term that accounts for friction effects is treated with the semi-implicit fractional-step approach of Q. Liang and Marche (2009). The model is validated through several benchmark tests chosen to assess its ability to deal with wet and dry interfaces, complex geometries, shocks, friction and bathymetry source terms.

The paper is organized as follows. In section 2.3 we present the non-dimensional governing equations and the partial transformation to generalized non-orthogonal curvilinear coordinates that are employed in the model. The proposed numerical scheme and the steps of the method to handle the integration of the NSWE is described in section 2.4. Validation tests and comparisons of numerical simulations with analytical solutions and experimental data are presented in section 2.5. Finally, conclusions and future perspectives of this work are presented in section 2.6.

2.3. Governing Equations

The two-dimensional NSWE are a system of nonlinear partial differential equations representing mass and momentum conservation laws (Toro, 2001). The main assumptions behind this model are incompressible and homogeneous fluid and hydrostatic pressure distribution, which correspond to the shallow water or long-wave hypothesis, implying negligible vertical velocities and depth-uniform horizontal velocities. The NSWE are often applied to river or nearshore flows where the characteristic horizontal wavelength is much longer than the characteristic water depth (see (Cunge et al., 1980) for more details).

In what follows, we will work on a non-dimensionalized set of NSWE by choosing characteristic horizontal and vertical length-scales and a velocity scale (\mathcal{H} , \mathcal{L} , and \mathcal{U} respectively), noting that the shallow-water assumptions require different scaling between the horizontal and vertical scales. The non-dimensional form of the governing equations simplifies the magnitude of the flow variables for the computation and gives an indication of the relative magnitude of the water-depth and flow velocities. By defining the length and velocity scales of the flow the time-scale is also fixed such that $T = \mathcal{L}/\mathcal{U}$, and the dimensionless Froude number, $Fr = \mathcal{U}/\sqrt{g\mathcal{H}}$, quantifies the relative importance of inertial effects over gravity (g). The dimensional variables, noted with a hat ($\hat{\cdot}$), are therefore defined as $\hat{x} = \mathcal{L}x$, $\hat{y} = \mathcal{L}y$, $\hat{z} = \mathcal{H}z$, $\hat{h} = \mathcal{H}h$, $\hat{u} = \mathcal{U}u$, $\hat{v} = \mathcal{U}v$, and $\hat{t} = Tt$. Where \hat{x} and \hat{y} represent the Cartesian directions, \hat{z} defines the bed elevation, \hat{h} is the water depth, \hat{u} and \hat{v} are the depth-averaged flow velocities in each Cartesian direction, and \hat{t} is the time. In Fig. 2.1, a schematic drawing of the main variables of the flow and the characteristic dimensional scales are shown.

Considering only bed-slope and friction source terms, the non-dimensional NSWE can be written in Cartesian coordinates in the following conservation form,

$$\frac{\partial Q}{\partial t} + \frac{\partial \bar{F}}{\partial x} + \frac{\partial \bar{G}}{\partial y} = S(Q) \quad (2.1)$$

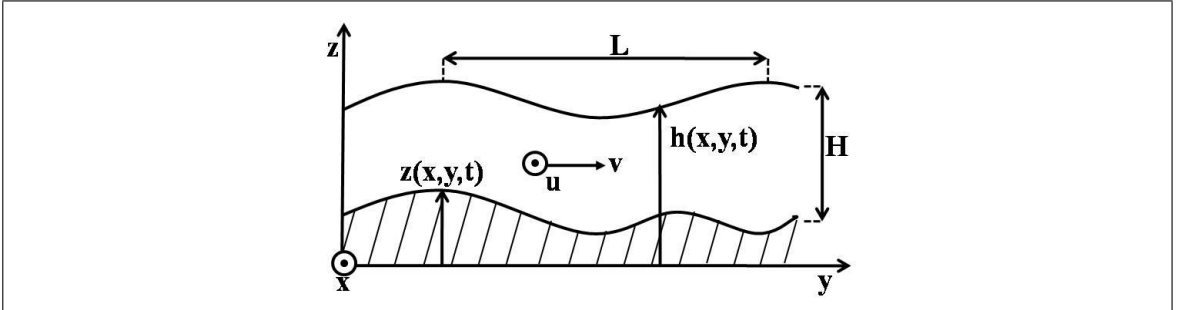


FIGURE 2.1. Schematic drawing of hydrodynamic variables and characteristic scales

where Q is the vector of hydrodynamic variables, \bar{F} and \bar{G} are respectively the flux vectors in each Cartesian direction, and S is the source term vector. These vectors are given by the following expressions,

$$Q = \begin{pmatrix} h \\ hu \\ hv \end{pmatrix}, \bar{F}(Q) = \begin{pmatrix} hu \\ hu^2 + \frac{1}{2Fr^2}h^2 \\ huv \end{pmatrix}, \bar{G}(Q) = \begin{pmatrix} hv \\ huv \\ hv^2 + \frac{1}{2Fr^2}h^2 \end{pmatrix} \quad (2.2)$$

$$S(Q) = \begin{pmatrix} 0 \\ -\frac{h}{Fr^2} \frac{\partial z}{\partial x} - S_{fx} \\ -\frac{h}{Fr^2} \frac{\partial z}{\partial y} - S_{fy} \end{pmatrix}$$

where z_x and z_y define the bed-slope in each coordinate direction, and S_f represents the friction source term.

In order to have a correct representation of arbitrarily complex geometries, we introduce a boundary-fitted curvilinear coordinate system in two dimensions denoted by the coordinate system (ξ, η) shown in Fig. 1.4. Generalized curvilinear coordinates are chosen to follow the boundaries of the domain, adapting the grid to the geometrical details of the computational domain. In this framework the mesh lines can be curved and their intersection is not necessarily orthogonal. This coordinate system is defined such that the curvilinear discretization of the (x, y) domain is transformed into a rectangular and regular mesh in the transformed space (ξ, η) as shown in Fig. 1.4. This approach allows to get

a better resolution in zones of interest and an accurate representation of the boundaries, resulting in an efficient discretization of the flow domain (Baghlani et al., 2008; D. Liang et al., 2007; Lackey & Sotiropoulos, 2005).

The system of equations (2.1) can be partially transformed to this new coordinate system maintaining the hydrodynamic variables referenced to the Cartesian frame. This procedure is known as partial transformation and only modifies the mass and momentum fluxes of the governing equations. The full transformation would change the variables in vector Q to the velocity components in the ξ and η directions, so-called contravariant velocity components, and the derivatives in the convective terms would yield the well-known Christoffel symbols of the second kind (TranNgoc & Takashi, 2007). Therefore, the transformed set of equations can be written as follows,

$$\frac{\partial Q}{\partial t} + J \frac{\partial F}{\partial \xi} + J \frac{\partial G}{\partial \eta} = S(Q) \quad (2.3)$$

where Q remains the same vector shown in Eqs. (2.1), but flux vectors are now expressed in terms of the time t , and the new spatial coordinate system ξ and η . With the partial coordinate transformation, the non-dimensional mass and momentum fluxes and source term vectors are expressed as follows,

$$F = \frac{1}{J} \begin{pmatrix} hU^1 \\ uhU^1 + \frac{1}{2Fr^2}h^2\xi_x \\ vhU^1 + \frac{1}{2Fr^2}h^2\xi_y \end{pmatrix}, \quad G = \frac{1}{J} \begin{pmatrix} hU^2 \\ uhU^2 + \frac{1}{2Fr^2}h^2\eta_x \\ vhU^2 + \frac{1}{2Fr^2}h^2\eta_y \end{pmatrix}, \quad (2.4)$$

$$S = \begin{pmatrix} 0 \\ -\frac{h}{Fr^2}(z_\xi\xi_x + z_\eta\eta_x) - S_{fx} \\ -\frac{h}{Fr^2}(z_\xi\xi_y + z_\eta\eta_y) - S_{fy} \end{pmatrix}$$

where z_ξ and z_η define the local bed slope with respect to the curvilinear coordinate system (ξ, η) . It is important to note that the friction source term is not affected by the coordinate transformation, since the momentum equations are maintained in the cartesian system.

The additional terms that appear in the fluxes, ξ_x , ξ_y , η_x , and η_y are the resulting metrics associated to the coordinate change, and $J = \xi_x \eta_y - \xi_y \eta_x$ is the Jacobian of the transformation, which will remain constant for a fixed grid. U^1 and U^2 are the contravariant velocity components, and are expressed as $U^j = u\epsilon_x + v\epsilon_y$ with $(j, \epsilon) \in (1, \xi), (2, \eta)$. As shown in Fig. 1.4, the transformed system of equations are discretized on a rectangular and uniform grid in the transformed space (ξ, η) using the finite volume method that is described in the next section.

2.4. Numerical Scheme

The transformed curvilinear NSWE, given by Eqs. (2.3), are solved using a finite volume well-balanced scheme, which incorporates separately the friction and bed-slope in the momentum source terms. The numerical procedure consists of an initial step in which the friction source term in the momentum equations is incorporated employing a semi-implicit method. In a second hyperbolic NSWE step, the variables are reconstructed at the cell interfaces and the fluxes are found through the solution of the Riemann problem at the cell interfaces using a non-conservative form of the governing equations. This methodology gives the numerical model the well-balanced property by considering the bed-slope in the spatial discretization schemes using a MUSCL type reconstruction method. The discretized form of the governing equations is integrated in time using a multi-stage Runge-Kutta scheme. In Fig. 2.2 a schematic flux diagram of the numerical scheme is shown, in order to explain how the scheme works at every time-step.

In the following sections we describe in detail the different steps of the algorithm, including the implementation of boundary conditions and the stability criterion of the numerical solution.

2.4.1. Semi-Implicit Friction Step

The friction source term is incorporated using the splitting semi-implicit method proposed in Q. Liang and Marche (2009), which is extended here for the two-dimensional

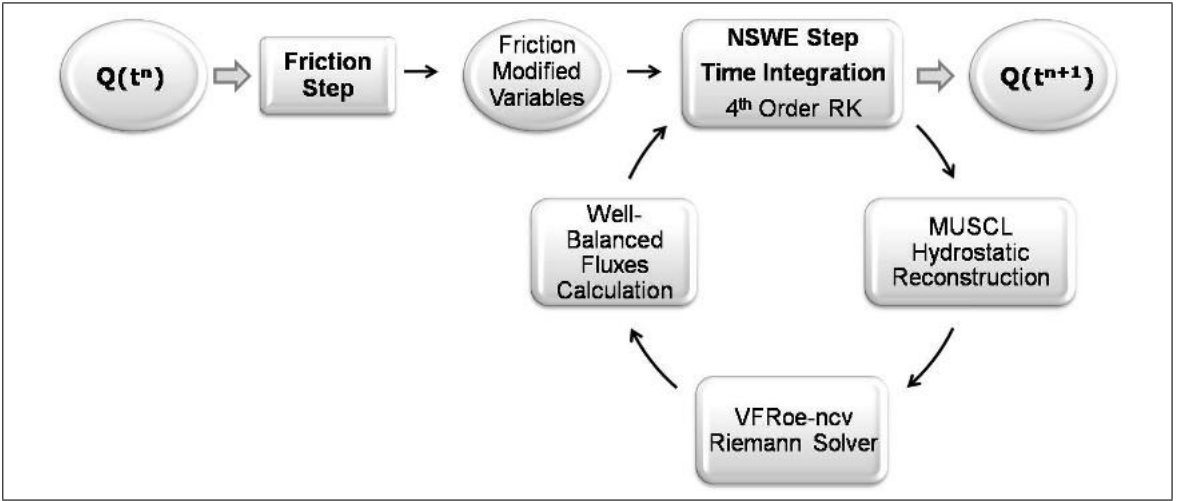


FIGURE 2.2. Numerical Scheme: Flux Diagram for each time-step

curvilinear case. This method consists in solving the ordinary differential equation.

$$\frac{dQ}{dt} = S_f \quad (2.5)$$

where the friction term S_f can be written in the following manner,

$$S_f = \begin{pmatrix} 0 \\ -\frac{\tau_{fx}}{\rho} \\ -\frac{\tau_{fy}}{\rho} \end{pmatrix} \quad (2.6)$$

The bed shear-stresses in the momentum equations are denoted as τ_{fx} and τ_{fy} for each cartesian direction, and ρ is the water density. The magnitude of the bed shear stresses in each direction can be calculated as follows,

$$\tau_{fx} = \rho C_f u \sqrt{u^2 + v^2} \quad (2.7)$$

$$\tau_{fy} = \rho C_f v \sqrt{u^2 + v^2} \quad (2.8)$$

where C_f is a non dimensional bed friction coefficient, which can be expressed using one of the standard existing approaches developed for uniform flow such as Manning or Chézy (Chow, 1959).

In Eq. (2.5) the friction term has no effect on the water depth h through the continuity equation, therefore we only solve the flow dynamics for a vector containing the variables in momentum equations:

$$\frac{dq}{dt} = S_f \quad (2.9)$$

where $q = [hu, hv]^T$, according to the momentum equation in each Cartesian coordinate direction, and the friction source term $S_f = [\tau_x/\rho, \tau_y/\rho]^T$. This equation is implicitly discretized as follows,

$$\frac{q^{n+1} - q^n}{\Delta t} = S_f^{n+1} \quad (2.10)$$

where n and $n+1$ denote the instant $t^n = t$ and $t^{n+1} = t + \Delta t$ respectively. The S_f^{n+1} term can be expressed using a second-order Taylor series expansion around $\Delta q = q^{n+1} - q^n$ such that,

$$S_f^{n+1} = S_f^n + \left(\frac{\partial S_f}{\partial q} \right) \Delta q + O(\Delta q^2) \quad (2.11)$$

Thus, retaining only first-order terms in Eq. (2.10), the following expression for the unknown variables is found,

$$q^{n+1} = q^n + \Delta t f \quad (2.12)$$

where the momentum flux is calculated as $f = \left(\frac{S_f^n}{D^n} \right)$, and $D^n = 1 - \Delta t (\partial S_f / \partial q)^n$

When solving the NSWE with friction this term may lead to a large friction force near the wet/dry front and eventually reverse the flow. In order to prevent this inconsistency, the friction force effect must be limited. At every time-step Δt , the state variables are first modified to take into account the bed roughness effects, and then this partial solution is used as initial condition for the hyperbolic NSWE step. For a detailed description of this method and the limiting-friction procedure, the reader is referred to the work of Q. Liang and Marche (2009).

2.4.2. Hyperbolic NSWE Step

The finite-volume numerical methodology consists on solving the NSWE without the friction terms, combining the approximate well-balanced VFRoe Riemann solver developed by Gallouet et al. (2003b) for the homogeneous problem, with the hydrostatic reconstruction method proposed by Audusse et al. (2004) to incorporate the bed-slope source term.

The semi-discrete finite-volume formulation for the system of equations (2.3) in the element (i, j) of the computational grid can be written as follows:

$$\frac{d}{dt}Q_{i,j} + \frac{J_{i,j}}{\Delta\xi}(F_{i+\frac{1}{2},j}^* - F_{i-\frac{1}{2},j}^*) + \frac{J_{i,j}}{\Delta\eta}(G_{i,j+\frac{1}{2}}^* - G_{i,j-\frac{1}{2}}^*) = S_{ij} \quad (2.13)$$

where $Q_{i,j}$ is the vector of cell-centered hydrodynamic variables, $J_{i,j}$ is the cell-centered Jacobian of the coordinate transformation, $F_{i\pm\frac{1}{2},j}^*$ and $G_{i,j\pm\frac{1}{2}}^*$ correspond to the numerical fluxes through the (i, j) cell interfaces, and $S_{i,j}$ to the centered discretization of the bed-slope source term. A successful application of the scheme requires a convenient estimation of the numerical fluxes and the $S_{i,j}$ source term. In Fig. 2.3 we depict a sketch of the typical discretization cell and the fluxes. In this figure the subindices L and R denote the left and right boundaries of the cell, while the $-$ and $+$ signs represent the left and right sides of the cell interface. To find the discretized fluxes in Eq. (2.13), we solve the Riemann problem at each cell interface using a non-conservative form of the governing equations. In the following subsections we describe the numerical procedure and explain in detail the variable reconstruction to compute all the terms in Eq. (2.13).

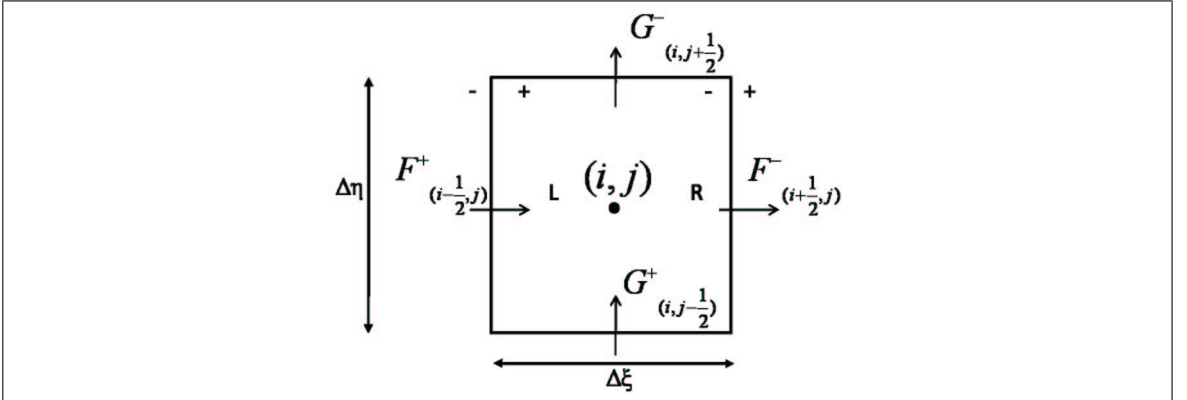


FIGURE 2.3. Discretization cell and numerical fluxes

2.4.2.1. The Non-conservative Solver

The numerical solution in the curvilinear system requires that the spatial discretization captures the steep gradients or shock-waves in the flow and also to account for wetting and drying variations in unsteady flows. In this model we employ the VRoe-ncv scheme (Marche et al., 2007; Gallouet et al., 2003a), which solves exactly a linearized Riemann problem in each cell interface. This scheme uses a non-conservative change of variables, which ensures that intermediate states remain positive and preserve the non-negativity of the water depth at least for the interface values. For all the details on the formalism of this scheme and its applications the reader is referred to the work of Gallouet et al. (2003b), and the recent modification presented by Marche (2007).

The VFROe-ncv solver is used here for the homogeneous part of the shallow-water equations to obtain the value of the state variables at the cell interfaces Q^* , which is later used to calculate the associated numerical fluxes F^* and G^* shown in Eq. (2.13). First we perform a non-conservative change of variables to the system of equations (2.3) using the vector $W(Q) = (2C, u, v)$. In this formulation the first component of vector W contains the non-dimensional wave celerity defined as $C = \sqrt{h/Fr^2}$. To obtain a non-conservative form of the NSWE and apply the VFROe method the change of variables produces the following system of equations using the chain rule of derivation,

$$W_t + B^1(W)W_\xi + B^2(W)W_\eta = 0 \quad (2.14)$$

where the matrices B^1 and B^2 are the corresponding Jacobian matrices of the fluxes in the transformed Eq. (2.3) with respect to the vector of hydrodynamic variables $W(Q)$ (Toro, 2001). These matrices can be written as,

$$B^1(W) = \begin{pmatrix} U^1 & C\xi_x & C\xi_y \\ C\xi_x & U^1 & 0 \\ C\xi_y & 0 & U^1 \end{pmatrix} \quad \text{and} \quad B^2(W) = \begin{pmatrix} U^2 & C\eta_x & C\eta_y \\ C\eta_x & U^2 & 0 \\ C\eta_y & 0 & U^2 \end{pmatrix} \quad (2.15)$$

To clarify the numerical procedure we explain in detail the application of the method to the ξ direction to obtain the augmented Riemann Problem (RP). In this particular case the variable extrapolation depends on the eigenvalues of the averaged Jacobian matrices, which can be computed directly by diagonalizing the system of equations with the following procedure. In the ξ direction, the set of equations can be written as:

$$W_t + B^1(W)W_\xi = 0 \quad (2.16)$$

$$W(x, 0) = \begin{cases} W_L & \text{if } \xi < 0 \\ W_R & \text{if } \xi > 0 \end{cases} \quad (2.17)$$

where W_L and W_R are the interface left and right side states of vector W . The RP, Eq. (2.16), is then linearized around the averaged state $\tilde{W} = \frac{W_L + W_R}{2}$. Therefore, the linearized Jacobian matrix B^1 for the ξ direction is defined as follows:

$$B^1(\tilde{W}) = \begin{pmatrix} \tilde{U}^1 & \tilde{C}\tilde{\xi}_x & \tilde{C}\tilde{\xi}_y \\ \tilde{C}\tilde{\xi}_x & \tilde{U}^1 & 0 \\ \tilde{C}\tilde{\xi}_y & 0 & \tilde{U}^1 \end{pmatrix} \quad (2.18)$$

where the tilde (\sim) represents the averaged values of the left and right sides of the cell interface.

The eigenvalues and left and right eigenvectors matrices of the linearized Jacobian matrix are thus written as,

$$\tilde{\lambda}_1 = \tilde{U}^1 - \tilde{C}\sqrt{(\tilde{\xi}_x^2 + \tilde{\xi}_y^2)}, \quad \tilde{\lambda}_2 = \tilde{U}^1, \quad \tilde{\lambda}_3 = \tilde{U}^1 + \tilde{C}\sqrt{(\tilde{\xi}_x^2 + \tilde{\xi}_y^2)} \quad (2.19)$$

$$\tilde{R}^1 = \begin{pmatrix} -\sqrt{(\tilde{\xi}_x^2 + \tilde{\xi}_y^2)} & 0 & \sqrt{(\tilde{\xi}_x^2 + \tilde{\xi}_y^2)} \\ \tilde{\xi}_x & -\tilde{\xi}_y & \tilde{\xi}_x \\ \tilde{\xi}_y & \tilde{\xi}_x & \tilde{\xi}_y \end{pmatrix} \quad (2.20)$$

$$\tilde{L}^1 = \begin{pmatrix} \frac{-1}{2\sqrt{(\tilde{\xi}_x^2 + \tilde{\xi}_y^2)}} & \frac{\tilde{\xi}_x}{2(\tilde{\xi}_x^2 + \tilde{\xi}_y^2)} & \frac{\tilde{\xi}_y}{2(\tilde{\xi}_x^2 + \tilde{\xi}_y^2)} \\ 0 & \frac{-\tilde{\xi}_y}{(\tilde{\xi}_x^2 + \tilde{\xi}_y^2)} & \frac{\tilde{\xi}_x}{(\tilde{\xi}_x^2 + \tilde{\xi}_y^2)} \\ \frac{1}{2\sqrt{(\tilde{\xi}_x^2 + \tilde{\xi}_y^2)}} & \frac{\tilde{\xi}_x}{2(\tilde{\xi}_x^2 + \tilde{\xi}_y^2)} & \frac{\tilde{\xi}_y}{2(\tilde{\xi}_x^2 + \tilde{\xi}_y^2)} \end{pmatrix} \quad (2.21)$$

According to Marche et al. (2007), the exact solution to the linearized RP at each side of the interface is given by the sign of the eigenvalues $\tilde{\lambda}_i$. From all the possible combinations only two cases become relevant (Marche et al., 2007),

- (i) If $\tilde{\lambda}_1 > 0$ or $\tilde{\lambda}_3 < 0$, then the flow is super-critical and the interface value is defined as,

$$W^* = \begin{cases} W_L & \text{if } \tilde{\lambda}_i > 0 \quad \forall i \\ W_R & \text{if } \tilde{\lambda}_i < 0 \quad \forall i \end{cases} \quad (2.22)$$

- (ii) If $\tilde{\lambda}_1 < 0$ and $\tilde{\lambda}_3 > 0$, then the flow is sub-critical and we are in the intermediate region. According to Marche et al. (2007), the solution is defined depending on the sign of $\tilde{\lambda}_2$ as follows,

$$W^* = \begin{cases} W_L + \tilde{L}_1^T [W]_L^R \tilde{R}_1 & \text{if } \tilde{\lambda}_2 > 0 \\ W_R - \tilde{L}_3^T [W]_L^R \tilde{R}_3 & \text{if } \tilde{\lambda}_2 < 0 \end{cases} \quad (2.23)$$

where $[W]_L^R = W_R - W_L$, and \tilde{L}_i and \tilde{R}_i are the left and right eigenvectors of the linearized convection matrix associated to each eigenvalue $\tilde{\lambda}_i$ (Marche et al., 2007). R_i vectors correspond to the columns of the R^1 matrix and L_i , to the lines of the L^1 matrix.

As an example we can show that for the $(i + \frac{1}{2})$ cell interface, the left state is $L = i$ and the right side state is $R = i + 1$. If the flow is sub-critical, i.e. $\tilde{\lambda}_1 > 0$ and $\tilde{\lambda}_3 < 0$, and

$\tilde{\lambda}_2 > 0$, the solution at the cell interface would be given by,

$$W^* = W_L + \begin{pmatrix} -1 \\ 2\sqrt{(\xi_x^2 + \xi_y^2)} & \frac{\xi_x}{2(\xi_x^2 + \xi_y^2)} & \frac{\xi_y}{2(\xi_x^2 + \xi_y^2)} \end{pmatrix} \begin{pmatrix} 2[C]_L^R \\ [u]_L^R \\ [v]_L^R \end{pmatrix} \begin{pmatrix} -\sqrt{\xi_x^2 + \xi_y^2} \\ \xi_x \\ \xi_y \end{pmatrix} \quad (2.24)$$

Then the wave celerity and instantaneous flow velocities at the cell interface ($i + \frac{1}{2}$) are computed using the following expressions:

$$2C_{i+\frac{1}{2},j} = 2C_L - \sqrt{\tilde{\xi}_x^2 + \tilde{\xi}_y^2} \left(-\frac{2[C]_L^R}{2\sqrt{\tilde{\xi}_x^2 + \tilde{\xi}_y^2}} + \frac{\tilde{\xi}_x[u]_L^R}{2(\tilde{\xi}_x^2 + \tilde{\xi}_y^2)} + \frac{\tilde{\xi}_y[v]_L^R}{2(\tilde{\xi}_x^2 + \tilde{\xi}_y^2)} \right) \quad (2.25)$$

$$u_{i+\frac{1}{2},j} = u_L + \tilde{\xi}_x \left(-\frac{2[C]_L^R}{2\sqrt{\tilde{\xi}_x^2 + \tilde{\xi}_y^2}} + \frac{\tilde{\xi}_x[u]_L^R}{2(\tilde{\xi}_x^2 + \tilde{\xi}_y^2)} + \frac{\tilde{\xi}_y[v]_L^R}{2(\tilde{\xi}_x^2 + \tilde{\xi}_y^2)} \right) \quad (2.26)$$

$$v_{i+\frac{1}{2},j} = v_L + \tilde{\xi}_y \left(-\frac{2[C]_L^R}{2\sqrt{\tilde{\xi}_x^2 + \tilde{\xi}_y^2}} + \frac{\tilde{\xi}_x[u]_L^R}{2(\tilde{\xi}_x^2 + \tilde{\xi}_y^2)} + \frac{\tilde{\xi}_y[v]_L^R}{2(\tilde{\xi}_x^2 + \tilde{\xi}_y^2)} \right) \quad (2.27)$$

Using this procedure the original conservative state variables at the cell interface in vector Q are found using an inverse change of variables from the non-conservative vector W , and then employed to calculate the numerical fluxes through the cell interfaces in Eq. (2.13):

$$F_{i+\frac{1}{2},j}^* = F [Q^*(0, Q_{i,j}, Q_{i+1,j})] \quad (2.28)$$

The process is analogous for the η coordinate direction. The RP is defined along the η coordinate considering the B^2 convection matrix, and the $(j + 1/2)$ cell interface. In the following step we show how the reconstruction is performed to achieve the well-balanced property of the numerical method in generalized non-orthogonal curvilinear coordinates.

2.4.2.2. The hydrostatic reconstruction

The bed-slope source term is discretized and incorporated in the numerical scheme using the well-balanced method proposed in Audusse et al. (2004). This second-order

accurate scheme satisfies the steady state static condition (global and local mass conservation), and also preserves the ability of the VFRoe-ncv solver to handle dry areas.

The hydrostatic reconstruction method is based in the MUSCL extrapolation (Monotonic Upwind Scheme for Conservation Laws) introduced by van Leer (Van-Leer, 1979). The method consists on calculating the numerical fluxes from limited reconstructed values at each side of the interface rather than cell-centered values, taking into account bed variations and the hydrostatic balance for the steady states at rest (Audusse et al., 2004). The method relies on the steps of the MUSCL extrapolation, such that the limited reconstructed values are found in three steps: i.) prediction of the gradients in each cell; ii.) linear extrapolation of the state variables to the cell interfaces; and iii.) slope limiting procedure.

In the ξ direction, considering the i cell, the linear reconstruction of Q_{iR} and Q_{iL} , at $i+1/2^-$ and $i-1/2^+$ interface (see Fig. 2.3) is calculated using a *minmod* limiter (Leveque, 2002). The free surface elevation $H = h + z$ is also reconstructed, obtaining H_{iR} and H_{iL} . Finally, the bed elevation z is obtained from the reconstructed values of water elevation and free surface as follows,

$$z_{iL} = H_{iL} - h_{iL} \quad (2.29)$$

$$z_{iR} = H_{iR} - h_{iR} \quad (2.30)$$

The hydrostatic reconstruction of the water elevation at each side of the cell interface is computed by ensuring the positivity preserving condition following the limits proposed in Marche et al. (2007). Taking into account bottom variations this method reads,

$$h_{i+\frac{1}{2}^-} = \max \left[0, h_{iR} + z_{iR} - z_{i+\frac{1}{2}} \right] \quad (2.31)$$

$$h_{i+\frac{1}{2}^+} = \max \left[0, h_{i+1L} + z_{i+1L} - z_{i+\frac{1}{2}} \right] \quad (2.32)$$

where the bed elevation at the cell interface, $z_{i+\frac{1}{2}}$, is calculated from,

$$z_{i+\frac{1}{2}} = \max [z_{iR}, z_{i+1L}] \quad (2.33)$$

Finally, the state variables at the cell interface can be computed as,

$$Q_{i+\frac{1}{2}+} = \begin{pmatrix} h_{i+\frac{1}{2}+} \\ h_{i+\frac{1}{2}+} u_{(i+1)L} \\ h_{i+\frac{1}{2}+} u_{(i+1)L} \end{pmatrix}, \quad Q_{i+\frac{1}{2}-} = \begin{pmatrix} h_{i+\frac{1}{2}-} \\ h_{i+\frac{1}{2}-} u_{iR} \\ h_{i+\frac{1}{2}-} u_{iR} \end{pmatrix} \quad (2.34)$$

This new reconstructed values are now used to solve the homogeneous system with the VF Roe-ncv solver described in section 2.4.2.1 and find the state values at the interface. Therefore, the numerical fluxes through the cell interfaces are calculated as,

$$F_{i+\frac{1}{2}}^* = F \left[Q_{i+\frac{1}{2}}^*(0, Q_{i+\frac{1}{2}-,j}, Q_{i+\frac{1}{2}+,j}) \right] \quad (2.35)$$

The bed-slope source term is also estimated through the new reconstructed values instead of the cell-centered ones, and then distributed to the cell interfaces considering the well-balanced requirement for static flows at rest (Audusse et al., 2004). At steady state, $h + z = \text{const.}$ and $\frac{\partial}{\partial t} = 0$, and at rest, $u = v = 0$. Then the first momentum equation of the curvilinear NSWE becomes,

$$J \left(\frac{1}{J} \frac{1}{2Fr^2} h^2 \xi_x \right)_\xi + J \left(\frac{1}{J} \frac{1}{2Fr^2} h^2 \eta_x \right)_\eta = - \frac{h}{Fr^2} (\xi_x z_\xi + \eta_x z_\eta) \quad (2.36)$$

The source term associated to each curvilinear coordinate direction, (ξ, η) , is balanced with the momentum flux in the same direction,

$$J \left(\frac{1}{J} \frac{1}{2Fr^2} h^2 \xi_x \right)_\xi \approx - \frac{h}{Fr^2} \xi_x z_\xi \quad (2.37)$$

$$J \left(\frac{1}{J} \frac{1}{2Fr^2} h^2 \eta_x \right)_\eta \approx - \frac{h}{Fr^2} \eta_x z_\eta \quad (2.38)$$

This approach leads to the specific discretization of the source term, which for the ξ direction is written as,

$$S_i^\xi = S_{i+\frac{1}{2}}^- + S_{i-\frac{1}{2}}^+ \quad (2.39)$$

$$S_{i+\frac{1}{2}}^- = \begin{pmatrix} 0 \\ \frac{1}{2Fr^2} \left(\frac{\xi_x}{J} \right)_{i+\frac{1}{2}} h_{i+\frac{1}{2}^-}^2 - \left(\frac{\xi_x}{J} \right)_i h_{iR}^2 \\ \frac{1}{2Fr^2} \left(\frac{\xi_y}{J} \right)_{i+\frac{1}{2}} h_{i+\frac{1}{2}^-}^2 - \left(\frac{\xi_y}{J} \right)_i h_{iR}^2 \end{pmatrix} \quad (2.40)$$

$$S_{i-\frac{1}{2}}^+ = \begin{pmatrix} 0 \\ \frac{1}{2Fr^2} \left(\frac{\xi_x}{J} \right)_{i-\frac{1}{2}} h_{i-\frac{1}{2}^+}^2 - \left(\frac{\xi_x}{J} \right)_i h_{iL}^2 \\ \frac{1}{2Fr^2} \left(\frac{\xi_y}{J} \right)_{i-\frac{1}{2}} h_{i-\frac{1}{2}^+}^2 - \left(\frac{\xi_y}{J} \right)_i h_{iL}^2 \end{pmatrix} \quad (2.41)$$

A centered source term Sc_i needs to be added to ensure consistency of the scheme and preserve the well-balanced property of the numerical solution (Marche et al., 2007). For the ξ direction this source term can be expressed as follows,

$$Sc_i^\xi = -\frac{1}{Fr^2} \begin{pmatrix} 0 \\ \xi_x i \left(\frac{h_{iL}^2 + h_{iR}^2}{2} \right) \left(\frac{z_{iR} - z_{iL}}{\Delta\xi} \right) \\ \xi_y i \left(\frac{h_{iR} + h_{iL}}{2} \right) \left(\frac{z_{iR} - z_{iL}}{\Delta\xi} \right) \end{pmatrix} \quad (2.42)$$

The same procedure is performed for the fluxes and source term in the η direction.

The application of the new FV formulation can be summarized as follows,

$$\frac{dQ_{i,j}(t)}{dt} + \frac{J_{i,j}}{\Delta\xi} \left(F_{i+\frac{1}{2},j}^- - F_{i-\frac{1}{2},j}^+ \right) + \frac{J_{i,j}}{\Delta\eta} \left(G_{i,j+\frac{1}{2}}^- - G_{i,j-\frac{1}{2}}^+ \right) = Sc_{i,j} \quad (2.43)$$

where the matrices in Eq. (E.61) are expressed as:

$$F_{i+\frac{1}{2},j}^- = F(Q_{i+\frac{1}{2},j}^*(0, Q_{i+\frac{1}{2}^-,j}, Q_{i+\frac{1}{2}^+,j})) + \frac{1}{2Fr^2} \begin{pmatrix} 0 \\ \left(\frac{\xi_x}{J} \right)_{i,j} h_{iR,j}^2 - \left(\frac{\xi_x}{J} \right)_{i+\frac{1}{2}^-,j} h_{i+\frac{1}{2}^-,j}^2 \\ \left(\frac{\xi_y}{J} \right)_{i,j} h_{iR,j}^2 - \left(\frac{\xi_y}{J} \right)_{i+\frac{1}{2}^-,j} h_{i+\frac{1}{2}^-,j}^2 \end{pmatrix} \quad (2.44)$$

$$F_{i-\frac{1}{2},j}^+ = F(Q_{i-\frac{1}{2},j}^*(0, Q_{i-\frac{1}{2}^-,j}, Q_{i-\frac{1}{2}^+,j})) \\ + \frac{1}{2Fr^2} \begin{pmatrix} 0 \\ \left(\frac{\xi_x}{J}\right)_{i,j} h_{iL,j}^2 - \left(\frac{\xi_x}{J}\right)_{i-\frac{1}{2}^+,j} h_{i-\frac{1}{2}^+,j}^2 \\ \left(\frac{\xi_y}{J}\right)_{i,j} h_{iL,j}^2 - \left(\frac{\xi_y}{J}\right)_{i-\frac{1}{2}^+,j} h_{i-\frac{1}{2}^+,j}^2 \end{pmatrix} \quad (2.45)$$

$$G_{i,j+\frac{1}{2}}^- = G(Q_{i,j+\frac{1}{2}}^*(0, Q_{i,j+\frac{1}{2}^-}, Q_{i,j+\frac{1}{2}^+})) \\ + \frac{1}{2Fr^2} \begin{pmatrix} 0 \\ \left(\frac{\eta_x}{J}\right)_{i,j} h_{i,jR}^2 - \left(\frac{\eta_x}{J}\right)_{i,j+\frac{1}{2}^-} h_{i,j+\frac{1}{2}^-}^2 \\ \left(\frac{\eta_y}{J}\right)_{i,j} h_{i,jR}^2 - \left(\frac{\eta_y}{J}\right)_{i,j+\frac{1}{2}^-} h_{i,j+\frac{1}{2}^-}^2 \end{pmatrix} \quad (2.46)$$

$$G_{i,j-\frac{1}{2}}^+ = G(Q_{i,j-\frac{1}{2}}^*(0, Q_{i,j-\frac{1}{2}^-}, Q_{i,j-\frac{1}{2}^+})) \\ + \frac{1}{2Fr^2} \begin{pmatrix} 0 \\ \left(\frac{\eta_x}{J}\right)_{i,j} h_{i,jL}^2 - \left(\frac{\eta_x}{J}\right)_{i,j-\frac{1}{2}^+} h_{i,j-\frac{1}{2}^+}^2 \\ \left(\frac{\eta_y}{J}\right)_{i,j} h_{i,jL}^2 - \left(\frac{\eta_y}{J}\right)_{i,j-\frac{1}{2}^+} h_{i,j-\frac{1}{2}^+}^2 \end{pmatrix} \quad (2.47)$$

$$Sc_{i,j} = Sc_{i,j}^\xi + Sc_{i,j}^\eta \quad (2.48)$$

Finally, time integration of the curvilinear NSWE with arbitrary topography is performed with a fourth-order Runge-Kutta scheme described in (Ferziger & Peric, 1996).

2.4.3. Boundary Conditions

To handle the boundary conditions in arbitrarily complex domains with second-order accuracy, we employ two layers of ghost cells outside the computational domain in the numerical model. With this methodology we can estimate the flow variables at the boundary cells and introduce specific dynamic information to the computational domain. Three types of boundary conditions have been implemented and tested in the model, which are

used in the next validation tests: i.) Transmissive or open boundary, establishes a zero-gradient between the boundary and ghost cells state variables, allowing the information to freely leave the domain without propagating spurious information back to the domain; ii.) Solid wall or close boundary, imposes that at the boundary the velocities and the water elevation gradient are equal to zero (no discharge boundary condition); and iii.) *Absorbing/Generating* boundary condition, which relies on the work of Cienfuegos et al. (Mignot & Cienfuegos, 2009; Cienfuegos et al., 2007), allowing to introduce dynamic information inside the domain from the boundary, such as waves or specific hydrographs, and evacuate back-traveling waves. Information is imposed outside the domain and a Riemann problem is solved at the boundary to find the value of flow variables and introduce this information into the computational domain. In the numerical method presented in this research this boundary condition has only been developed for normal incident flow.

2.4.4. Stability Criterion

The stability of the numerical model is controlled by the Courant-Friedrich-Lowy criterion (CFL) (Courant et al., 1928). This principle states that the numerical method must be able to propagate information at a physical speed determined by the eigenvalues of the flux Jacobian matrices. For explicit numerical schemes in cartesian coordinates, it establishes that the Courant number $Cr = u \Delta t / \Delta x$ must be less than 1 ($Cr < 1$) in order to obtain a correct time step for discrete time integration, implying that information will propagate less than one grid cell at a single time step (Leveque, 2002). The latter will ensure stability and convergence to the sought solution. In this case, the time-step is defined in the two-dimensional curvilinear framework as follows:

$$\Delta t = Cr \frac{\min [\Delta\xi, \Delta\eta]}{\max [\max(U^1 + C \sqrt{\xi_x^2 + \xi_y^2})_{i,j}, \max(U^2 + C \sqrt{\eta_x^2 + \eta_y^2})_{i,j}]} \quad (2.49)$$

2.5. Validation of the Model

The numerical model presented herein is a non-orthogonal generalized curvilinear coordinate version of the model described in Marche et al. (2007), with the additional incorporation of bed-friction. The original model has been validated against various benchmark cases in Cartesian coordinates, involving shock-capturing and moving shoreline problems, obtaining quantitatively accurate results in comparison with analytical solutions and laboratory data (Marche et al., 2007). The following validation cases presented in this section are intended to demonstrate the improvement obtained when a boundary-fitted curvilinear discretization is used, and to prove the ability of the model to deal with bed-slope and friction source terms.

2.5.1. Radial Dam-Break

This test involves the hypothetical case of the breaking of a circular dam. The circular wall containing a volume of water is instantly removed at time $t = 0$ s. Then a shock-wave propagates outwards, radially and symmetrically over a horizontal and frictionless bottom, while a rarefaction wave propagates inwards (Alcrudo & García-Navarro, 1993). Due to the symmetry of the problem, this is an interesting test to assess the improvement achieved by using a boundary-fitted curvilinear coordinate discretization of the domain. In order to compare both types of discretizations, Cartesian and Polar, we carry out two simulations with these different discretizations. The Cartesian grid is formed with a regular and uniform mesh of 50×50 cells, each one of dimensions of 1×1 m. On the other hand, the boundary-fitted curvilinear grid has 50×25 cells constructed with polar coordinates; resulting in an orthogonal grid with 50 cells in the tangential direction and 25 cells in the radial direction of 1 m length. The two meshes employed in the calculation are shown in Fig. 2.4.

Fig. 2.5 shows instantaneous contour plots of the free surface at time $t = 0.7$ s using both grids. The differences between them are clearly observed as the computed results obtained with the Cartesian grid are not perfectly symmetric in the radial direction, and several spurious variations of water depth are found between the shock and the rarefaction waves.

The asymmetries can also be observed in the velocity field computed using the Cartesian grid discretization shown in Fig. 2.6(a), where the direction of the shock-wave that is propagated outwards is not perfectly radial. The inaccuracies are completely removed when using a boundary-fitted curvilinear grid, where a perfect circular bore is successfully propagated, and a symmetrical velocity field is obtained (see the contours in Figs. 2.5(b) and 2.6(b)). These results agree well with those of Alcrudo and García-Navarro (1993) and Mingham and Causon (1998). This simple case also illustrates the significant improvement in the computed results when the domain is discretized using a coordinate system that can adapt to the domain. It is important to note that in this case the coordinate system continues to be orthogonal, which simplifies the computation of the metrics and Jacobian matrix of the transformation in Eq. (2.3).

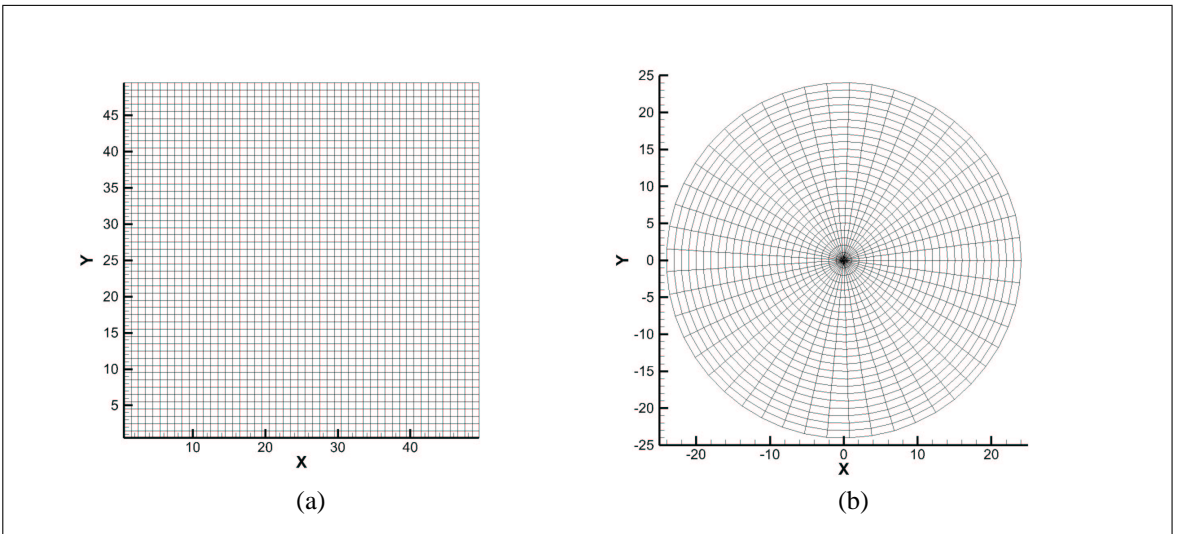


FIGURE 2.4. Radial dam-break. Discretization grids: (a) Cartesian grid, (b) Curvi-linear grid

2.5.2. Supercritical flow in a convergent channel

To demonstrate the full capabilities of the model in shallow inertial flows with non-orthogonal discretizations, we test the numerical model in a flow with supercritical flow and steep waves in a more complex channel geometry. In this case we perform numerical simulations of the steady state supercritical flow through a curved transition, which was first studied experimentally by Ippen and Dawson (Ippen & Dawson, 1951). In the

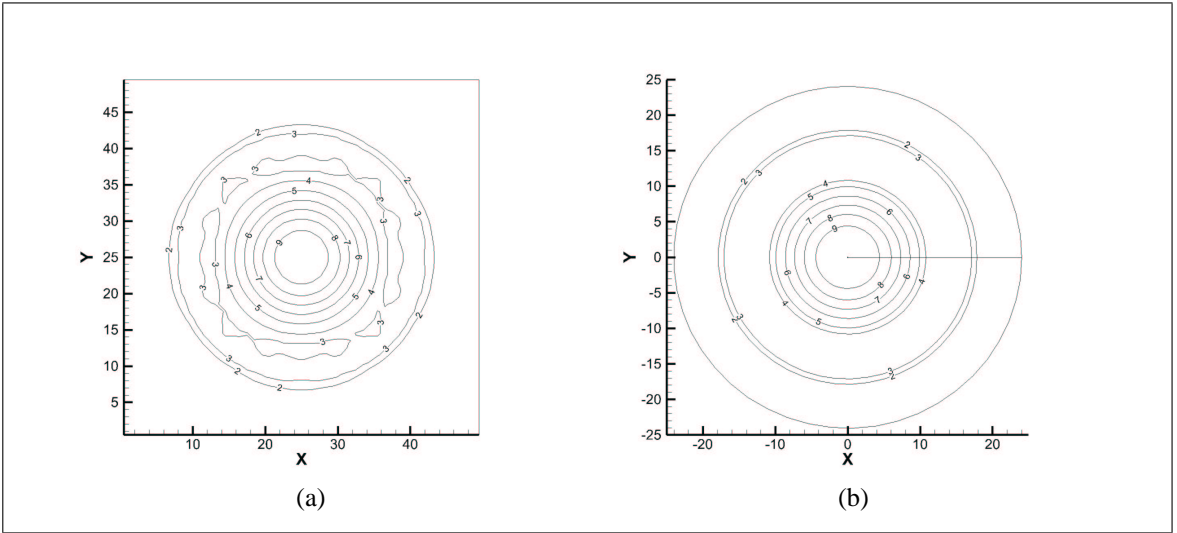


FIGURE 2.5. Radial dam-break. Contour plot of computed free surface at $t=0.7$ s,
(a) Using cartesian grid, (b) Using curvilinear grid

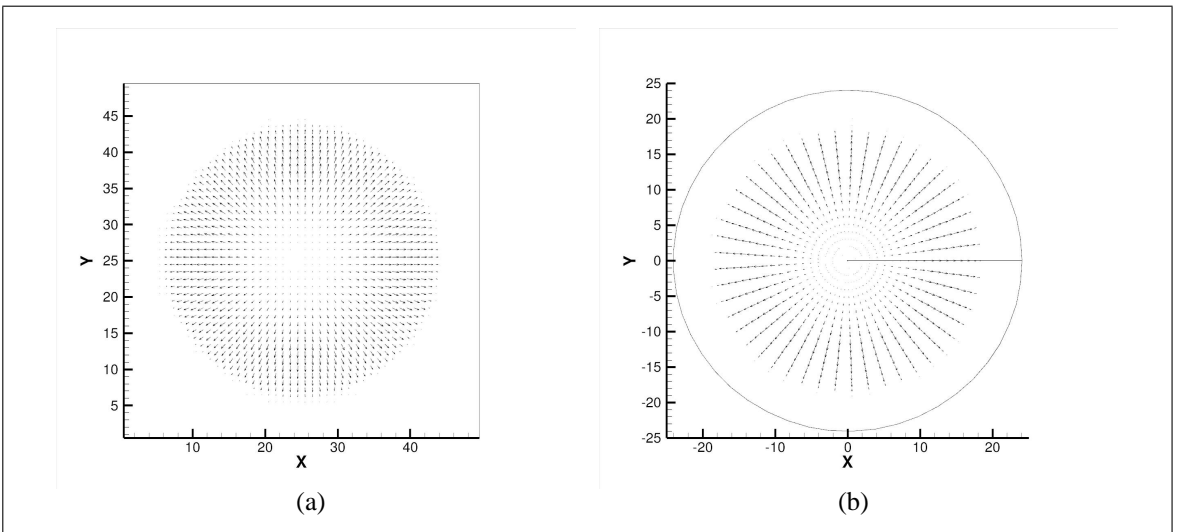


FIGURE 2.6. Radial dam-break. Computed velocity field at $t=0.7$ s, (a) Using cartesian grid, (b) Using curvilinear grid

channel, two rectangular sections are connected by a converging transition. According to Causon and Mingham (1999), the dimensions of the contraction should be corrected from those originally reported by Ippen and Dawson (1951), since two errors were found in the dimensions quoted in Ippen and Dawson (1951) when Causon and Mingham (1999) derived the describing equations for this channel configuration . The corrected contraction length is 1.067 m and it consists in two equal, but opposite circular arcs with a central

contact angle of 16.26° (Causon & Mingham, 1999). The simulation was carried out using a non-uniform boundary-fitted mesh of 450×100 cells and the channel was assumed to be flat and frictionless as in previous numerical investigations (D. Liang et al., 2007). The geometry of the channel and the numerical mesh are shown in Figs. 2.7 and 2.8.

Inflow conditions in the channel consist on a water depth of 0.03 m and a flow velocity of 2.7 m/s, which corresponds to a supercritical flow with a Froude number equal to $Fr = 4.0$. The same inflow conditions are introduced into the computational domain using the Absorbing/Generating boundary condition (Mignot & Cienfuegos, 2009; Cienfuegos et al., 2007). No-flow boundary condition was imposed at the sidewalls, and at the downstream end of the channel an open boundary condition is applied to allow all the information to exit the domain without propagating back and perturbing the numerical solution. The simulations were carried out until reaching a steady state using a CFL number equal to 0.5 in order to ensure numerical stability during the computation.

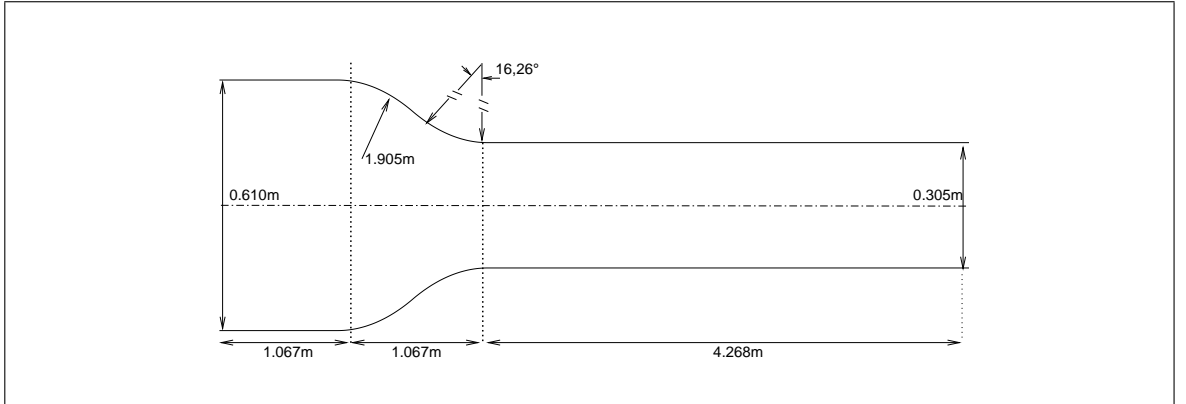


FIGURE 2.7. Convergent channel. Geometry of the channel

All the features observed in the experiments are successfully captured in the numerical simulation (see the comparisons in Figs. 2.9(c) and 2.9(d)). At the beginning of the contraction, detached oblique shock-waves are formed at each sidewall and reflected to the center of the section, where they cross to hit the opposite sidewall. The interaction of these oblique shocks produces standing waves in the channel, increasing locally the water height. The reflection and superposition of these waves repeat themselves towards the end of the channel, forming the diamond wave-pattern shown in Fig. 2.9.

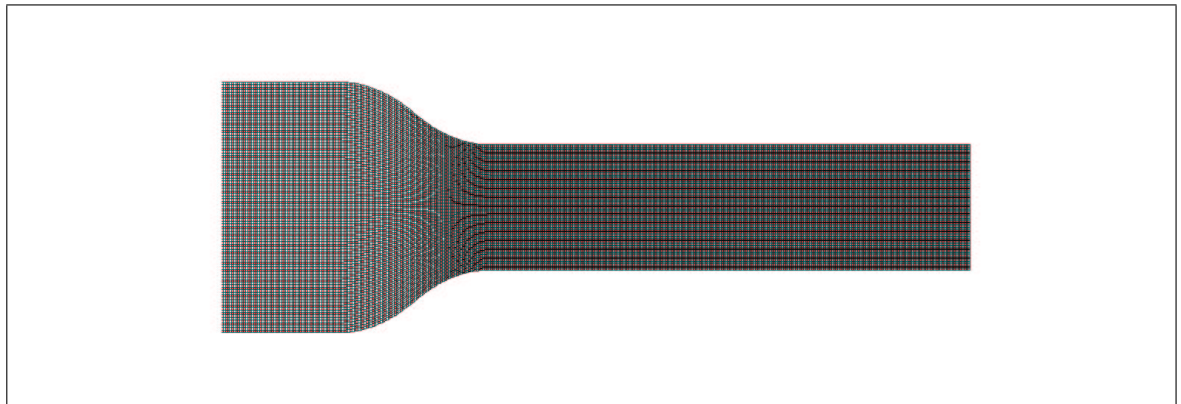


FIGURE 2.8. Convergent channel. Boundary-fitted grid

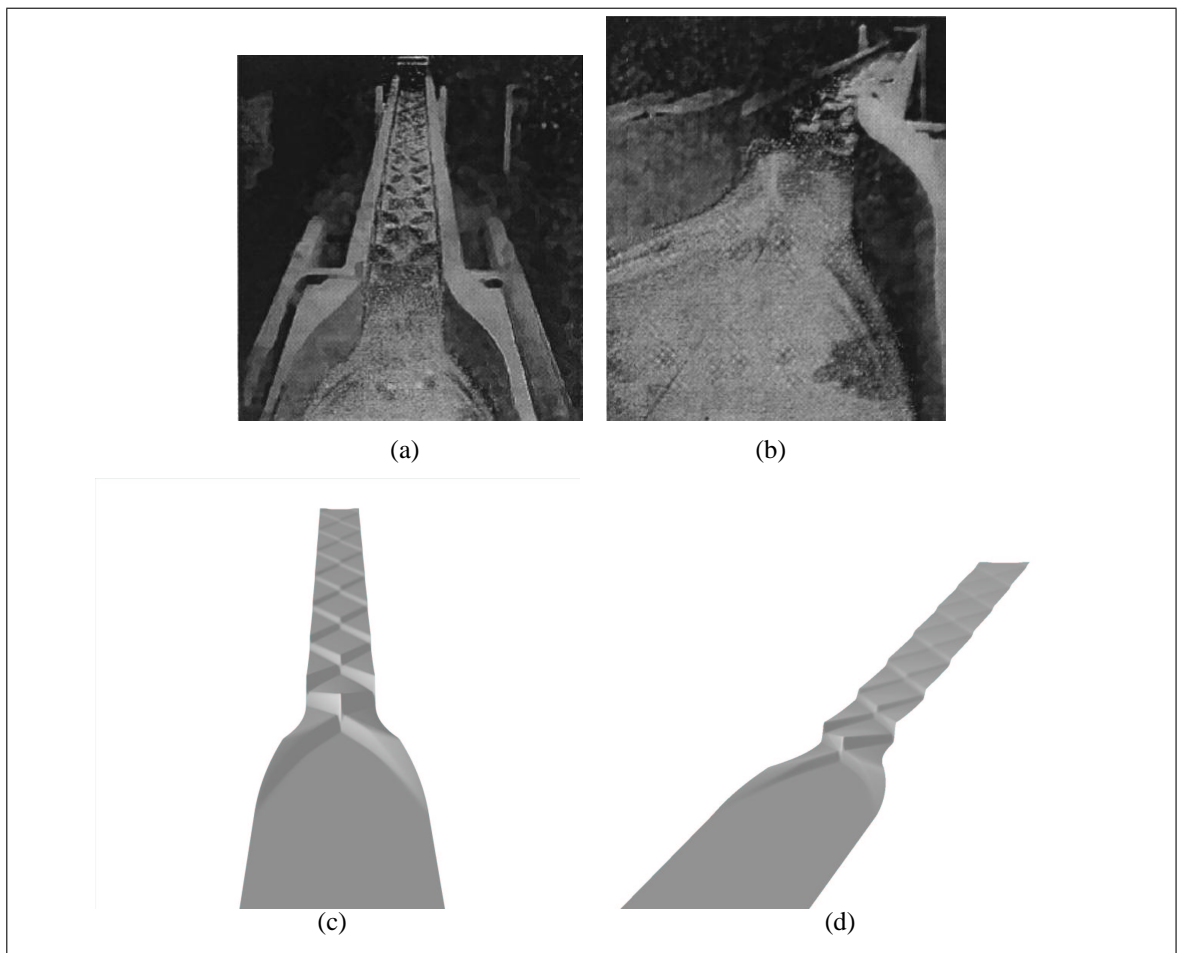


FIGURE 2.9. Convergent channel. Steady state wave pattern. (a) & (b) Laboratory Experiments of Ippen and Dawson (1951), (c) & (d) Computed free surface

Computed water depths are in excellent agreement with experimental data for the first shock wave at the middle and at the sidewalls of the channel. Nevertheless, as the flow progresses downstream the numerical model produces steeper fronts than observed in the experiment, and increasing differences in amplitude and location of the wave crests are found towards the outlet (Figs. 2.10(a) and 2.10(b)). Similar results were obtained by Causon and Mingham (1999), where the shallow water equations were solved using a Godunov-type upwind scheme, and by D. Liang et al. (2007), where curvilinear shallow water equations are solved using the MacCormack scheme. These differences should be attributed to the hydrostatic pressure assumption of the shallow-water equations, which might no longer be valid near quasi-periodic shock waves. Improvements have been found when vertical velocity variations and non-hydrostatic pressure profiles are considered (Kruger & Rutschmann, 2006) and much better results were obtained when solving Navier-Stokes equations for this problem (Aliabadi et al., 2002), which would indicate that viscosity might have an important effect on the attenuation of the waves downstream of the channel. Despite the differences found in the downstream flow pattern, the shallow-water equations can still do a good job in predicting the first cross shock-wave where the maximum water depth occurs. This feature is the most important value to be considered in investigations where overflow needs to be prevented.

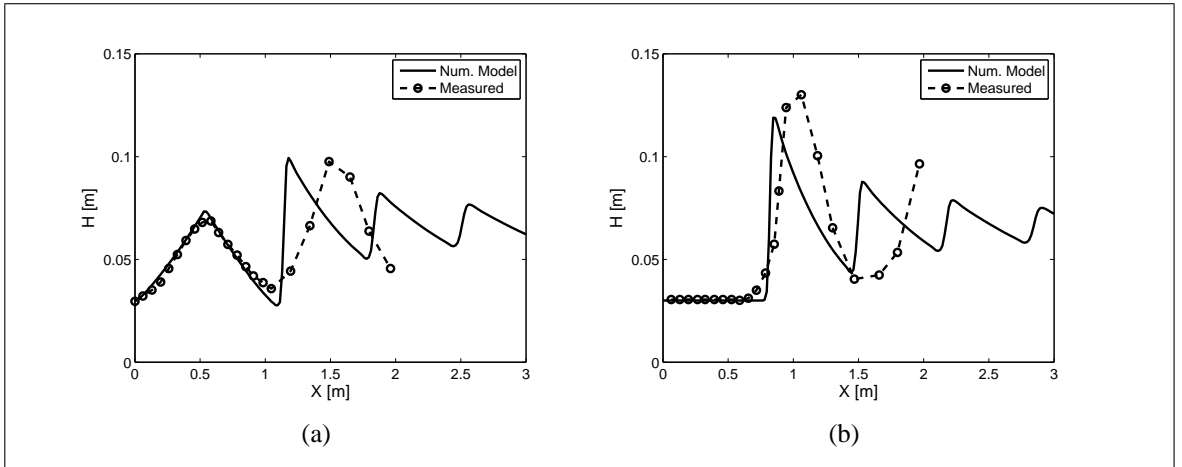


FIGURE 2.10. Convergent channel. Measured and computed water depths at steady state, (a) along the sidewall, (b) along the middle of the channel section

2.5.3. 1D Oscillating water column over a parabolic basin with friction

An important characteristic of the model is its capability of handling frictional source terms in the numerical solution of the NSWE, especially in situations where the flow is shallow or when the process of wave run-up/run-down is important. Here we test the numerical model with the analytical solution of the oscillation inside a parabolic basin with friction to assess the ability of the methodology developed in this research to deal with steep bed-slopes and friction source terms. We also aim at demonstrating its success in managing the wetting and drying process and to reach and preserve the steady states. The chosen benchmark test was also used in Q. Liang and Marche (2009) to validate the semi-implicit friction step proposed to incorporate the additional source term in the momentum equations. Sampson et al. (2006) found an exact analytical solution to the shallow-water equations in 1D for the flow above a parabolic topography with friction. This solution was derived from the Thacker's solutions for oscillations over a parabolic basin (Thacker, 1981), assuming that velocity only depends on time and it is only in one direction ($u = u(t)$, $v = 0$). The motion decays over time as expected for flows with frictional damping (Sampson et al., 2006).

The parabolic topography is defined by,

$$z = h_0(x/a)^2 \quad (2.50)$$

where h_0 is the still water level and a is a constant. The origin for x is at the center of the basin. The analytical solution for the free surface, denoted as $\zeta(x, t)$, and used to compare the numerical predictions, is given by:

$$\begin{aligned} \zeta(x, t) = & h_0 + \frac{a^2 B^2 e^{-\tau t}}{8g^2 h_0} \left[-s\tau \sin(2st) + \left(\frac{\tau^2}{4} - s^2 \right) \cos(2st) \right] \\ & - \frac{B^2 e^{-\tau t}}{4g} - \frac{e^{-\tau t/2}}{g} \left[Bs \cos(st) + \frac{\tau B}{2} \sin(st) \right] x \end{aligned} \quad (2.51)$$

where B is a constant and p is a hump amplitude parameter given by $p = \sqrt{8gh_0/a^2}$. Friction is represented by the τ parameter, which is related to the bed friction coefficient C_f such that $C_f = h\tau/|u|$. Finally, the frequency s is defined through the relation given by

$s = \sqrt{p^2 - \tau^2}/2$, where τ must be less than the hump amplitude p (Q. Liang & Marche, 2009).

The simulation is performed over a 10,000 m length parabolic basin, discretized with 200 uniform cells. The chosen parameters for this case are $a = 30.0$ m, $h_0 = 10$ m, $\tau = 0.001$ s⁻¹ and $B = 5$ m/s. No boundary conditions are needed for this case as the initial condition evolves until reaching a motionless state. Computations were carried out for 10,000 s in order to achieve steady state as shown in previous investigations (Q. Liang & Marche, 2009).

Comparisons between analytical and numerical results at different instants in time are depicted in Figs.(2.11) and (2.12). Excellent agreement is found in the amplitude of the free surface oscillations, which correctly decays in time as a consequence of the friction force. It reaches the rest level h_0 after nearly 10,000 s. Interaction between dry and wet cells is also represented with high accuracy, and no numerical problems are observed. Therefore, the robustness and stability of the friction scheme in conjunction with the well-balancing properties of the solution of the hyperbolic system are validated.

2.6. Conclusions

In this investigation we have developed and validated a finite-volume numerical model to simulate shallow inertial flows described by the NSWE using a non-orthogonal curvilinear coordinate systems. The numerical scheme successfully reproduces the flow hydrodynamics over rough and highly varying topographies, and it is capable to incorporate complex boundary geometries to represent correctly wetting and drying processes over arbitrary domains. The method is based on the methodology proposed by Marche et al. (2007) and it is adapted here to solve the bed-slope source term and to incorporate the friction at the bed by using the splitting semi-implicit scheme developed by Q. Liang and Marche (2009).

Three validation test cases are considered to illustrate the capabilities of the new model. Test cases involve the use of boundary-fitted grids, frictional and varying bathymetry, supercritical flow, and shock-waves. The advantages of using boundary fitted grid is shown

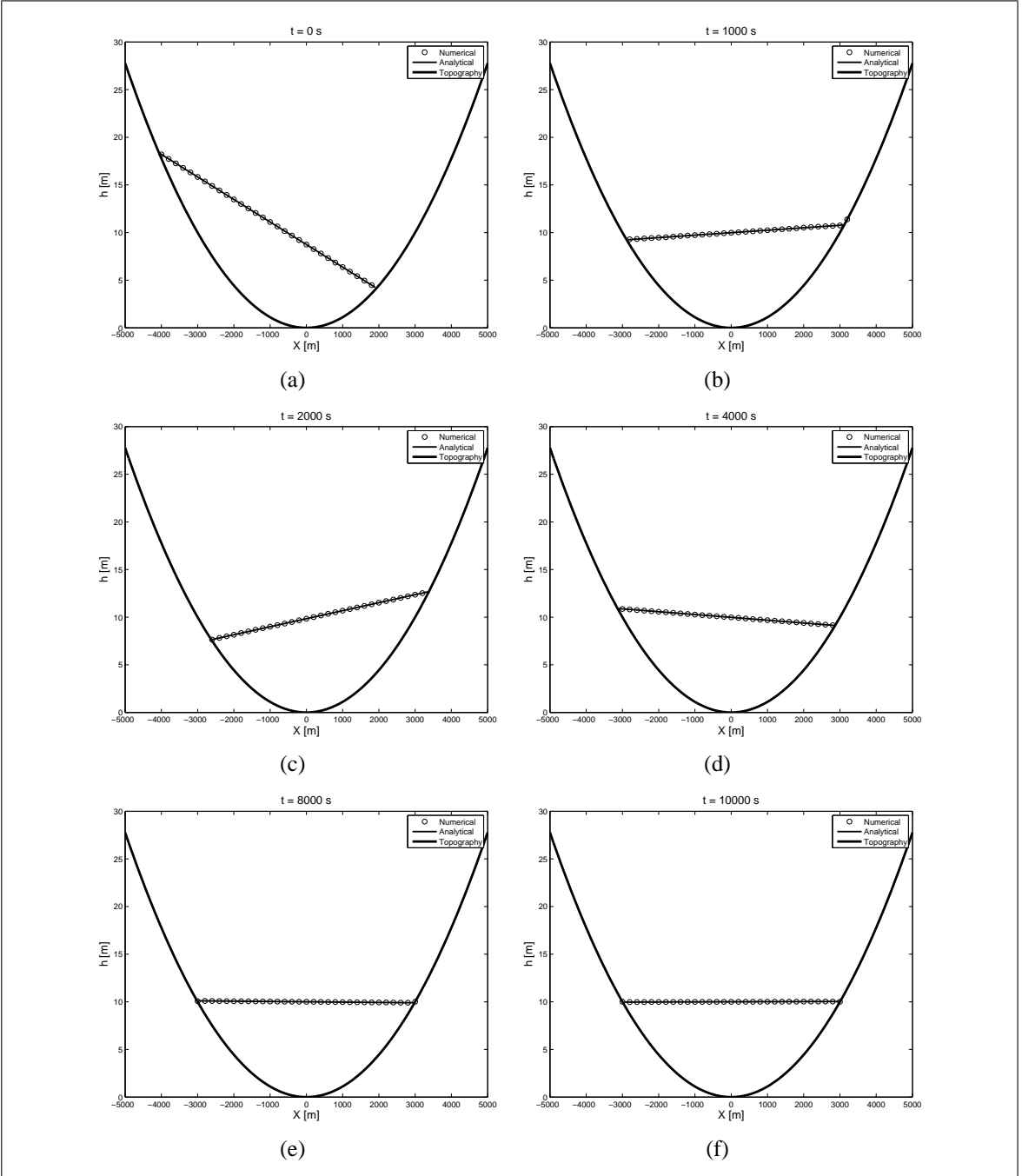


FIGURE 2.11. 1D Oscillating water column. Free surface at different times

for the case of the cylindrical dam-break (Alcrudo & García-Navarro, 1993). The generalized curvilinear coordinate formulation is employed to discretize the domain in polar coordinates, showing a significant improvement of the numerical solution compared to the

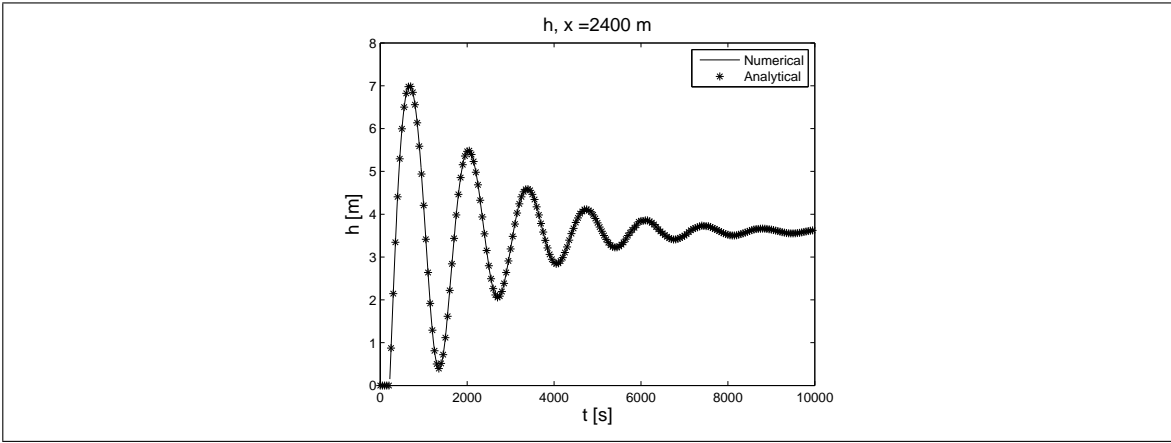


FIGURE 2.12. 1D Oscillating water column. Time series for the water depth at $X = 2400$ m

results obtained with the Cartesian mesh. Supercritical flow and standing shock-wave patterns observed in the experiments of Ippen and Dawson (1951) in a converging channel discretized with a non-orthogonal grid are well reproduced. The computed water elevation shows an excellent agreement with experimental data at least for the first shock-wave, while differences are found downstream in the channel due to the errors induced by the hydrostatic and inviscid assumptions embedded in the NSWE. Wetting and drying process over a frictional parabolic basin (Q. Liang & Marche, 2009) are correctly represented and excellent agreement is also found compared to analytical solutions.

The results reported in this research confirm that the numerical method is a powerful and effective tool that can be used to model extreme and rapid flood events over complex bathymetry in cases such as dam-breaks (Valiani et al., 2002), glacial lake outburst floods (GLOF) (Dussaillant et al., 2009) or tsunamis (Synolakis & Kong, 2006). We are currently carrying out scaled laboratory experiments over realistic bathymetries to investigate the propagation of flood waves generated by the rapid emptying of a reservoir over a river reach. A numerical investigation using our model for the NSWE will be carried out to predict the effects of the propagated flood wave (free surface elevation and inundation zones), and to test the abilities of the model for conditions similar to reality. The results of this study will be reported in a future publication.

Future research using the same methodology developed in this investigation will focus on the study of complex engineering and geophysical flows. This model will be employed to investigate density-coupled flows, incorporating the transport of active and passive contaminants in rivers and estuaries (Loose et al., 2005). Also, advanced sediment transport and morphodynamic models (Cao et al., 2004; Vasquez et al., 2008) will be added to the basic equations of the flow to study erosion and sedimentation processes in fluvial and coastal environments.

2.7. Acknowledgements

The authors would like to thank F. Marche for the guidance in the use of the SURF_WB model and the orientation in the implementation of the curvilinear coordinate model. Also thanks the financial aid provided by the Fondecyt project N°11060312 and the ECOS-Conicyt project C07U01.

3. PHYSICAL AND NUMERICAL MODELING OF INERTIA-DOMINATED FLOOD WAVES

3.1. Abstract

Extreme flash floods have been more frequent in the last decades, probably due to the global warming phenomena. These extreme events challenge the classic engineering practice and call for new methods to quantify flow variables as well as their impacts with the purpose of improving the design of infrastructure and to define risk zones, diminishing the potential damage of the flood. In the Chilean South Patagonia, glacial lake outburst floods (GLOF), for example, have been unexpectedly recurrent over the last couple of years (Chilean Cachet II lake has emptied 5 times since 2008, (Dussaillant et al., 2009)). In the laboratory, this phenomenon can be modeled in a simplified manner as the instant discharge of a water volume contained in a reservoir to a river reach, similar to a dam-break. This paper presents the results of a laboratory experiment of this kind carried out at the Hydraulic Engineering Laboratory at the *Pontificia Universidad Católica de Chile*. Experimental data is then used to evaluate the abilities of the numerical model developed in Chapter 2, which solves a set of curvilinear nonlinear shallow water equations. The numerical model is a well-balanced and robust finite volume scheme that considers bed-slope and friction in the source terms especially developed to predict the dynamics of shallow inertial flows. It has shock-capturing ability and can handle flows over strongly variable topography and complex geometries using a non-orthogonal boundary-fitted discretization of the domain. Results show that the numerical model is able to qualitatively describe the flooding process and good estimations of the peak amplitudes, arrival times and recession curves are found through the river reach. This kind of experience is a demanding test for any numerical model that could represent it.

3.2. Introduction

In recent years the need of understanding and modeling the effects of natural extreme events, such as floods, tsunamis or glacial lake outburst floods (GLOF), has grown. Indeed, they have enormous consequences in terms of damage to infrastructure, human lives and the environment. These events, which seem to be more frequent, challenge the classic engineering practice and call for new methods in order to improve the protection of human settlements. It is paramount to have a good estimation of the relevant hydrodynamic involved.

In Chile, several floods produced by GLOF in the Aysén region have occurred in the last couple of years (Dussaillant et al., 2009). Indeed, in april and october 2008, two major events occurred in the Colonia river, a tributary of the Baker river, as a consequence of the Cachet-II lake outburst. In both events, an increase in the Baker river free surface, above 4.5 m, and in its peak discharge, over $3000 \text{ m}^3/\text{s}$, was generated after the confluence with the Colonia river¹. Besides, in 2007, an 6.2 earthquake (USGS, 2007). produced an important landslide over the sea in the Punta Cola zone near Puerto Chacabuco, generating 6 m waves that propagated through the fjords Finally, in February 2010, the 8.8 earthquake (USGS, 2010), generated a tsunami that hit the Chilean coast from the V to the IX regions, with waves up to 10 m in Constitución and a 2.7 m sea level rise in Talcahuano (Farias et al., 2010)

Around the world more examples of extreme flooding can be found, such as the collapse of the Malpasset dam in the south of France, which have been studied by several researchers because maximum water elevation in surrounding areas is available (Hervouet, 2000; Valiani et al., 2002; D. Liang et al., 2007). Similarly, in northeastern China, took place one of the worst flooding in more than a decade (BBC, 2010). According to public reports almost 1000 people have died and 500 are missing. Indeed, a maximum flow rate of $70000 \text{ m}^3/\text{s}$ hit the Yangtze river, where a mayor amount of water has to be released from

¹DGA Satellite monitoring station at Baker River

the Three Gorges dam, since the floods raised the level of water in its reservoir up to 185 m (maximum is 175 m) (BBC, 2010).

These examples reaffirm the need to develop modeling tools that can accurately describe shallow inertial flows in detail and thus contribute to the design of infrastructure, operation of hydraulic facilities, or to the definition of risk zones in order to diminish the potential damages of fast flooding. Moreover, it is important to consider that it is highly probable that the recurrence of these events continues to increase in the future due to the Global Warming phenomena.

Numerical modeling of free surface flows, constitutes then a valuable tool to evaluate the consequences of this type of events. However, the accurate representation of shallow inertial flows requires specific mathematical techniques, due to the topographical features and complex boundaries of the zones where they occur, the discontinuities that might appear and the flooding of surrounding areas. These features are not correctly captured by standard numerical methods.

The main objective of this paper is to prove that the numerical model developed in Chapter 2 is a trustable and robust tool to represent flash extreme flooding under challenging conditions. Thus, the numerical model is tested against new experimental data associated to the propagation of a flood wave generated by the rapid emptying of a reservoir over a scale river model. Laboratory experiments were performed at the Hydraulic Engineering Laboratory of the *Pontificia Universidad Católica de Chile*, with the technical support of the *Instituto Nacional de Hidráulica* (INH). The obtained data allows us to evaluate the behaviour of the model for conditions similar to reality that incorporate the above features and complexities. This work focuses on both, the outcome of the experience, and on the abilities of the model to reproduce the propagation of the bore downstreams of the reservoir.

The paper is organized as follows. In section 3.3.1 we present the details of the laboratory experiments and the post-processing of the data is shown in section 3.3.2. The numerical model and its application to the dam-break experiment are described in section

3.3.3. Numerical results and comparisons with experimental data are presented in section 3.4. Finally, conclusions and future perspectives of this work are presented in section 3.5

3.3. Methods

3.3.1. Experimental Set-Up

Dam-break experiments were carried out in a scaled river reach constructed at the Hydraulic Engineering Laboratory of the *Pontificia Universidad Católica de Chile*. This physical model has been prepared to simulate unsteady flow over strongly variable topography.

The river reach is 16 m long and 4.5 m wide, it starts with a narrow and curved zone of adverse average bed-slope -2.4% , but it becomes wider towards its downstream end, with zones of adverse and favourable bed-slopes, ranging between $\pm 8\%$. The average bed-slope over the considered river reach is -0.8% . A longitudinal profile of the river reach is shown in Fig. 3.1. Upstream of the river model, there is a reservoir and a gate that holds a fixed volume of water that can be suddenly released by manual operation of the gate (see Fig. 3.2).

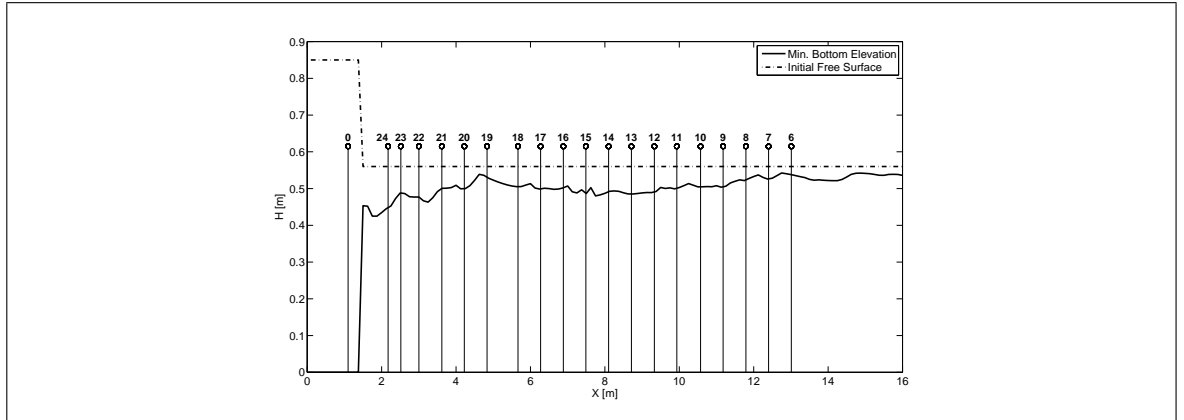


FIGURE 3.1. Dam-break Experience: Longitudinal profile of the river reach bottom elevation, initial conditions and measurement points

The experience consisted in suddenly open the reservoir gate to release a fixed volume of water into a quiescent free surface downstreams. Then a bore was generated and propagated to the end of the river reach, producing fast free surface variations that were recorded



FIGURE 3.2. Dam-break Experience: (a) Physical Model, (b) Experimental Set-up and Reservoir

during 60 s. Experimental set-up and the measurement instruments are shown in Figs. 3.2 and 3.3.



FIGURE 3.3. Dam-break Experience: Resistive Gauges

Free surface variations at the reservoir were measured using a KPSI brand pressure transducer recording voltage at 100 Hz. The accuracy of this instrument is $\pm 1\%$. It was calibrated so that 1 V equals 1 cm of water column. At downstream sections, free surface variations over the mean water level were measured using wave DHI resistive gauges,

which were located at the talweg of the cross sections studied. Every gauge records voltage data at 100 Hz, the accuracy of these gauges is ± 1.5 mm and the zero drift is $\pm 5\%$, depending on water temperature.

Initial conditions in fixing the free surface elevation at 0.85 m inside the reservoir and at 0.56 m at the river (see Fig.3.1). Free surface variations were recorded at nineteen points in the river reach (see Fig. 3.1). Four resistive gauges were available, i.e. only four points could be measured at the same time. Thus, five set of experiences were performed in order to complete the nineteen considered sections. As a verification of the measured data, three repetitions were performed at each gauge location, maintaining the position of the pressure sensor, in order to use its data as a reference and to synchronize the time series.

3.3.2. Post-Processing of the data

A preliminary analysis of the raw data is presented below in order to show the magnitude and propagation of the flooding wave. Time series of free surface variations at the reservoir and three section downstreams the river reach will be studied (S23, S20 and S12).

Reservoir measurements show an accelerated drop of the free surface level, decreasing 0.2 m in 10 s. The final reservoir level rounds the 0.6 m (Fig. 3.4(a)). In the first studied measurement point (S23), located 0.97 m downstream from the reservoir exit, the wave front arrives at 1.5 s. In this time series two amplitude peaks of 0.1 m are observed, which are detected at 1.9 s and 8.4 s (Fig. 3.4(b)). At the point S20, 2.8 m downstream from the exit, the wave front is detected 2.5 s after the dam-break, only one peak of 0.13 m was detected at 5.3 s (Fig. 3.4(c)). Finally, downstream of the channel, at point S12, 7.9 m from the reservoir gate, the front arrives after 6.5 s and the maximum peak measured was 0.09 m of amplitude after 7 s (Fig. 3.4(d)). After the peaks were detected at every measurement point, the free surface started to uniformly decrease, reaching 0.57 m of altitude.

In order to compare the recorded data with further numerical results, it has to be post-processed.

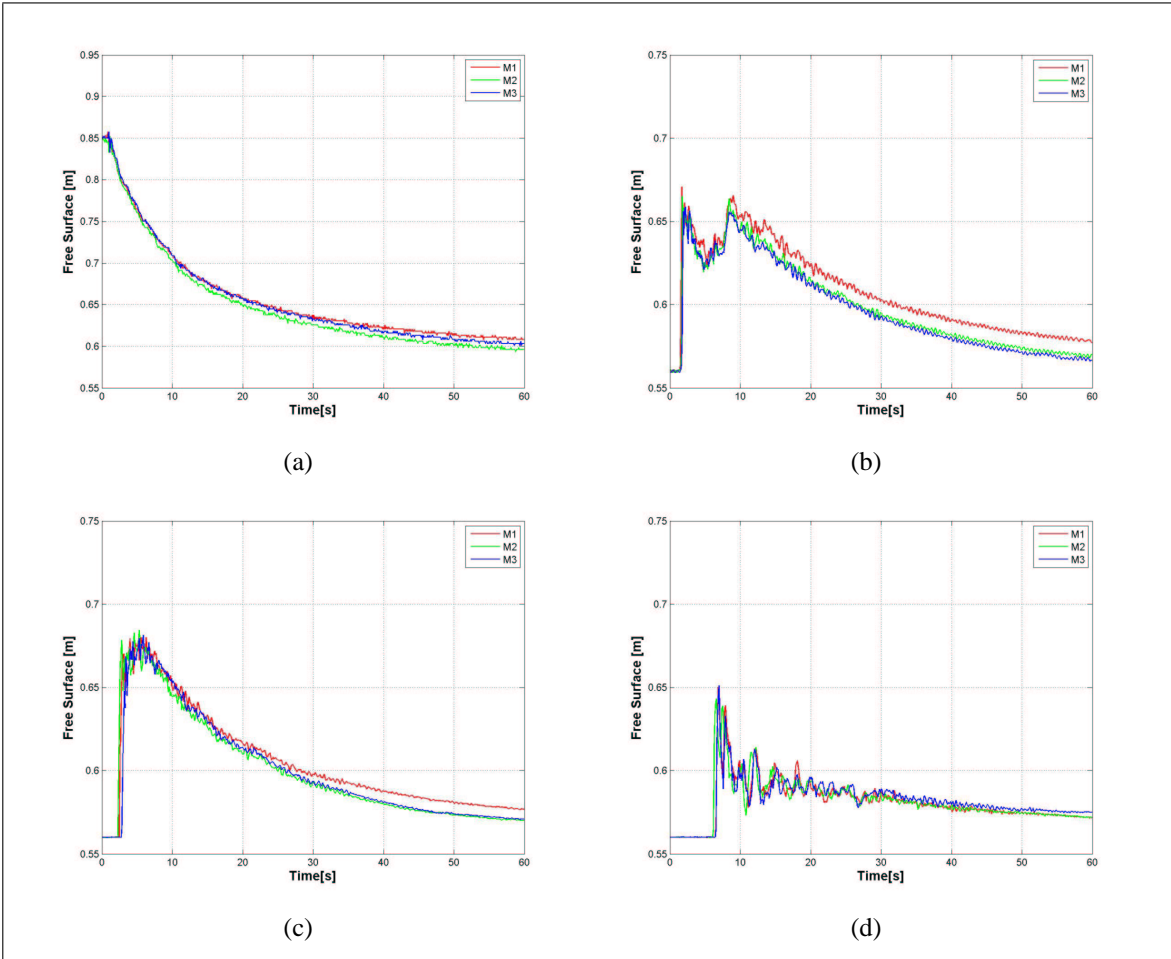


FIGURE 3.4. Time Series of Free surface Measurements at different locations: (a) Reservoir, (b) Point 23, (c) Point 20, (d) Point 12

Since, several repetitions of the same experiment were performed moving the resistive gauges and the measurements did not start exactly with the gate opening at every repetition of the experiment, recollected data must be synchronized. First, all the reservoir recorded data, i.e. off every repetition of the experiment, was synchronized using the first recorded time series as a reference. The lag time between each reservoir time series and the first one was calculated using the Cross-covariance function of Matlab. The corresponding lag time was used to adjust in time every time series of the free surface variation at each gauge location according to each experiment and repetition.

Finally, due to the high velocity of the propagated flood wave, resistive gauges vibrate. This vibrations are traduced into small oscillations in the signal, in order to remove spurious

oscillations of the data due to signal noise or vibrations of the resistive gauges, a low-pass digital Butterworth filter was applied using a cutoff frequency of 0.1.

3.3.3. Numerical Modeling

3.3.3.1. Numerical Model

The obtained data from the dam-break laboratory experience will be used to test the abilities of the numerical model presented in Chapter 2, which has shock-capturing ability, and manages subcritical and supercritical flows over strongly variable topography with complex boundaries using a boundary-fitted discretization of the domain. The numerical model solves the nonlinear shallow water equations (NSWE) (3.1) considering bed-slope and friction in the source terms, written under a boundary-fitted set of curvilinear coordinates (ξ, η) . The NSWE written in dimensionless variables are:

$$\frac{\partial Q}{\partial t} + J \frac{\partial F}{\partial \xi} + J \frac{\partial G}{\partial \eta} = S(Q) \quad (3.1)$$

where

$$Q = \begin{pmatrix} h \\ hu \\ hv \end{pmatrix}, F = \frac{1}{J} \begin{pmatrix} hU^1 \\ uhU^1 + \frac{1}{2Fr^2}h^2\xi_x \\ vhU^1 + \frac{1}{2Fr^2}h^2\xi_y \end{pmatrix}, G = \frac{1}{J} \begin{pmatrix} hU^2 \\ uhU^2 + \frac{1}{2Fr^2}h^2\eta_x \\ vhU^2 + \frac{1}{2Fr^2}h^2\eta_y \end{pmatrix}, \quad (3.2)$$

$$S = \begin{pmatrix} 0 \\ -\frac{h}{Fr^2}(z_\xi\xi_x + z_\eta\eta_x) - S_{fx} \\ -\frac{h}{Fr^2}(z_\xi\xi_y + z_\eta\eta_y) - S_{fx} \end{pmatrix}$$

where h represents the water height, u and v are the dimensionless Cartesian components of the velocity; z defines the bed elevation, z_ξ and z_η define the bed slope with respect to the curvilinear coordinate system, S_f represents the friction source term, and $Fr = U/\sqrt{gH}$ is the Froude number defined by the characteristic velocity and vertical scales of the problem, U and H , and the acceleration of gravity g . ξ_x , ξ_y , η_x , and η_y are the resulting metrics associated to the coordinate system, and $J = \xi_x\eta_y - \xi_y\eta_x$ is the Jacobian of the

transformation, which will remain constant for a fixed grid. U^1 and U^2 are the contravariant velocity components, and are expressed as $U^j = u\epsilon_x + v\epsilon_y$ with $(j, \epsilon) \in (1, \xi), (2, \eta)$.

NSWE are solved using a well-balanced finite volume scheme that separately incorporates the effects of both source terms. Friction is solved using a implicit splitting scheme presented in (Q. Liang & Marche, 2009). Nonlinear shallow water equations with topographic variations are solved with the method proposed in Marche et al. (2007). This scheme combines the approximate Riemann Solver VF Roe-ncv (Gallouet et al., 2003b) for the homogeneous problem, with the MUSCL type hydrostatic reconstruction method (Audusse et al., 2004) to balance the bed-slope source term.

The numerical model, includes different boundary conditions, solid reflective wall, transmissive, periodic and absorbing/generating boundary condition. Time integration is solved with a fourth order Runge-Kutta scheme and stability is controlled by the Courant-Friedrich-Lowy condition, which establishes the time step for the integration scheme. The numerical model has been validated against analytical solutions and laboratory data, and a wide range of problems that involve variable topography, dam-break phenomena and complex geometries.

3.3.3.2. Numerical Simulation

Numerical modeling of the experiments requires a digital discretization of the river bathymetry and the reservoir, and initial and boundary conditions.

Bathymetric profiles of the physical model were recollected and then interpolated to create the grid using the *griddata* function of Matlab. As a first attempt to model the experiment, a regular and uniform Cartesian grid was used. The physical model was discretized into 129 x 37 square cells of size $\Delta x = \Delta y = 0.125$ m. A three dimensional view of the model bathymetry is shown in Fig. 3.5.

Computational initial conditions were 0.85 m of free surface elevation at the reservoir and 0.56 m at the river reach, and null velocities over the entire domain were considered. Bed-roughness was not considered in the simulations. Open boundary condition was used at the downstream end of the river reach and close boundary condition was applied to the

other sides of the domain, CFL condition was set to 0.8 in order to ensure the numerical stability of the simulations.

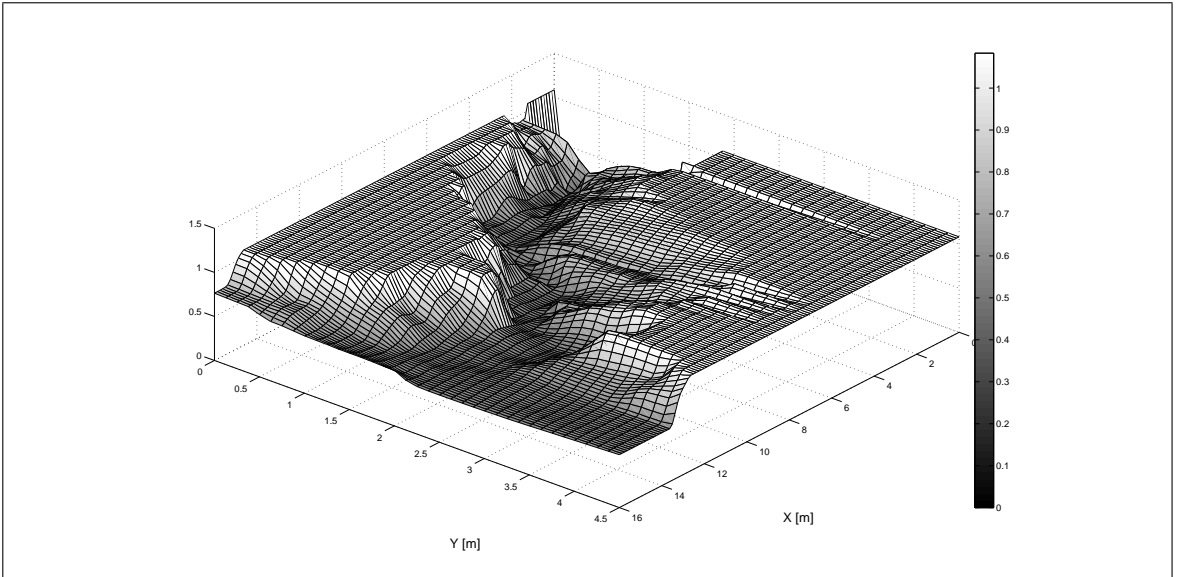


FIGURE 3.5. Dam-break Experience: Digital physical model bathymetry

3.4. Results

Qualitatively, the numerical model was able to simulate the dam-break event and the propagation of the flood waves over the river model. The main features of the rapidly varying flow were reproduced by the numerical model. Discontinuities observed in the laboratory experiment, such as hydraulic jumps, recirculation and reflection due to topographical obstacles are clearly observed in the numerical results. The model was also able to flood the dry areas and to converge to the steady state. Fig. 3.6 shows a three dimensional view of the free surface 3.1 s after the gate opening, in which the propagated flood wave train surface can be appreciated.

Based on the obtained results, three variables were studied: arrival time of the wave front, maximum amplitudes and the total volume of water per unit area under each gauge after 60 s of simulation. Comparisons between measured and numerical time series of the free surface at the studied measurement points are shown in Fig. 3.7. This figure shows

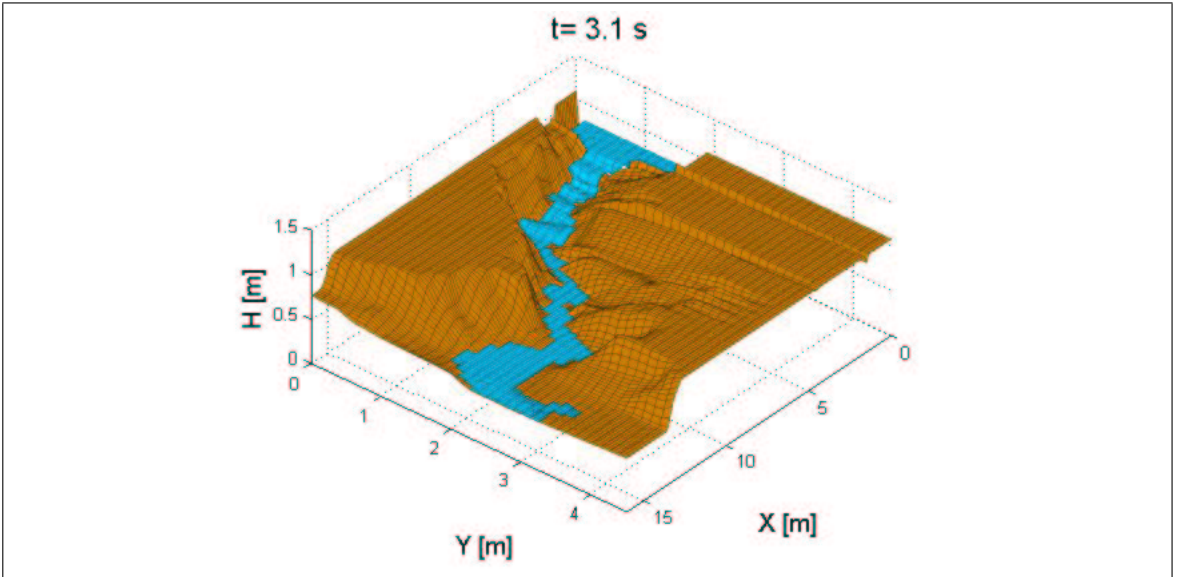


FIGURE 3.6. Dam-break Experience: Effects of the dam-break over the river free surface at $t = 3.1$ s

that the main features of the flood, arrival time and peak amplitude, agree well with the experimental data.

Quantitative comparisons of the numerical results with the experimental data are shown in Fig. 3.8. Fig. 3.8(a) compares the arrival time of the wave front for every measurement point; Fig. 3.8(b), the maximum amplitude peaks, and Fig. 3.8(b), the volume per unit area under each gauge.

It was verified that the arrival times of the wave front to the measurement points (virtual gauges) are well reproduced by the numerical model, a 7.2% relative error was calculated for the last measurement gauge. Predicted results indicate that the wave front will move faster at the beginning of the river, reaching the first studied virtual gauge (Point 23) 0.7 s after the dam-break. Downstream, the numerical model predicts a deceleration of the front, arriving at similar times at point 12. This difference may be explained by the opening mechanism of the gate, which is instantaneous in the numerical model but is done in a finite time in the experience.

As for the magnitude of the observed peaks, differences vary within the studied point. The numerical model underestimates the maximum amplitudes in most cases, but not the

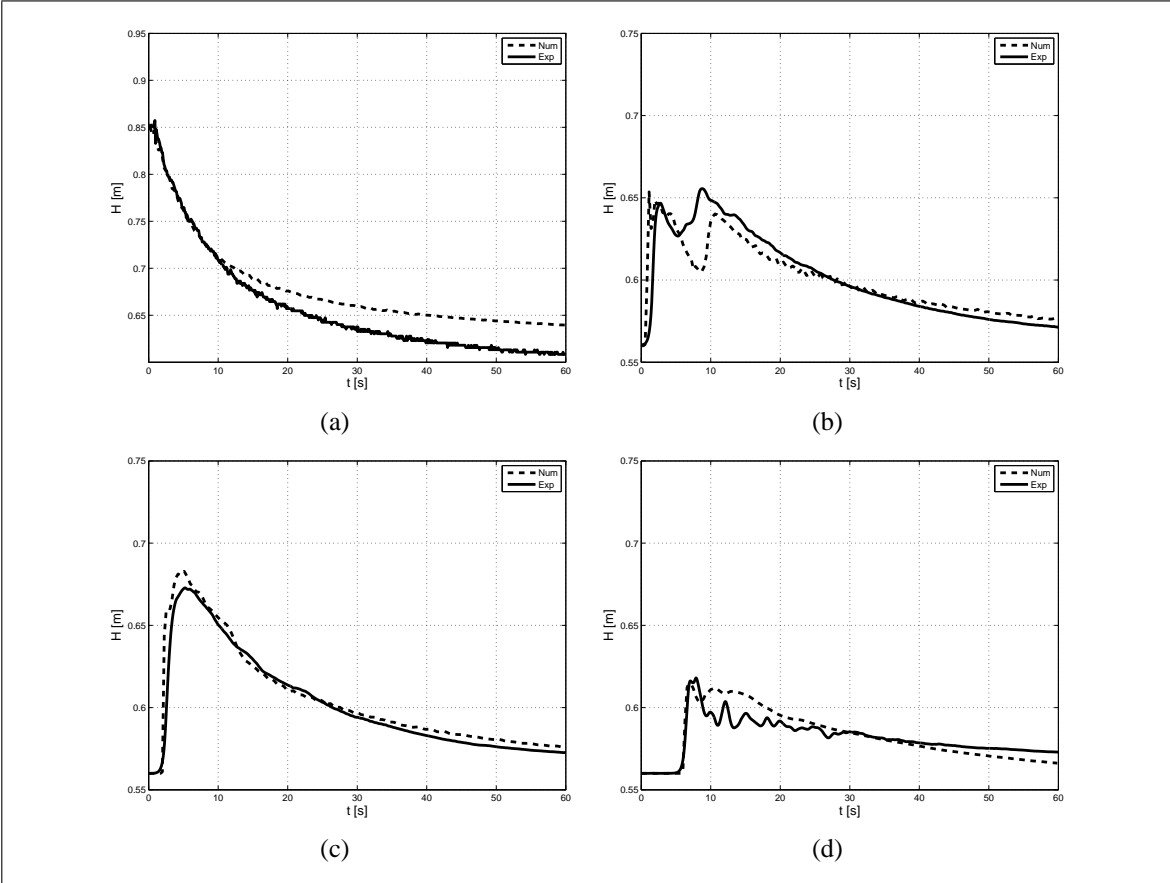


FIGURE 3.7. Comparison between measured and predicted free surface elevation at different locations: (a) Reservoir, (b) Point 23, (c) Point 20, (d) Point 12

time of their arrival. Relative errors up to 6% are found, which is an acceptable error considering how demanding the experience is. After the peaks occur, the amplitude of the wave front decays, then the model correctly predicts the recession curve at every gauge, reaching the final 0.57 free surface elevation level at almost every point.

Finally, the volume per unit area that passed under each gauge was calculated, it was compared with experimental values and excellent agreement if found, with relative errors ranging from 0.6% to 3.5%.

3.5. Conclusions

High resolution experimental data was obtained for the free surface variations in a physical model of a river, associated with the propagation of a flooding wave. This data

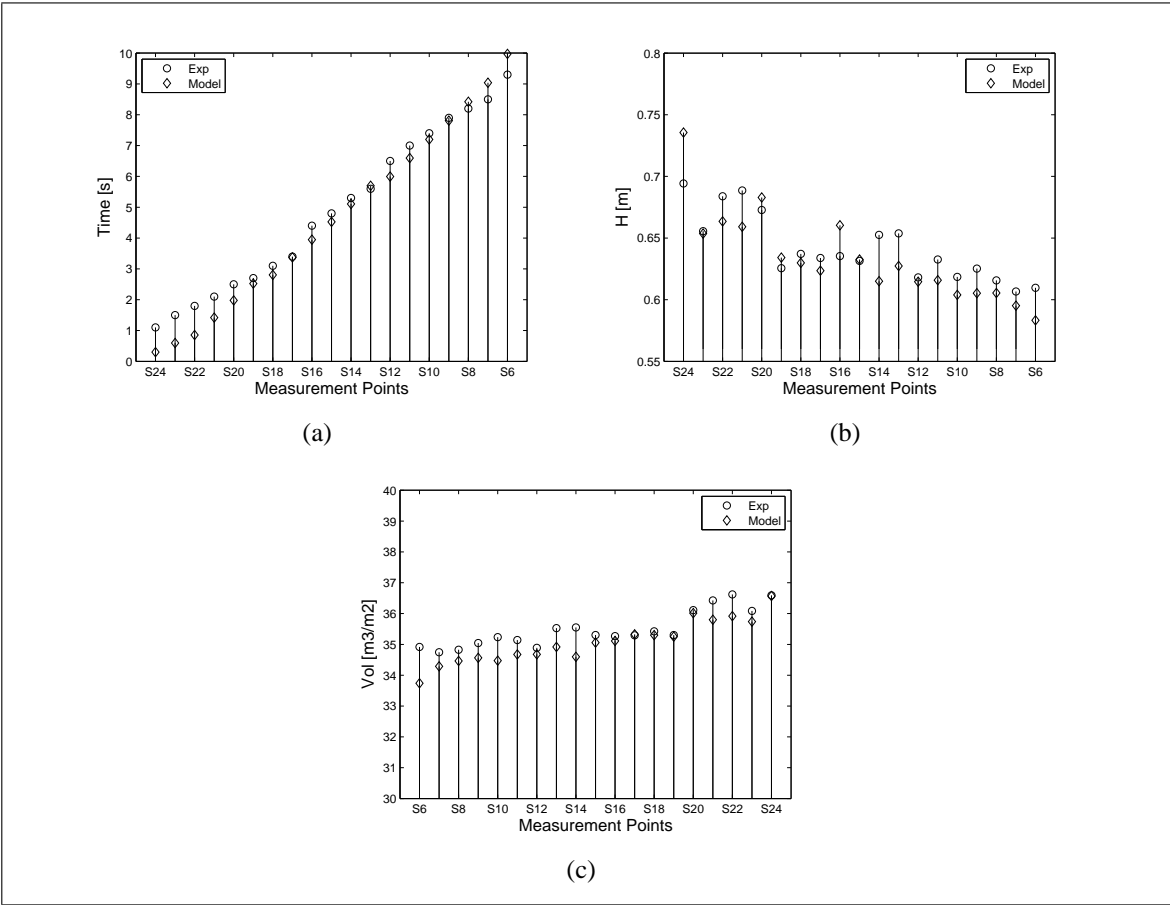


FIGURE 3.8. Comparison between measured and predicted results: (a) Arrival Time, (b) Maximum free surface elevation, (c) Volume of water per unit area

is of great interest to test numerical models and to evaluate if they are appropriate for representing this kind of phenomena over natural conditions. Also, it helps to illustrate, in a simplified manner, the effects of extreme events, such as GLOF or Dam-breaks, and their consequences on surrounding areas.

The numerical model was able to represent the propagation of the wave front and the flooding processes under the tough circumstances of the experience. Arrival times, peak amplitudes and recession curves are well represented. Small differences found between experimental and numerical results may be explained by different factors. One of them is the opening mechanism of the gate, which was manually lifted in the experiments, but instantly disappears in the numerical simulations. This can generate extra oscillations in the reservoir and a delay in its emptying. Another factor can be an inadequate representation

of some sections of river due to the gridding method used, especially at the curved zone of the river after the reservoir, where a boundary-fitted grid could be more appropriate.

The numerical model is a robust and useful tool to deduce the behaviour of natural flows and the singularities that may appear. The obtained results, experimental and numerical, show the magnitude of the effects that an extreme event similar to the simulated could produce in real life. Considering the data obtained, the free surface elevation could rise 35% in just a few seconds. The latter illustrates the need of previously define risk zones, evacuation programs, and restoration guides of the affected lands and structures.

3.6. Acknowledgements

The authors thanks the *Instituto Nacional de Hidráulica* for the measurement instruments and technical support in the laboratory campaigns. Also, acknowledge Doménico Sciolla, Master student of the Hydraulic Engineering department, for the aid provided carrying out the experiences.

4. CONCLUSION AND FUTURE PERSPECTIVES

In the previous thesis, the development, implementation, validation and application of the **SURFWB_UC** numerical model were presented. The model is a low cost tool intended to study free-surface variations in time of shallow inertial flows over strongly varying topography with complex boundaries. It solves the NSWE equations written in a non-orthogonal curvilinear coordinate system using a well-balance, shock-capturing finite volume method based in the **SURF_WB** model presented in (Marche et al., 2007) and in the friction method proposed in (Q. Liang & Marche, 2009).

In order to probe its capabilities, the numerical model was submitted to several validation test and new experimental data associated with the propagation of a flash flood wave. The test cases studied involved convergence to steady state at rest, 1D and 2D dam-break, frictional topographies, moving shore-line processes, subcritical and supercritical flow, among others features, all of them proper of shallow-inertial flows. Good agreement was found between numerical results and analytical solutions, and also between the laboratory data. The presented numerical model was stable and accurate in all of those applications, thus confirming the capabilities of the model.

During the performed simulations, the main drawback that was encountered was the gridding process for extremely complicated geometries such as the physical river model. This can be a demanding task in the case of natural topography if the needed information is not enough. To address this issue, information can be obtained from field surveys or digital elevation models (DEM). Also, to create boundary-fitted grids, a good gridding software or interpolation method has to be available.

The numerical model was developed to satisfy the need of predicting the effects of flash extreme flooding over complex topographies resulting form storm surges, dam-breaks, tsunamis or GLOF. The obtained results and the demonstrated capabilities of the model shown in both articles allow us to affirm that it is a powerful tool to study the consequences of this kind of phenomena, leading to a better understanding and analysis of the development and behavior of the flow.

SURFWB_UC may be used to determine the hazards of flash extreme floods in terms of local water depth and velocities, variables that are useful to define risk zones and potential damage in the surrounding areas of a river basin or in the coast-line. For example, the effects of a river flood can be studied by simulating different discharge hydrographs based in historical data or in hydrological simulation results; the consequences of a tsunami in coastal areas can be simulated in detail by introducing long waves of different amplitude or period and direction to the computational domain. The information that the model delivers can further be used for urban planning and to define flood protection and management plans.

Future work should be oriented to complement the model with other source terms, such as the Coriolis effect in order to simulate large scale scenarios. Also, the model can be improved by coupling it with other numerical models, such as pollutant transport to analyse plumes trajectory, sediment transport to study erosion and sedimentation processes, infiltration model to account for the soil characteristics. The model could also be complemented by the integration of GIS. Finally, a friendly graphical user interface could be implemented to easily use **SURFWB_UC**.

Finally, due to the good obtained results and the wide range of application that the model can have, it can be concluded that the development of this thesis constitutes an advance in the modeling of rapidly varying flow and provides an excellent tool to study shallow inertial flows.

REFERENCES

- (n.d.).
- Alcrudo, F., & García-Navarro, P. (1993). A high resolution Godunov-type scheme in finite volumes for the 2d shallow-water equations. *International Journal of Numerical Methods in Fluids*, 16, 489-505.
- Aliabadi, S., Johnson, A., Zellars, B., Abatan, A., & Berger, C. (2002). Parallel simulation of flows in open channels. *Future Generation Computer Systems*, 18, 627-637.
- Audusse, E., Bouchut, F., Bristeau, M., Klein, R., & Benoit, P. (2004). A Fast and Stable Well-Balance Scheme with Hysdrostatic Reconstruction for Shallow Water Flows. *SIAM Journal on Scientific Computing*, 25(6), 2050-2065.
- Baghlan, A., Talebbeydokhti, N., & M.J., A. (2008). A shock-capturing model based on flux-vector splitting method in boundary-fitted curvilinear coordinates. *Applied Mathematical Modeling*, 32, 249-266.
- BBC. (2010). Flooding traps 30.000 in chinese town.
<http://www.bbc.co.uk/news/world-asia-pacific-10784666>.
- Berger, R., & Stockstill, R. (1995). Finite-element model for high-velocity channels. *Journal of Hydraulic Engineering*, 121, 225-252.
- Bradford, S., & Sanders, B. (2002). Finite-volume model for shallow-water flooding of arbitrary topography. *Journal of Hydraulic Engineering*, 128, 289-298.
- Buffard, T., Gallouet, T., & Herard, J.-M. (2000). A sequel to a rough Godunov scheme: application to real gases. *Computers and Fluids*, 29, 813-847.
- Cao, Z., Pender, G., Wallis, S., & Carling, P. (2004). Computational dam-break hydraulics over erodible sediment bed. *Journal of Hydraulic Engineering*, 130, 689-703.
- Causon, D., & Mingham, C. (1999). Advances in calculation methods for supercritical flow in spillway channels. *Journal of Hydraulic Engineering*, 125, 1039-1050.
- Chow, V.-T. (1959). *Open-channel hydraulics*. New York McGraw-Hill.

- Cienfuegos, R., Barthelemy, E., & Bonneton, P. (2007). A fourth order compact finite volume scheme for fully nonlinear and weakly dispersive Boussinesq-type equations - Part II : Boundary Conditions and validation. *Int. J. Num. Meth. Fluids*, 53, 1423-1455.
- Courant, R., Friedrichs, K., & Lewy, H. (1928). Über die partieller Differenzen-Gleichungen der mathematischen Physik. *Mathematische Annalar*, 100, 32-74.
- Cunge, J. (1991). *Simulation des Encoulements dans les Rivieres et Canaux*. Institut National Polytechnique de Grenoble.
- Cunge, J., F., H., & A., V. (1980). *Practical Aspects of Computational River Hydraulics*. Pitman Publishing Limited.
- Dussaillant, A., Benito, G., Buytaert, W., Carling, P., Meier, C., & Espinoza, F. (2009). Repeated glacial-lake outburst floods in Patagonia: an increasing hazard? *Natural Hazards*, 54, 469-481.
- Farias, M., Vargas, G., Tassara, A., Carretier, S., Baize, S., Melnick, D., et al. (2010). Land-level changes produced by the Mw 8.8 2010 chilean earthquake. *Science*, 329, 916.
- Ferziger, J., & Peric, M. (1996). *Computational Methods for Fluid Dynamics*. Springer.
- Fujihara, M., & Borthwick, A. (2000). Godunov-type solution of curvilinear shallow-water equations. *Journal of Hydraulic Engineering*, 126, 827-836.
- Gallouet, T., Herard, J.-M., & Seguin, N. (2003a). On the use of symmetrizing variables for vacuums. *Calcolo*, 40, 163-194.
- Gallouet, T., Herard, J.-M., & Seguin, N. (2003b). Some approximate Godunov scheme to compute shallow-water equations with topography. *Computers and Fluids*, 32, 479-513.
- Greenberg, J., & Leroux, A. (1996). A well-balanced scheme for the numerical processing of source terms in hyperbolic equations. *SIAM Journal on Numerical Analysis*, 33(1), 1–16.

- Hervouet, J. (2000). A high resolution 2-d dam-break model using parallelization. *Hydrological Processes*, 14, 2211-2230.
- Hogg, A., & Pritchard, D. (2004). The effects of hydraulic resistance on dam-break and other shallow inertial flows. *Journal of Fluids Mechanics*, 501, 179-212.
- Ippen, A., & Dawson, J. (1951). Desing of channel constrictions: High velocity flow in open channels (symposium). *Transactions of ASCE*, 116, 326-346.
- Kruger, S., & Rutschmann, P. (2006). Modeling 3d supercritical flow with extended shallow-water approach. *Journal of Hydraulic Engineering*, 127, 916-926.
- Lackey, T., & Sotiropoulos, F. (2005). Role of artificial dissipation scaling and multi-grid acceleration in numerical solution of the depth-averaged free-surface flow equations. *Journal of Hydraulic Engineering*, 131, 476-487.
- LeVeque, R. (1998). Balancing source terms and flux gradients in high-resolution godunov methods: the quasi-steady wave-propagation algorithm. *Journal of Computational Physics*, 146(1), 346–365.
- Leveque, R. (2002). *Finite Volumen Methods for Hyperbolic Problems*. Cambridge University Press.
- Liang, D., Lin, B., & Falconer, R. (2007). A boundary-fitted numerical model for flood routing with shock-capturing capability. *Journal of Hydrology*, 332, 477-486.
- Liang, Q., & Marche, F. (2009). Numerical resolution of well-balanced shallow water equations with complex source terms. *Advances in Water Resources*, 32, 873-884.
- Loose, B., Niño, Y., & Escauriaza, C. (2005). Finite volume modeling of variable density shallow-water flow equations for a well-mixed estuary: application to the rio Maipo estuary in central Chile. *Journal of Hydraulic Research*, 43, 339-350.
- Marche, F. (2005). *Theoretical and Numerical Study of Shallow Water Models. Applications to Nearshore Hydrodynamics*. Unpublished doctoral dissertation, LUniversit Bordeaux I.
- Marche, F. (2007). Derivation of a new two-dimensional viscous shallow water model with varying topography, bottom friction and capillary effects. *European Journal of Mechanics B/Fluids*, 26, 49-63.

- Marche, F., Bonneton, P., Fabrie, P., & Seguin, N. (2007). Evaluation of well-balance bore-capturing schemes for 2D wetting and drying processes. *International Journal for Numerical Methods in Fluids*, 53, 867-894.
- Masella, J., Faille, I., & Gallouet, T. (1999). A rough Godunov scheme. *International Journal of Computational Fluid Dynamics*, 12, 133-149.
- Mignot, E., & Cienfuegos, R. (2009). On the application of a Boussinesq model to river flows including shocks. *Coastal Engineering*, 56, 23-31.
- Mingham, C., & Causon, D. (1998). High-resolution finite-volume method for shallow water flows. *Journal of Hydraulic Engineering*, 124, 604-614.
- Molls, T., & Chaudry, D. (1995). Depth-averaged open-channel flow model. *Journal of Hydraulic Engineering*, 121, 453-465.
- Molls, T., & Zhao, G. (2000). Depth-averaged simulation of supercritical flow in channel with wavy sidewall. *Journal of Hydraulic Engineering*, 126, 437-444.
- Sampson, J., Easton, A., & Singh, M. (2006). Moving boundary shallow water flow above parabolic bottom topography. *ANZIAM Journal*, 47, C373-C387.
- Shi, F., Dalrymple, R., Kirby, J., Chen, Q., & Kennedy, A. (2001). A fully nonlinear Boussinesq model in generalized curvilinear coordinates. *Coastal Engineering*, 42, 337-358.
- Stoker, J. (1992). *Water Waves, The Mathematical Theory with Applications*. John Wiley and Sons, Inc.
- Synolakis, C., & Kong, L. (2006). Runup measurements of the december 2004 Indian ocean tsunami. *Earthquake Spectra*, S67-S91.
- Thacker, W. (1981). Some exact solutions to the nonlinear shallow-water wave equations. *Journal of Fluids Mechanics*, 107, 499-508.
- Toro, E. (1997). *Riemann Solvers and Numerical Methods for Fluid Dynamics*. Springer.
- Toro, E. (2001). *Shock-Capturing Methods for Free-Surface Shallow Flows*. John Wiley and Sons, Inc.

- TranNgoc, A., & Takashi, H. (2007). Depth-Averaged model of open-channel flows over an arbitrary 3d surface and its applications to analysis of water surface profile. *Journal oh Hydraulic Engineering*, 133, 350-360.
- Tucciarelli, T., & Termini, D. (2000). Finite-element modeling of floodplain flow. *Journal of Hydraulic Engineering*, 126, 416-424.
- USGS. (2007). *Earthquake lists & maps*. <http://earthquake.usgs.gov/earthquakes>.
- USGS. (2010). *Magnitude 8.8 offshore Maule, Chile*. <http://earthquake.usgs.gov/earthquakes/eqinthenews/2010/us2010tfan/>.
- Valiani, A., Caleffi, V., & Zanni, A. (2002). Case study: Malpasset dam-break simulation using a two-dimensional finite volume method. *Journal of Hydraulic Engineering*, 128, 460-472.
- Van-Leer, B. (1979). Toward the ultimate conservative difference scheme V. A second order sequel to Godunov's method. *Journal of Computational Physics*, 32, 101-136.
- Vasquez, J., Steffler, P., & Millar, R. (2008). Modeling bed changes in meandering rivers using triangular finite elements. *Journal of Hydraulic Engineering*, 134, 1348-1352.
- Zhou, J., Causon, D., Mingham, C., & Ingram, D. (2004). Numerical prediction of dam-break flows in general geometries with complex topography. *Journal of Hydraulic Engineering*, 130, 332-340.

APPENDIX A. SHALLOW WATER EQUATIONS

A.1. Non-linear Shallow Equations

(i) Continuity Equation:

The two-dimensional mass conservation equation, written in terms of water depth h and Cartesian velocities, u and v , is defined as:

$$\frac{\partial h}{\partial t} + \frac{\partial hu}{\partial x} + \frac{\partial hv}{\partial y} = 0 \quad (\text{A.1})$$

(ii) Momentum Conservation Equations:

In the x direction:

$$\frac{\partial hu}{\partial t} + \frac{\partial}{\partial x}(hu^2 + \frac{1}{2}gh^2) + \frac{\partial}{\partial y}(huv) = -gh\frac{\partial z}{\partial x} - S_{fx} \quad (\text{A.2})$$

In the y direction:

$$\frac{\partial hv}{\partial t} + \frac{\partial}{\partial y}(hv^2 + \frac{1}{2}gh^2) + \frac{\partial}{\partial x}(huv) = -gh\frac{\partial z}{\partial y} - S_{fy} \quad (\text{A.3})$$

Where S_f corresponds to the friction source term, which can be calculated using Manning or Chezy approaches.

The NSWE can be written in matrix form as:

$$Q_t + F(Q)_x + G(Q)_y = S(Q) \quad (\text{A.4})$$

Where X_t o X_x denote the partial derivatives of X with respect to time t or position x . In this case:

$$Q = \begin{pmatrix} h \\ hu \\ hv \end{pmatrix}, F(Q) = \begin{pmatrix} hu \\ hu^2 + \frac{1}{2}gh^2 \\ huv \end{pmatrix}, G(Q) = \begin{pmatrix} hv \\ huv \\ hv^2 + \frac{1}{2}gh^2 \end{pmatrix}, \quad (\text{A.5})$$

$$S(Q) = \begin{pmatrix} 0 \\ -\frac{hg\partial z}{\partial x} - S_{fx} \\ -\frac{hg\partial z}{\partial y} - S_{fy} \end{pmatrix}$$

A.2. Dimensionless NSWE

A.2.1. Dimensional Scales

The characteristic scales used to obtain dimensionless variables are:

Horizontal: L

Vertical: H

Velocity: U

Froude Number: $Fr = \frac{U}{\sqrt{gH}}$

From the Froude number, the gravity acceleration can be written as $g = \frac{U^2}{Fr^2 H}$

Then the variables are transformed into:

$$x \rightarrow L\hat{x}$$

$$y \rightarrow L\hat{y}$$

$$z \rightarrow H\hat{z}$$

$$h \rightarrow H\hat{h}$$

$$u \rightarrow U\hat{u}$$

$$v \rightarrow U\hat{v}$$

$$t \rightarrow \frac{L}{U}\hat{t}$$

Where $\hat{\alpha}$ correspond to the dimensionless variables, which will be used from now on, for simplicity the $\hat{\cdot}$ symbol will be omitted.

A.2.2. Dimensionless Equations

The NSWE written in terms of dimensionless variables and characteristic scales are:

(i) Continuity Equation:

$$\frac{UH}{L} \frac{\partial h}{\partial t} + \frac{UH}{L} \frac{\partial hu}{\partial x} + \frac{UH}{L} \frac{\partial hv}{\partial y} = 0 \quad (\text{A.6})$$

Simplifying

$$\frac{\partial h}{\partial t} + \frac{\partial hu}{\partial x} + \frac{\partial hv}{\partial y} = 0 \quad (\text{A.7})$$

(ii) Momentum Equations:

In the x direction:

$$\begin{aligned} \frac{HU^2}{L} \frac{\partial hu}{\partial t} + \frac{HU^2}{L} \frac{\partial}{\partial x}(hu^2) + \frac{HU^2}{L} \frac{1}{2Fr^2} \frac{\partial h^2}{\partial x} + \frac{HU^2}{L} \frac{\partial}{\partial y}(huv) \\ = -\frac{HU^2}{L} \frac{h}{Fr^2} \frac{\partial z}{\partial x} - \tau_1 \end{aligned} \quad (\text{A.8})$$

Simplifying,

$$\begin{aligned} \frac{\partial hu}{\partial t} + \frac{\partial}{\partial x}(hu^2 + \frac{1}{2Fr^2} h^2) + \frac{\partial}{\partial y}(huv) \\ = -\frac{h}{Fr^2} \frac{\partial z}{\partial x} - \tau_1 \end{aligned} \quad (\text{A.9})$$

In the y direction:

$$\begin{aligned} \frac{HU^2}{L} \frac{\partial hu}{\partial t} + \frac{HU^2}{L} \frac{\partial}{\partial y}(hu^2) + \frac{HU^2}{L} \frac{1}{2Fr^2} \frac{\partial h^2}{\partial y} + \frac{HU^2}{L} \frac{\partial}{\partial x}(huv) \\ = -\frac{HU^2}{L} \frac{h}{Fr^2} \frac{\partial z}{\partial y} - \tau_2 \end{aligned} \quad (\text{A.10})$$

Simplifying,

$$\begin{aligned} \frac{\partial hu}{\partial t} + \frac{\partial}{\partial y}(hu^2 + \frac{1}{2Fr^2} h^2) + \frac{\partial}{\partial x}(huv) \\ = -\frac{h}{Fr^2} \frac{\partial z}{\partial y} - \tau_2 \end{aligned} \quad (\text{A.11})$$

$\tau_j, j = 1, 2$, represents the dimensionless friction shear stress.

(iii) Matrix Form of the dimensionless NSWE:

$$Q_t + F(Q)_x + G(Q)_y = S(Q) \quad (\text{A.12})$$

Each vector is rewritten as:

$$Q = \begin{pmatrix} h \\ hu \\ hv \end{pmatrix}, F(Q) = \begin{pmatrix} hu \\ hu^2 + \frac{1}{2Fr^2}h^2 \\ huv \end{pmatrix}, G(Q) = \begin{pmatrix} hv \\ huv \\ hv^2 + \frac{1}{2Fr^2}h^2 \end{pmatrix}, \quad (\text{A.13})$$

$$S(Q) = \begin{pmatrix} 0 \\ -\frac{h}{Fr^2} \frac{\partial z}{\partial x} - S_{fx} \\ -\frac{h}{Fr^2} \frac{\partial z}{\partial y} - S_{fy} \end{pmatrix}$$

APPENDIX B. CURVILINEAR SHALLOW WATER EQUATIONS

B.1. Generalized Curvilinear Coordinate System

In this section, a generalized, boundary-fitted, curvilinear coordinate system is introduced. The change of coordinates is done from the Cartesian system (x, y) to the curvilinear system (ξ, η) .

B.1.1. Some Properties of the (ξ, η) system

Some properties of the coordinate system change which will be used in the transformation process are:

(i) Jacobian of the geometric transformation $(x, y) \rightarrow (\xi, \eta)$:

$$J = \frac{\partial(\xi, \eta)}{\partial(x, y)} = \det \begin{bmatrix} \xi_x & \eta_x \\ \xi_y & \eta_y \end{bmatrix} = \xi_x \eta_y - \xi_y \eta_x \quad (\text{B.1})$$

(ii) Jacobian of the inverse transformation $(\xi, \eta) \rightarrow (x, y)$:

$$G = J^{-1} = \frac{\partial(x, y)}{\partial(\xi, \eta)} = \det \begin{bmatrix} x_\xi & y_\xi \\ x_\eta & y_\eta \end{bmatrix} = x_\xi y_\eta - x_\eta y_\xi \quad (\text{B.2})$$

(iii) Jacobian relationships or *metrics*:

(a) Relations between Cartesian coordinates:

$$\frac{\partial x}{\partial x} = 1, \frac{\partial x}{\partial y} = 0, \frac{\partial y}{\partial x} = 0, \frac{\partial y}{\partial y} = 1 \quad (\text{B.3})$$

(b) Coordinate Transformation using the chain rule:

$$\begin{bmatrix} x_x \\ y_x \end{bmatrix} = \begin{bmatrix} x_\xi & x_\eta \\ y_\xi & y_\eta \end{bmatrix} \begin{bmatrix} \xi_x \\ \eta_x \end{bmatrix} = \begin{bmatrix} 1 \\ 0 \end{bmatrix} \quad (\text{B.4})$$

and

$$\begin{bmatrix} x_y \\ y_y \end{bmatrix} = \begin{bmatrix} x_\xi & x_\eta \\ y_\xi & y_\eta \end{bmatrix} \begin{bmatrix} \xi_y \\ \eta_y \end{bmatrix} = \begin{bmatrix} 0 \\ 1 \end{bmatrix} \quad (\text{B.5})$$

(c) Relations between booth coordinate systems: The solution of the (B.4) and (B.5) systems establishes the following relations:

$$\begin{aligned}\xi_x &= \frac{y_\eta}{G} = J y_\eta \\ \xi_y &= -\frac{x_\eta}{G} = -J x_\eta \\ \eta_x &= -\frac{y_\xi}{G} = -J y_\xi \\ \eta_y &= \frac{x_\xi}{G} = J x_\xi\end{aligned}\tag{B.6}$$

(d) Conservation Relations: The metrics satisfy the following conservation relations:

$$\frac{\partial}{\partial \xi} \left(\frac{\xi_x}{J} \right) + \frac{\partial}{\partial \eta} \left(\frac{\eta_x}{J} \right) = 0\tag{B.7}$$

$$\frac{\partial}{\partial \xi} \left(\frac{\xi_y}{J} \right) + \frac{\partial}{\partial \eta} \left(\frac{\eta_y}{J} \right) = 0\tag{B.8}$$

(iv) Metrics Calculations: In a discretized domain, the derivatives of the Cartesian coordinates with respect to the curvilinear coordinates can be calculated as,

$$\begin{aligned}x_\xi &= \frac{x_{i+1,j} - x_{i-1,j}}{2\Delta\xi} \\ x_\eta &= \frac{x_{i,j+1} - x_{i,j-1}}{2\Delta\eta} \\ y_\xi &= \frac{y_{i+1,j} - y_{i-1,j}}{2\Delta\xi} \\ y_\eta &= \frac{y_{i,j+1} - y_{i,j-1}}{2\Delta\eta}\end{aligned}\tag{B.9}$$

B.1.2. Covariant and Contravariant Components of a Cartesian vector

Considering a set of curvilinear coordinates which consist in two lines families: $(\xi(x, y) = cte \text{ y } \eta(x, y) = cte)$. At a point P, two vector basis are defined (see Fig. B.1). The first base consists in two vectors that are tangent to the coordinate lines, call *covariant* base.

$$g_1 = \left(\frac{\partial x}{\partial \xi}, \frac{\partial y}{\partial \xi} \right), \quad g_2 = \left(\frac{\partial x}{\partial \eta}, \frac{\partial y}{\partial \eta} \right)\tag{B.10}$$

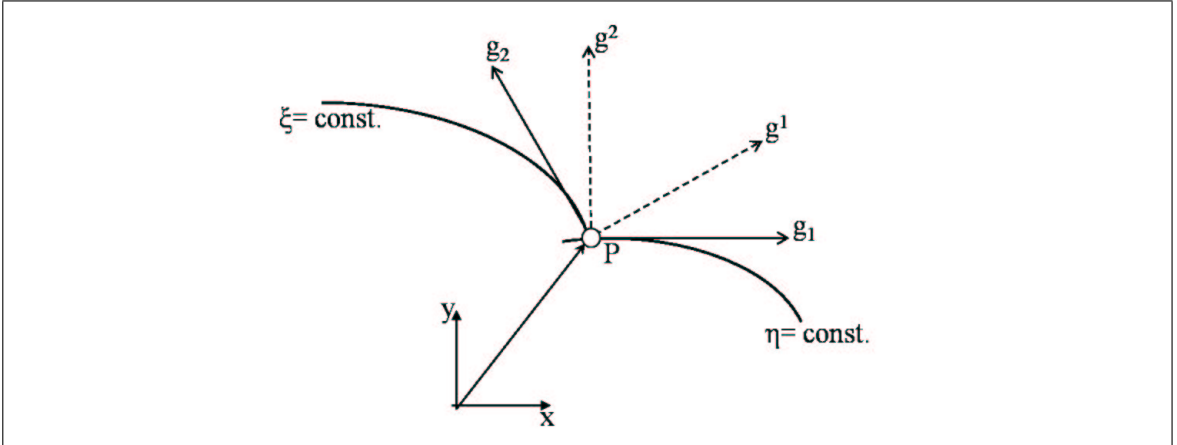


FIGURE B.1. Covariant and Contravariant Basis

The second one, consist in two vectors that are perpendicular to the ξ and η lines, and is known as *contravariant* base.

$$g^1 = \left(\frac{\partial \xi}{\partial x}, \frac{\partial \xi}{\partial y} \right), \quad g^2 = \left(\frac{\partial \eta}{\partial x}, \frac{\partial \eta}{\partial y} \right) \quad (\text{B.11})$$

A cartesian vector, $V = (u, v)$ can be expressed in terms of the *covariant* abse as:

$$V = V^1 g_1 + V^2 g_2 \quad (\text{B.12})$$

Where,

$$V^1 = V \bullet g^1 = u \frac{\partial \xi}{\partial x} + v \frac{\partial \xi}{\partial y} \quad (\text{B.13})$$

$$V^2 = V \bullet g^2 = u \frac{\partial \eta}{\partial x} + v \frac{\partial \eta}{\partial y} \quad (\text{B.14})$$

The latter components of the vector, V^1 y V^2 , are called *contravariant* components. Similarly, a *covariant* set can be defined as:

$$V = V_1 g^1 + V_2 g^2 \quad (\text{B.15})$$

Where,

$$V_1 = V \bullet g_1 = u \frac{\partial x}{\partial \xi} + v \frac{\partial y}{\partial \xi} \quad (\text{B.16})$$

$$V_2 = V \bullet g_2 = u \frac{\partial x}{\partial \eta} + v \frac{\partial y}{\partial \eta} \quad (\text{B.17})$$

B.2. Curvilinear NSWE

The complete details of the change of coordinate of the dimensionless NSWE (A.12) is described below.

(i) Continuity Equation:

$$\frac{\partial h}{\partial t} + \frac{\partial(hu)}{\partial \xi} \frac{\partial \xi}{\partial x} + \frac{\partial(hu)}{\partial \eta} \frac{\partial \eta}{\partial x} + \frac{\partial(hv)}{\partial \xi} \frac{\partial \xi}{\partial y} + \frac{\partial(hv)}{\partial \eta} \frac{\partial \eta}{\partial y} = 0 \quad (\text{B.18})$$

The strong-conservation form of the latter equation can be obtained by multiplying and dividing the equation by the Jacobian J :

$$\frac{\partial h}{\partial t} + J \left(\frac{\partial(hu)}{\partial \xi} \frac{\partial \xi}{\partial x} \frac{1}{J} + \frac{\partial(hu)}{\partial \eta} \frac{\partial \eta}{\partial x} \frac{1}{J} + \frac{\partial(hv)}{\partial \xi} \frac{\partial \xi}{\partial y} \frac{1}{J} + \frac{\partial(hv)}{\partial \eta} \frac{\partial \eta}{\partial y} \frac{1}{J} \right) = 0 \quad (\text{B.19})$$

Using the conservative relations (B.7) and (B.8) and rearranging,

$$h_t + J \frac{\partial}{\partial \xi} \left[\frac{h(u\xi_x + v\xi_y)}{J} \right] + \frac{\partial}{\partial \eta} \left[\frac{h(u\eta_x + v\eta_y)}{J} \right] = 0 \quad (\text{B.20})$$

Defining $U^1 = u\xi_x + v\xi_y$ y $U^2 = u\eta_x + v\eta_y$ as the contravariant velocities components, the continuity equations in a curvilinear coordinate system is written as:

$$h_t + J \left(\frac{U^1 h}{J} \right)_\xi + J \left(\frac{U^2 h}{J} \right)_\eta = 0 \quad (\text{B.21})$$

(ii) Momentum Equations:

In the x direction:

$$\begin{aligned}
& (hu)_t + \frac{\partial}{\partial \xi} (hu^2 + \frac{1}{2Fr^2} h^2) \xi_x \\
& + \frac{\partial}{\partial \eta} (hu^2 + \frac{1}{2Fr^2} h^2) \eta_x + \frac{\partial}{\partial \xi} (huv) \xi_y + \frac{\partial}{\partial \eta} (huv) \eta_y \\
& = -\frac{h}{Fr^2} (z_\xi \xi_x + z_\eta \eta_x) - \tau_1
\end{aligned} \tag{B.22}$$

Multiplying and dividing by the Jacobian J ,

$$\begin{aligned}
& (hu)_t + J \frac{\partial}{\partial \xi} (hu^2 + \frac{1}{2Fr^2} h^2) \frac{\xi_x}{J} \\
& + \frac{\partial}{\partial \eta} (hu^2 + \frac{1}{2Fr^2} h^2) \frac{\eta_x}{J} + \frac{\partial}{\partial \xi} (huv) \frac{\xi_y}{J} + \frac{\partial}{\partial \eta} (huv) \frac{\eta_y}{J} \\
& = -\frac{h}{Fr^2} (z_\xi \xi_x + z_\eta \eta_x) - \tau_1
\end{aligned} \tag{B.23}$$

Using the conservative relations (B.7) and (B.8) and rearranging,

$$\begin{aligned}
& (hu)_t + \frac{\partial}{\partial \xi} (hu(u\xi_x + v\xi_y) \frac{1}{J} + \frac{1}{2Fr^2} h^2 \xi_x \frac{1}{J}) \\
& + \frac{\partial}{\partial \eta} (hu(u\eta_x + v\eta_y) \frac{1}{J} + \frac{1}{2Fr^2} h^2 \eta_x \frac{1}{J}) \\
& = -\frac{h}{Fr^2} (z_\xi \xi_x + z_\eta \eta_x) - \tau_1
\end{aligned} \tag{B.24}$$

Finally,

$$(hu)_t + \left(\frac{huU^1 + \frac{1}{2Fr^2} h^2 \xi_x}{J} \right)_\xi + \left(\frac{huU^2 + \frac{1}{2Fr^2} h^2 \eta_x}{J} \right)_\eta = -\frac{h}{Fr^2} (z_\xi \xi_x + z_\eta \eta_x) - \tau_1 \tag{B.25}$$

Analogously in the y direction:

$$(hv)_t + \left(\frac{hvU^1 + \frac{1}{2Fr^2} h^2 \xi_x}{J} \right)_\xi + \left(\frac{hvU^2 + \frac{1}{2Fr^2} h^2 \eta_y}{J} \right)_\eta = -\frac{h}{Fr^2} (z_\xi \xi_y + z_\eta \eta_y) - \tau_2 \tag{B.26}$$

(iii) Matrix Form:

The NSWE in curvilinear coordinates, written in a conservative form, are:

$$Q_t + JF_\xi + JG_\eta = S \quad (\text{B.27})$$

Where:

$$Q = \begin{pmatrix} h \\ hu \\ hv \end{pmatrix}, F = \frac{1}{J} \begin{pmatrix} hU^1 \\ uhU^1 + \frac{1}{2Fr^2}h^2\xi_x \\ vhU^1 + \frac{1}{2Fr^2}h^2\xi_y \end{pmatrix}, G = \frac{1}{J} \begin{pmatrix} hU^2 \\ uhU^2 + \frac{1}{2Fr^2}h^2\eta_x \\ vhU^2 + \frac{1}{2Fr^2}h^2\eta_y \end{pmatrix} \quad (\text{B.28})$$

$$S = \begin{pmatrix} 0 \\ -\frac{h}{Fr^2}(z_\xi\xi_x + z_\eta\eta_x) - S_{fx} \\ -\frac{h}{Fr^2}(z_\xi\xi_y + z_\eta\eta_y) - S_{fx} \end{pmatrix}$$

APPENDIX C. NON-CONSERVATIVE FORM OF THE CURVILINEAR NSWE

C.1. Non-Conservative form of the curvilinear NSWE

The system (B.27) is a hyperbolic system of partial differential equations and it can be written in a non-conservative form as:

$$Q_t + A(Q)Q_\xi + B(Q)Q_\eta \quad (\text{C.1})$$

Where A and B correspond to the Jacobian matrices of the system, which are diagonalizable and have real eigenvalues λ_i . A linear combination of the corresponding eigenvectors, constitute a solution to the hyperbolic problem, which consist in a linear combination of m "waves" travelling at the characteristic speed λ_i .

In this section, the procedure to find the eigenvalues, or characteristic directions, is explained. These values will be used in the numerical solution of the curvilinear SWE.

(i) Continuity Equation:

Expanding the derivatives of the Eq. B.20:

$$\begin{aligned} h_t + J \left[(hu)_\xi \frac{\xi_x}{J} + (hu)\left(\frac{\xi_x}{J}\right)_\xi + (hv)_\xi \frac{\xi_y}{J} + (hu)\left(\frac{\xi_y}{J}\right)_\xi \right] \\ + J \left[(hu)_\eta \frac{\eta_x}{J} + (hu)\left(\frac{\eta_x}{J}\right)_\eta + (hv)_\eta \frac{\eta_y}{J} + (hu)\left(\frac{\eta_y}{J}\right)_\eta \right] = 0 \end{aligned} \quad (\text{C.2})$$

Then, using relations (B.7) and (B.8) and rearraging,

$$\begin{aligned} h_t + \xi_x \frac{\partial(hu)}{\partial\xi} + \xi_y \frac{\partial(hv)}{\partial\xi} + hu \frac{\partial\xi_x}{\partial\xi} + hv \frac{\partial\xi_y}{\partial\xi} \\ + \eta_x \frac{\partial(hu)}{\partial\eta} + \eta_y \frac{\partial(hv)}{\partial\eta} + hu \frac{\partial\eta_x}{\partial\eta} + hv \frac{\partial\eta_y}{\partial\eta} = 0 \end{aligned} \quad (\text{C.3})$$

but $\frac{\partial \xi_x}{\partial \xi} = \frac{\partial^2 \xi}{\partial x \partial \xi} = \frac{\partial}{\partial x} \frac{\partial \xi}{\partial \xi} = 0$ (the same for η), then the mass conservation equations in its non-conservative form is defined as:

$$h_t + \xi_x(hu)_\xi + \xi_y(hv)_\xi + \eta_x(hu)_\eta + \eta_y(hv)_\eta = 0 \quad (\text{C.4})$$

(ii) Momentum Equations:

In the x direction, starting from Eq. (B.22):

$$\begin{aligned} (hu)_t + hu \frac{\partial}{\partial \xi} U^1 + U^1 \frac{\partial(hu)}{\partial \xi} + \frac{1}{2Fr^2} 2h\xi_x \frac{\partial h}{\partial \xi} + \frac{1}{2Fr^2} h^2 \frac{\partial \xi_x}{\partial \xi}^0 \\ + hu \frac{\partial}{\partial \eta} U^2 + U^2 \frac{\partial(hu)}{\partial \eta} + \frac{1}{2Fr^2} 2h\eta_x \frac{\partial h}{\partial \eta} + \frac{1}{2Fr^2} h^2 \frac{\partial \eta_x}{\partial \eta}^0 = S_2 \end{aligned} \quad (\text{C.5})$$

Expanding the derivatives that are not in function of h, u and v variables:

$$\begin{aligned} hu \frac{\partial U^1}{\partial \xi} &= \frac{\partial huU^1}{\partial \xi} - U^1 \frac{\partial(hu)}{\partial \xi} \\ &= u \frac{\partial hU^1}{\partial \xi} + h \cancel{U^1 \frac{\partial u}{\partial \xi}} - U^1 u \frac{\partial h}{\partial \xi} - \cancel{U^1 h \frac{\partial u}{\partial \xi}} \\ &= u \frac{\partial}{\partial \xi} (hu\xi_x + hv\xi_y) - U^1 u \frac{\partial h}{\partial \xi} \\ &= u\xi_x \frac{\partial(hu)}{\partial \xi} + u\xi_y \frac{\partial(hv)}{\partial \xi} - U^1 u \frac{\partial h}{\partial \xi} \end{aligned}$$

Analogously:

$$hu \frac{\partial U^2}{\partial \eta} = u\eta_x \frac{\partial(hu)}{\partial \eta} + u\eta_y \frac{\partial(hv)}{\partial \eta} - U^2 u \frac{\partial h}{\partial \eta}$$

Finally, the equation written in a non-conservative form is:

$$\begin{aligned} (hu)_t + \left(\frac{h}{Fr^2} \xi_x - U^1 u \right) h_\xi + (U^1 + u\xi_x)(hu)_\xi + u\xi_y(hv)_\xi + \\ \left(\frac{h}{Fr^2} \eta_x - U^2 u \right) h_\eta + (U^2 + u\eta_x)(hu)_\eta + u\eta_y(hv)_\eta = Snc_2 \end{aligned} \quad (\text{C.6})$$

Analogously, in the y direction,

$$\begin{aligned} (hv)_t + \left(\frac{h}{Fr^2} \xi_y - U^1 v \right) h_\xi + (U^1 + u\xi_x)(hv)_\xi + v\xi_y(hu)_\xi + \\ \left(\frac{h}{Fr^2} \eta_y - U^2 v \right) h_\eta + (U^2 + v\eta_x)(hv)_\eta + v\eta_x(hu)_\eta = Snc_3 \end{aligned} \quad (\text{C.7})$$

(iii) Matrix Form:

$$Q_t + A^1 Q_\xi + A^2 Q_\eta = Snc \quad (\text{C.8})$$

Where:

$$Q = \begin{pmatrix} h \\ hu \\ hv \end{pmatrix}, \quad (\text{C.9})$$

$$A^1 = \begin{pmatrix} 0 & \xi_x & \xi_y \\ \frac{h}{Fr^2} \xi_x - U^1 u & U^1 + u\xi_x & u\xi_y \\ \frac{h}{Fr^2} \xi_y - U^1 v & v\xi_x & U^1 + v\xi_y \end{pmatrix}, \quad (\text{C.10})$$

$$A^2 = \begin{pmatrix} 0 & \eta_x & \eta_y \\ \frac{h}{Fr^2} \eta_x - U^2 u & U^2 + u\eta_x & u\eta_y \\ \frac{h}{Fr^2} \eta_y - U^2 v & v\eta_x & U^2 + v\eta_y \end{pmatrix}, \quad (\text{C.11})$$

$$Snc = \begin{pmatrix} 0 \\ -\frac{1}{Fr^2} (z_\xi \xi_y + z_\eta \eta_x) - \tau_1 \\ -\frac{1}{Fr^2} (z_\xi \xi_y + z_\eta \eta_y) - \tau_2 \end{pmatrix} \quad (\text{C.12})$$

C.2. Eigenvalues of Jacobian matrices

The eigenvalues are the solution of the following system:

$$|A - \lambda I| = 0 \quad (\text{C.13})$$

Thus, the eigenvalues are:

$$\lambda_1^1 = U^1 - \sqrt{\frac{h}{Fr^2}(\xi_x^2 + \xi_y^2)}, \lambda_2^1 = U^1, \lambda_3^1 = U^1 + \sqrt{\frac{h}{Fr^2}(\xi_x^2 + \xi_y^2)} \quad (\text{C.14})$$

$$\lambda_1^2 = U^2 - \sqrt{\frac{h}{Fr^2}(\eta_x^2 + \eta_y^2)}, \lambda_2^2 = U^2, \lambda_3^2 = U^2 + \sqrt{\frac{h}{Fr^2}(\eta_x^2 + \eta_y^2)} \quad (\text{C.15})$$

Here, the dimensionless wave celerity is defined as $C = \sqrt{\frac{h}{Fr^2}}$.

APPENDIX D. THE VFROE-NCV APPROXIMATE RIEMANN SOLVER

The **VFRoe-ncv** is inspired in Godunov's and Roe's schemes. A linearized Riemann problem is solved at each cell interface, following Roe's idea. This linearized exact solution is used to calculate the numerical fluxes, following Godunov's idea. This scheme was first presented in Masella et al. (1999), and its detailed development can be found in Masella et al. (1999); Buffard et al. (2000); Marche et al. (2007).

D.1. Formalism of the VFRoe-ncv scheme

In a one-dimensional frame, the following Riemann problem is:

$$Q_t + F(Q)_x = 0 \quad (\text{D.1})$$

$$Q(x, 0) = \begin{cases} Q_L & \text{if } x < 0 \\ Q_R & \text{if } x > 0 \end{cases} \quad (\text{D.2})$$

Where $Q(x, t) \in \mathbb{R}^p$ and the $F(Q)$ flux is such that the Jacobian matrix, $A(Q) = \frac{\partial F}{\partial Q}$ is diagonalizable and has real eigenvalues.

Considering the change of variables $Q \rightarrow Y(Q)$ (Y is an invertible function), the system (D.1) is defined in a non-conservative form:

$$Y_t + B(Y)Y_x = 0 \quad (\text{D.3})$$

Following Roe's idea, at each cell interface the following linear Riemann (LRP) problem is solved:

$$Y_t + B(\tilde{Y})Y_x = 0 \quad (\text{D.4})$$

$$Y(x, 0) = \begin{cases} Y_L & \text{if } x < 0 \\ Y_R & \text{if } x > 0 \end{cases} \quad (\text{D.5})$$

Where \tilde{Y} is an averaged state that depends of Y_L and Y_R . $B(\tilde{Y})$ is a diagonalizable matrix and has real eigenvalues $\tilde{\lambda}_i$ with $i \in 1, \dots, p$ sorted from lowest to highest.

The exact solution to the LRP at each side of the discontinuity is written as:

$$Y^*((\frac{x}{t})^-, Y_L, Y_R) = Y_L + \sum_{\tilde{\lambda}_i < (\frac{x}{t})} \tilde{l}_i [Y]_L^R \tilde{r}_i \quad (\text{D.6})$$

$$Y^*((\frac{x}{t})^+, Y_L, Y_R) = Y_R - \sum_{\tilde{\lambda}_i > (\frac{x}{t})} \tilde{l}_i [Y]_L^R \tilde{r}_i \quad (\text{D.7})$$

Where \tilde{l}_i and \tilde{r}_i correspond to the left and right eigenvalues associated with $\tilde{\lambda}_i$, and $[Y]_L^R = Y_R - Y_L$.

The values, $Y^*((\frac{x}{t})^-, Y_L, Y_R)$ and $Y^*((\frac{x}{t})^+, Y_L, Y_R)$, are equal when $\frac{x}{t} \neq \tilde{\lambda}_i$. Thus, if none of the eigenvalues $\tilde{\lambda}_i$ vanishes, the solution at the interface, i.e $\frac{x}{t} = 0$, is given by:

$$Y^*(0, Y_L, Y_R) = Y^*((0)^-, Y_L, Y_R) = Y^*((0)^+, Y_L, Y_R) \quad (\text{D.8})$$

Finally, the scheme allow us to calculate the fluxes trough the interface as:

$$F^{VFRoe}(Q_L, Q_R) = F(Q_{VFRoe}(Y(Q_L, Q_R))) \quad (\text{D.9})$$

In the case when a rarefaction wave crosses the interface, VFRoe-ncv scheme can produce weak solutions with non-physical meaning. Therefore, a entropy correction should be added in order to reach the correctly physical solution. The latter occurs when $\lambda L_i < 0 < \lambda R_i$. In this special case, the interface solution is defined by an intermediate state, Y_m , following the correction proposed by Masella et al. (1999). The intermediate state is defined as:

$$Y_m = Y_L + \frac{\tilde{l}_i Y_L + \tilde{l}_i Y_R}{2} \tilde{r}_i = Y_R - \frac{\tilde{l}_i Y_L + \tilde{l}_i Y_R}{2} \tilde{r}_i \quad (\text{D.10})$$

APPENDIX E. WELL-BALANCED NUMERICAL SCHEME

In this section the well-balance scheme used to solve the hyperbolic step of the model is detailed. The hydrostatic reconstruction method presented in Audusse et al. (2004) will be explained, and it will be applied to the curvilinear NSWE.

A finite volume formulation of the system (B.27) is given by:

$$\frac{d}{dt} Q_{i,j}(t) + \frac{J_{i,j}}{\Delta\xi} (F_{i+\frac{1}{2},j}^* - F_{i-\frac{1}{2},j}^*) + \frac{J_{i,j}}{\Delta\eta} (G_{i,j+\frac{1}{2}}^* - G_{i,j-\frac{1}{2}}^*) = S_{i,j} \quad (\text{E.1})$$

Where:

$$Q_{i,j} = (h_{i,j}, h_{i,j}u_{i,j}, h_{i,j}v_{i,j})^T$$

$F_{i\pm\frac{1}{2},j}^*$, $G_{i,j\pm\frac{1}{2}}^*$ correspond to the numerical fluxes through the cell (i, j) interfaces, and $S_{i,j}$ corresponds to the centered discretization of the bed-slope source term. Usually, the fluxes $F_{i\pm\frac{1}{2},j}$ and $G_{i\pm\frac{1}{2},j}$ are calculated using a Riemann solver (VFRoe-ncv in this case), using the cell centered values of the state variables ($F_{i+\frac{1}{2}} = F(Q_{i,j}, Q_{i+1,j})$), but a centered evaluation of the bed-slope source term will not be able to preserve steady states at rest (Audusse et al. (2004)). These states are defined by:

$$h_{i,j} + z_{i,j} = Cte, \quad u_{i,j} = v_{i,j} = 0 \quad (\text{E.2})$$

Thus, Audusse et al. (2004) method consists in calculating the numerical fluxes with reconstructed values at the cell interface, then, bed-slope well-balance terms are introduced. Finally the FV scheme that will be solved is:

$$\frac{\partial Q_{i,j}(t)}{\partial t} + \frac{J_{i,j}}{\Delta\xi} (F_{i+\frac{1}{2},j}^+ - F_{i-\frac{1}{2},j}^-) + \frac{J_{i,j}}{\Delta\eta} (G_{i,j+\frac{1}{2}}^+ - G_{i,j-\frac{1}{2}}^-) = S_{c,i,j} \quad (\text{E.3})$$

Where F^\pm and G^\pm are the fluxes calculated using the reconstructed and balanced terms and the solution of the approximate Riemann solver. $S_{c,i,j}$ corresponds to the centered discretization of the bed-slope source term using, also, reconstructed values.

E.1. 1st Order Hydrostatic Reconstruction

The first step is to obtain reconstructed values at the cell interfaces, taking into account bottom variations and the obtained balance for static flows. Without loss of generality, the values at the cell interfaces $(i + \frac{1}{2}, j)$ and $(i, j + \frac{1}{2})$ will be defined. The cell discretization is shown in Fig. (E.1).

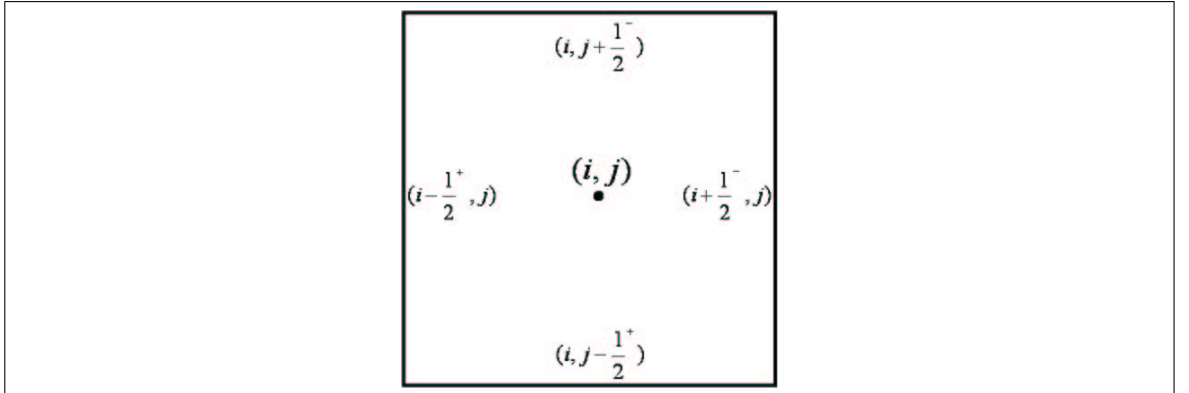


FIGURE E.1. Discretización en la celda i-ésima

Topography values at the cell interfaces are defined as:

$$z_{i\pm\frac{1}{2},j} = \max(z_{i,j}, z_{i\pm 1,j}) \quad (\text{E.4})$$

$$z_{i,j\pm\frac{1}{2}} = \max(z_{i,j}, z_{i,j\pm 1}) \quad (\text{E.5})$$

Then, the water depth reconstruction at the cell interfaces, which must be positivity preserving, is defined as:

$$h_{i+\frac{1}{2}-,j} = \max(0, h_{i,j} + z_{i,j} - z_{i+\frac{1}{2},j}) \quad (\text{E.6})$$

$$h_{i+\frac{1}{2}+,j} = \max(0, h_{i+1,j} + z_{i+1,j} - z_{i+\frac{1}{2},j}) \quad (\text{E.7})$$

$$h_{i,j+\frac{1}{2}-} = \max(0, h_{i,j} + z_{i,j} - z_{i,j+\frac{1}{2}}) \quad (\text{E.8})$$

$$h_{i,j+\frac{1}{2}+} = \max(0, h_{i,j+1} + z_{i,j+1} - z_{i,j+\frac{1}{2}}) \quad (\text{E.9})$$

and the complete reconstructed values are:

$$Q_{i+\frac{1}{2}^-, j} = \begin{pmatrix} h_{i+\frac{1}{2}^-, j} \\ h_{i+\frac{1}{2}^-, j} u_{i,j} \\ h_{i+\frac{1}{2}^-, j} v_{i,j} \end{pmatrix} \quad (\text{E.10})$$

$$Q_{i+\frac{1}{2}^+, j} = \begin{pmatrix} h_{i+\frac{1}{2}^+, j} \\ h_{i+\frac{1}{2}^+, j} u_{i+1,j} \\ h_{i+\frac{1}{2}^+, j} v_{i+1,j} \end{pmatrix} \quad (\text{E.11})$$

$$Q_{i,j+\frac{1}{2}^-} = \begin{pmatrix} h_{i,j+\frac{1}{2}^-} \\ h_{i,j+\frac{1}{2}^-} u_{i,j} \\ h_{i,j+\frac{1}{2}^-} v_{i,j} \end{pmatrix} \quad (\text{E.12})$$

$$Q_{i,j+\frac{1}{2}^+} = \begin{pmatrix} h_{i,j+\frac{1}{2}^+} \\ h_{i,j+\frac{1}{2}^+} u_{i,j+1} \\ h_{i,j+\frac{1}{2}^+} v_{i,j+1} \end{pmatrix} \quad (\text{E.13})$$

These reconstructed values, (E.10),(E.11), (E.12) and (E.13), are used as an input to solve the Riemann problem and then to calculate the numerical fluxes of the homogeneous problem, ($F_{i\pm\frac{1}{2},j}^*$ y $G_{i,j\pm\frac{1}{2}}^*$), then:

$$F_{i\pm\frac{1}{2},j}^* = F(Q_{i\pm\frac{1}{2},j}^*) = F(Q^*(0, Q_{i\pm\frac{1}{2}^-, j}, Q_{i\pm\frac{1}{2}^+, j})) \quad (\text{E.14})$$

$$G_{i,j\pm\frac{1}{2}}^* = G(Q_{i,j\pm\frac{1}{2}}^*) = G(Q^*(0, Q_{i,j\pm\frac{1}{2}^-}, Q_{i,j\pm\frac{1}{2}^+})) \quad (\text{E.15})$$

At the same time, the bed-slope source term is discretized and distributed to the cell interfaces, considering the hydrostatic balance for static flows. At steady state $h+z = Cte$, $hu = Cte$, $hv = Cte$ and $\frac{\partial}{\partial t} = 0$, at rest: $u = v = 0$. Then, from the momentum equations (B.25) and (B.26):

$$J\left(\frac{1}{2Fr^2}h^2\frac{\xi_x}{J}\right)_\xi + J\left(\frac{1}{2Fr^2}h^2\frac{\eta_x}{J}\right)_\eta = -\frac{h}{Fr^2}(\xi_x z_\xi + \eta_x z_\eta) \quad (\text{E.16})$$

$$J\left(\frac{1}{2Fr^2}h^2\frac{\xi_y}{J}\right)_\xi + J\left(\frac{1}{2Fr^2}h^2\frac{\eta_y}{J}\right)_\eta = -\frac{h}{Fr^2}(\xi_y z_\xi + \eta_y z_\eta) \quad (\text{E.17})$$

For simplicity, we will proceed only with Eq. (E.16). The source term associated with each curvilinear direction will be balanced with the corresponding flux:

$$\text{a. } J\left(\frac{1}{2Fr^2}h^2\frac{\xi_x}{J}\right)_\xi \approx -\frac{h}{Fr^2}\xi_x z_\xi$$

$$\text{b. } J\left(\frac{1}{2Fr^2}h^2\frac{\eta_x}{J}\right)_\eta \approx -\frac{h}{Fr^2}\eta_x z_\eta$$

Considering the ξ (Eq. a.) and integrating over the la i-th cell, an approximation of the averaged source term into the cell

$$\begin{aligned} & -\frac{1}{\Delta\xi} \int_{\xi_{i-\frac{1}{2}^+,j}}^{\xi_{i+\frac{1}{2}^-,j}} \frac{h}{Fr^2} \xi_x z_\xi d\xi \approx \frac{J}{\Delta\xi} \int_{\xi_{i-\frac{1}{2}^+,j}}^{\xi_{i+\frac{1}{2}^-,j}} \frac{1}{2Fr^2} \frac{\xi_x}{J} h_\xi^2 d\xi \\ &= \frac{J}{\Delta\xi} \left(\int_{\xi_{i-\frac{1}{2}^+,j}}^{\xi_{i,j}} \frac{1}{2Fr^2} \frac{\xi_x}{J} h_\xi^2 d\xi + \int_{\xi_{i,j}}^{\xi_{i+\frac{1}{2}^-,j}} \frac{1}{2Fr^2} \frac{\xi_x}{J} h_\xi^2 d\xi \right) \\ &= \frac{J}{\Delta\xi} \frac{1}{2Fr^2} \left(\left(\frac{\xi_x}{J} \right)_{i,j} h_{i,j}^2 - \left(\frac{\xi_x}{J} \right)_{i-\frac{1}{2},j} h_{i-\frac{1}{2},j}^2 + \left(\frac{\xi_x}{J} \right)_{i+\frac{1}{2},j} h_{i+\frac{1}{2},j}^2 - \left(\frac{\xi_x}{J} \right)_{i,j} h_{i,j}^2 \right) \end{aligned} \quad (\text{E.18})$$

The latter is analogous for the η direction, and motivates to discretize the bed-slope source term $Sc_{i,j}$ as:

$$Sc_{i,j} = \frac{J_{i,j}}{\Delta\xi} Sc_{i,j}^\xi + \frac{J_{i,j}}{\Delta\eta} Sc_{i,j}^\eta \quad (\text{E.19})$$

$$Sc_{i,j}^\xi = Sc_{i+\frac{1}{2}^-,j}^\xi + Sc_{i-\frac{1}{2}^+,j}^\xi \quad (\text{E.20})$$

$$Sc_{i+\frac{1}{2}^-,j}^\xi + Sc_{i-\frac{1}{2}^+,j}^\xi = \begin{pmatrix} 0 \\ Sc_{i+\frac{1}{2}^-,j}^1 \\ Sc_{i+\frac{1}{2}^-,j}^2 \end{pmatrix} + \begin{pmatrix} 0 \\ Sc_{i-\frac{1}{2}^+,j}^1 \\ Sc_{i-\frac{1}{2}^+,j}^2 \end{pmatrix} \quad (\text{E.21})$$

$$Sc_{i,j}^\eta = Sc_{i,j+\frac{1}{2}^-}^\eta + Sc_{i,j-\frac{1}{2}^+}^\eta \quad (\text{E.22})$$

$$Sc_{i,j+\frac{1}{2}^-}^\eta + Sc_{i,j-\frac{1}{2}^+}^\eta = \begin{pmatrix} 0 \\ Sc_{i,j+\frac{1}{2}^-}^1 \\ Sc_{i,j+\frac{1}{2}^-}^2 \end{pmatrix} + \begin{pmatrix} 0 \\ Sc_{i,j-\frac{1}{2}^+}^1 \\ Sc_{i,j-\frac{1}{2}^+}^2 \end{pmatrix} \quad (\text{E.23})$$

Where:

$$Sc_{i+\frac{1}{2}^-, j}^1 = \frac{1}{2Fr^2} \left(\left(\frac{\xi_x}{J} \right)_{i+\frac{1}{2}, j} h_{i+\frac{1}{2}^-, j}^2 - \left(\frac{\xi_x}{J} \right)_{i, j} h_{i, j}^2 \right) \quad (\text{E.24})$$

$$Sc_{i-\frac{1}{2}^+, j}^1 = \frac{1}{2Fr^2} \left(\left(\frac{\xi_x}{J} \right)_{i, j} h_{i, j}^2 - \left(\frac{\xi_x}{J} \right)_{i-\frac{1}{2}, j} h_{i-\frac{1}{2}^+, j}^2 \right) \quad (\text{E.25})$$

$$Sc_{i, j+\frac{1}{2}^-}^1 = \frac{1}{2Fr^2} \left(\left(\frac{\eta_x}{J} \right)_{i, j+\frac{1}{2}} h_{i, j+\frac{1}{2}^-}^2 - \left(\frac{\eta_x}{J} \right)_{i, j} h_{i, j}^2 \right) \quad (\text{E.26})$$

$$Sc_{i, j-\frac{1}{2}^+}^1 = \frac{1}{2Fr^2} \left(\left(\frac{\eta_x}{J} \right)_{i, j} h_{i, j}^2 - \left(\frac{\eta_x}{J} \right)_{i, j-\frac{1}{2}^+} h_{i, j-\frac{1}{2}^+}^2 \right) \quad (\text{E.27})$$

$$Sc_{i+\frac{1}{2}^-, j}^2 = \frac{1}{2Fr^2} \left(\left(\frac{\xi_y}{J} \right)_{i+\frac{1}{2}, j} h_{i+\frac{1}{2}^-, j}^2 - \left(\frac{\xi_y}{J} \right)_{i, j} h_{i, j}^2 \right) \quad (\text{E.28})$$

$$Sc_{i-\frac{1}{2}^+, j}^2 = \frac{1}{2Fr^2} \left(\left(\frac{\xi_y}{J} \right)_{i, j} h_{i, j}^2 - \left(\frac{\xi_y}{J} \right)_{i-\frac{1}{2}, j} h_{i-\frac{1}{2}^+, j}^2 \right)$$

(E.29)

$$Sc_{i, j+\frac{1}{2}^-}^2 = \frac{1}{2Fr^2} \left(\left(\frac{\eta_y}{J} \right)_{i, j+\frac{1}{2}} h_{i, j+\frac{1}{2}^-}^2 - \left(\frac{\eta_y}{J} \right)_{i, j} h_{i, j}^2 \right) \quad (\text{E.30})$$

$$Sc_{i, j-\frac{1}{2}^+}^2 = \frac{1}{2Fr^2} \left(\left(\frac{\eta_y}{J} \right)_{i, j} h_{i, j}^2 - \left(\frac{\eta_y}{J} \right)_{i, j-\frac{1}{2}^+} h_{i, j-\frac{1}{2}^+}^2 \right) \quad (\text{E.31})$$

Then, the FV scheme that will be solved is:

$$\begin{aligned} \frac{dQ_{i,j}(t)}{dt} + \frac{J_{i,j}}{\Delta\xi} (F_{i+\frac{1}{2},j}^* - F_{i-\frac{1}{2},j}^*) + \frac{J_{i,j}}{\Delta\eta} (G_{i,j+\frac{1}{2}}^* - G_{i,j-\frac{1}{2}}^*) = \\ \frac{J_{i,j}}{\Delta\xi} (Sc_{i+\frac{1}{2}^-, j}^\xi + Sc_{i-\frac{1}{2}^+, j}^\xi) + \frac{J_{i,j}}{\Delta\eta} (Sc_{i, j}^\eta + Sc_{i, j+\frac{1}{2}^-}^\eta + Sc_{i, j-\frac{1}{2}^+}^\eta) \end{aligned} \quad (\text{E.32})$$

$$\begin{aligned} \frac{dQ_{i,j}(t)}{dt} + \frac{J_{i,j}}{\Delta\xi} (F_{i+\frac{1}{2},j}^* - Sc_{i+\frac{1}{2}-,j}^\xi - (F_{i-\frac{1}{2},j}^* + Sc_{i-\frac{1}{2}+,j}^\xi)) \\ + \frac{J_{i,j}}{\Delta\eta} (G_{i,j+\frac{1}{2}}^* - Sc_{i,j+\frac{1}{2}-}^\eta - (G_{i,j-\frac{1}{2}}^* + Sc_{i,j-\frac{1}{2}+}^\eta)) = 0 \end{aligned} \quad (\text{E.33})$$

Which is summarize as:

$$\frac{dQ_{i,j}(t)}{dt} + \frac{J_{i,j}}{\Delta\xi} (F_{i+\frac{1}{2},j}^- - F_{i-\frac{1}{2},j}^+) + \frac{J_{i,j}}{\Delta\eta} (G_{i,j+\frac{1}{2}}^- - G_{i,j-\frac{1}{2}}^+) = 0 \quad (\text{E.34})$$

Finally, the fluxes are defined as:

$$F_{i+\frac{1}{2},j}^- = F(Q_{i+\frac{1}{2},j}^*) + \begin{pmatrix} 0 \\ \frac{1}{2Fr^2} \left(\frac{\xi_x}{J} h_{i,j}^2 - \frac{\xi_x}{J} h_{i+\frac{1}{2}-,j}^2 \right) \\ \frac{1}{2Fr^2} \left(\frac{\xi_y}{J} h_{i,j}^2 - \frac{\xi_y}{J} h_{i+\frac{1}{2}-,j}^2 \right) \end{pmatrix} \quad (\text{E.35})$$

$$F_{i-\frac{1}{2},j}^+ = F(Q_{i-\frac{1}{2},j}^*) + \begin{pmatrix} 0 \\ \frac{1}{2Fr^2} \left(\frac{\xi_x}{J} h_{i,j}^2 - \frac{\xi_x}{J} h_{i-\frac{1}{2}+,j}^2 \right) \\ \frac{1}{2Fr^2} \left(\frac{\xi_y}{J} h_{i,j}^2 - \frac{\xi_y}{J} h_{i-\frac{1}{2}+,j}^2 \right) \end{pmatrix} \quad (\text{E.36})$$

$$G_{i,j+\frac{1}{2}}^- = G(Q_{i,j+\frac{1}{2}}^*) + \begin{pmatrix} 0 \\ \frac{1}{2Fr^2} \left(\frac{\eta_x}{J} h_{i,j}^2 - \frac{\eta_x}{J} h_{i,j+\frac{1}{2}-}^2 \right) \\ \frac{1}{2Fr^2} \left(\frac{\eta_y}{J} h_{i,j}^2 - \frac{\eta_y}{J} h_{i,j+\frac{1}{2}-}^2 \right) \end{pmatrix} \quad (\text{E.37})$$

$$G_{i,j-\frac{1}{2}}^+ = G(Q_{i,j-\frac{1}{2}}^*) + \begin{pmatrix} 0 \\ \frac{1}{2Fr^2} \left(\frac{\eta_x}{J} h_{i,j}^2 - \frac{\eta_x}{J} h_{i,j-\frac{1}{2}+}^2 \right) \\ \frac{1}{2Fr^2} \left(\frac{\eta_y}{J} h_{i,j}^2 - \frac{\eta_y}{J} h_{i,j-\frac{1}{2}+}^2 \right) \end{pmatrix} \quad (\text{E.38})$$

E.2. 2nd Order Hydrostatic Reconstruction

Following Audusse et al. (2004) methodology, it is possible to obtain a second order extension of the hydrostatic reconstruction. This is accomplished by reconstructing the hydrodynamic variables from limited and interpolated values at the cell interfaces. A MUSCL type method is used to reconstruct the cell values.

These new state variables will be obtained in three steps: gradient predictions inside each cell, linear extrapolation and limitation procedure. In this case, a **minmod** reconstruction method will be used.

Minmod Reconstruction: Reconstructed and linear extrapolated values at the cell edges, $i \pm \frac{1}{2}$, j and $i, j \pm \frac{1}{2}$ (See Fig. (E.2)) are defined as:

$$Q_{iL,j} = Q_{i,j} - \frac{\Delta\xi}{2} \nabla_i Q_{i,j} \quad (\text{E.39})$$

$$Q_{iR,j} = Q_{i,j} + \frac{\Delta\xi}{2} \nabla_i Q_{i,j} \quad (\text{E.40})$$

$$Q_{i,jL} = Q_{i,j} - \frac{\Delta\eta}{2} \nabla_j Q_{i,j} \quad (\text{E.41})$$

$$Q_{i,jR} = Q_{i,j} + \frac{\Delta\eta}{2} \nabla_j Q_{i,j} \quad (\text{E.42})$$

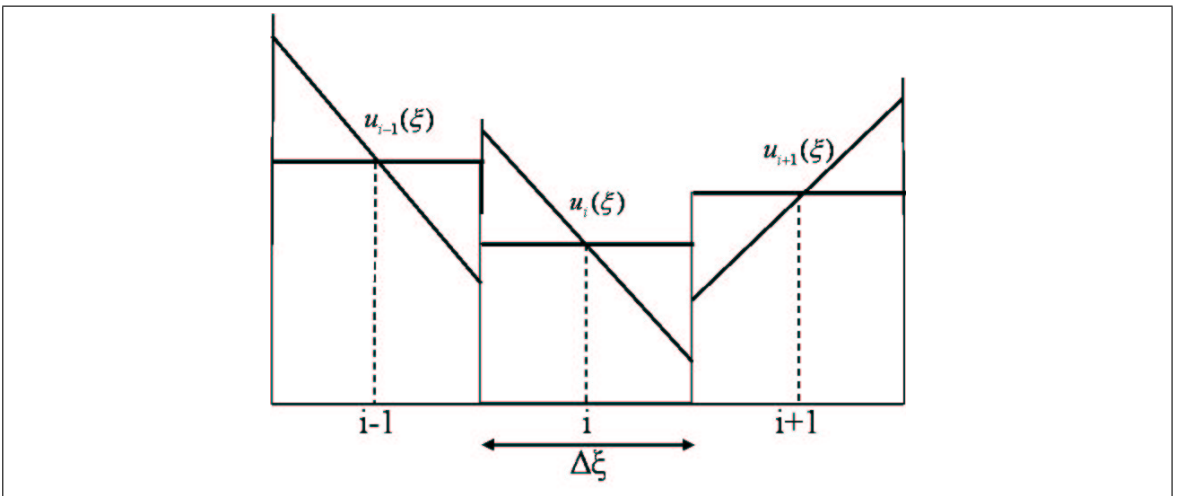


FIGURE E.2. Schematic drawing of the **Minmod** reconstruction method, Marche (2005)

The gradients ∇_i and ∇_j are calculated with:

$$\nabla_i Q_{i,j} = \text{minmod}\left(\frac{Q_{i,j} - Q_{i-1,j}}{\Delta\xi}, \frac{Q_{i+1,j} - Q_{i,j}}{\Delta\xi}\right) \quad (\text{E.43})$$

$$\nabla_j Q_{i,j} = \text{minmod}\left(\frac{Q_{i,j} - Q_{i,j-1}}{\Delta\eta}, \frac{Q_{i,j+1} - Q_{i,j}}{\Delta\eta}\right) \quad (\text{E.44})$$

With:

$$\text{minmod}(x, y) = \begin{cases} \min(x, y) & \text{if } x, y \geq 0 \\ \max(x, y) & \text{if } x, y < 0 \\ 0 & \text{if other case} \end{cases} \quad (\text{E.45})$$

These limited values at each cell interface: $Q_{iL,j}$, $Q_{iR,j}$, $Q_{i,jL}$, $Q_{i,jR}$, will be used to the hydrostatic reconstruction of the water depth instead of $Q_{i,j}$. The reconstruction of the topography, $z_{i,j}$, is obtained from the reconstruction of the free surface elevation, $(h + z)$ and the reconstruction of the water depth. In order to accomplish the well-balance property of the model and its consistency, a center discretization of the bed-slope source term must be added (Ver (Audusse et al., 2004)).

Summarizing, the second order reconstruction methodology is:

(i) Linear Reconstruction of the state variables $Q_{i,j}$:

$Q_{iL,j}$, $Q_{iR,j}$, $Q_{i,jL}$, $Q_{i,jR}$ are obtained using the **minmod** reconstruction.

(ii) Linear Reconstruction of the free surface $(h + z)_{i,j}$:

$(h + z)_{iL,j}$, $(h + z)_{iR,j}$, $(h + z)_{i,jL}$, $(h + z)_{i,jR}$ are calculated using **minmod** reconstruction.

(iii) Topography reconstruction $z_{i,j}$:

$$z_{iL,j} = (h + z)_{iL,j} - h_{iL,j} \quad (\text{E.46})$$

$$z_{iR,j} = (h + z)_{iR,j} - h_{iR,j} \quad (\text{E.47})$$

$$z_{i,jL} = (h + z)_{i,jL} - h_{i,jL} \quad (\text{E.48})$$

$$z_{i,jR} = (h + z)_{i,jR} - h_{i,jR} \quad (\text{E.49})$$

(iv) Hydrostatic Reconstruction:

$$h_{i+\frac{1}{2}^-, j} = \max(0, h_{iR, j} + z_{iR, j} - z_{i+\frac{1}{2}, j}) \quad (\text{E.50})$$

$$h_{i+\frac{1}{2}^+, j} = \max(0, h_{i+1L, j} + z_{i+1L, j} - z_{i+\frac{1}{2}, j}) \quad (\text{E.51})$$

$$h_{i, j+\frac{1}{2}^-} = \max(0, h_{i, jR} + z_{i, jR} - z_{i, j+\frac{1}{2}}) \quad (\text{E.52})$$

$$h_{i, j+\frac{1}{2}^+} = \max(0, h_{i, j+1L} + z_{i, j+1L} - z_{i, j+\frac{1}{2}}) \quad (\text{E.53})$$

Then, the reconstructed values at the cell interfaces are:

$$Q_{i+\frac{1}{2}^+, j} = \begin{pmatrix} h_{i+\frac{1}{2}^+, j} \\ h_{i+\frac{1}{2}^+, j} u_{(i+1)L, j} \\ h_{i+\frac{1}{2}^+, j} u_{(i+1)L, j} \end{pmatrix}, \quad Q_{i+\frac{1}{2}^-, j} = \begin{pmatrix} h_{i+\frac{1}{2}^-, j} \\ h_{i+\frac{1}{2}^-, j} u_{iR, j} \\ h_{i+\frac{1}{2}^-, j} u_{iR, j} \end{pmatrix} \quad (\text{E.54})$$

$$Q_{i, j+\frac{1}{2}^+} = \begin{pmatrix} h_{i, j+\frac{1}{2}^+} \\ h_{i, j+\frac{1}{2}^+} u_{i, (j+1)L} \\ h_{i, j+\frac{1}{2}^+} v_{i, (j+1)L} \end{pmatrix}, \quad Q_{i, j+\frac{1}{2}^-} = \begin{pmatrix} h_{i, j+\frac{1}{2}^-} \\ h_{i, j+\frac{1}{2}^-} u_{i, jR} \\ h_{i, j+\frac{1}{2}^-} v_{i, jR} \end{pmatrix} \quad (\text{E.55})$$

(v) Fluxes:

$$\begin{aligned} F_{i+\frac{1}{2}, j}^- &= F(Q_{i+\frac{1}{2}, j}^*(0, Q_{i+\frac{1}{2}^-, j}, Q_{i+\frac{1}{2}^+, j})) \\ &+ \frac{1}{2Fr^2} \begin{pmatrix} 0 \\ \left(\frac{\xi_x}{J}\right)_{i,j} h_{iR, j}^2 - \left(\frac{\xi_x}{J}\right)_{i+\frac{1}{2}^-, j} h_{i+\frac{1}{2}^-, j}^2 \\ \left(\frac{\xi_y}{J}\right)_{i,j} h_{iR, j}^2 - \left(\frac{\xi_y}{J}\right)_{i+\frac{1}{2}^-, j} h_{i+\frac{1}{2}^-, j}^2 \end{pmatrix} \end{aligned} \quad (\text{E.56})$$

$$\begin{aligned} F_{i-\frac{1}{2}, j}^+ &= F(Q_{i-\frac{1}{2}, j}^*(0, Q_{i-\frac{1}{2}^-, j}, Q_{i-\frac{1}{2}^+, j})) \\ &+ \frac{1}{2Fr^2} \begin{pmatrix} 0 \\ \left(\frac{\xi_x}{J}\right)_{i,j} h_{iL, j}^2 - \left(\frac{\xi_x}{J}\right)_{i-\frac{1}{2}^+, j} h_{i-\frac{1}{2}^+, j}^2 \\ \left(\frac{\xi_y}{J}\right)_{i,j} h_{iL, j}^2 - \left(\frac{\xi_y}{J}\right)_{i-\frac{1}{2}^+, j} h_{i-\frac{1}{2}^+, j}^2 \end{pmatrix} \end{aligned} \quad (\text{E.57})$$

$$G_{i,j+\frac{1}{2}}^- = G(Q_{i,j+\frac{1}{2}}^*(0, Q_{i,j+\frac{1}{2}}^-, Q_{i,j+\frac{1}{2}}^+)) \\ + \frac{1}{2Fr^2} \begin{pmatrix} 0 \\ \left(\frac{\eta_x}{J}\right)_{i,j} h_{i,jR}^2 - \left(\frac{\eta_x}{J}\right)_{i,j+\frac{1}{2}-} h_{i,j+\frac{1}{2}-}^2 \\ \left(\frac{\eta_y}{J}\right)_{i,j} h_{i,jR}^2 - \left(\frac{\eta_y}{J}\right)_{i,j+\frac{1}{2}-} h_{i,j+\frac{1}{2}-}^2 \end{pmatrix} \quad (\text{E.58})$$

$$G_{i,j-\frac{1}{2}}^+ = G(Q_{i,j-\frac{1}{2}}^*(0, Q_{i,j-\frac{1}{2}}^-, Q_{i,j-\frac{1}{2}}^+)) \\ + \frac{1}{2Fr^2} \begin{pmatrix} 0 \\ \left(\frac{\eta_x}{J}\right)_{i,j} h_{i,jL}^2 - \left(\frac{\eta_x}{J}\right)_{i,j-\frac{1}{2}+} h_{i,j-\frac{1}{2}+}^2 \\ \left(\frac{\eta_y}{J}\right)_{i,j} h_{i,jL}^2 - \left(\frac{\eta_y}{J}\right)_{i,j-\frac{1}{2}+} h_{i,j-\frac{1}{2}+}^2 \end{pmatrix} \quad (\text{E.59})$$

$$Sc_{i,j} = -\frac{1}{Fr^2} \begin{pmatrix} 0 \\ \xi_x \left(\frac{h_{iR,j} + h_{iL,j}}{2} \right) \left(\frac{z_{iR,j} - z_{iL,j}}{\Delta\xi} \right) + \eta_x \left(\frac{h_{i,jR} + h_{i,jL}}{2} \right) \left(\frac{z_{i,jR} - z_{i,jL}}{\Delta\eta} \right) \\ \xi_y \left(\frac{h_{iR,j} + h_{iL,j}}{2} \right) \left(\frac{z_{iR,j} - z_{iL,j}}{\Delta\xi} \right) + \eta_y \left(\frac{h_{i,jR} + h_{i,jL}}{2} \right) \left(\frac{z_{i,jR} - z_{i,jL}}{\Delta\eta} \right) \end{pmatrix} \quad (\text{E.60})$$

Finally, the FV formulation of the problem is given by:

$$\frac{dQ_{i,j}(t)}{dt} + \frac{J_{i,j}}{\Delta\xi} (F_{i+\frac{1}{2},j}^- - F_{i-\frac{1}{2},j}^+) + \frac{J_{i,j}}{\Delta\eta} (G_{i,j+\frac{1}{2}}^- - G_{i,j-\frac{1}{2}}^+) = Sc_{i,j} \quad (\text{E.61})$$

APPENDIX F. BOUNDARY CONDITIONS

Due to the use of the MUSCL reconstruction, two lines of ghost cells are needed for the computation of the state variables at the boundaries of the domain. The computational domain is shown in Fig. F.1).

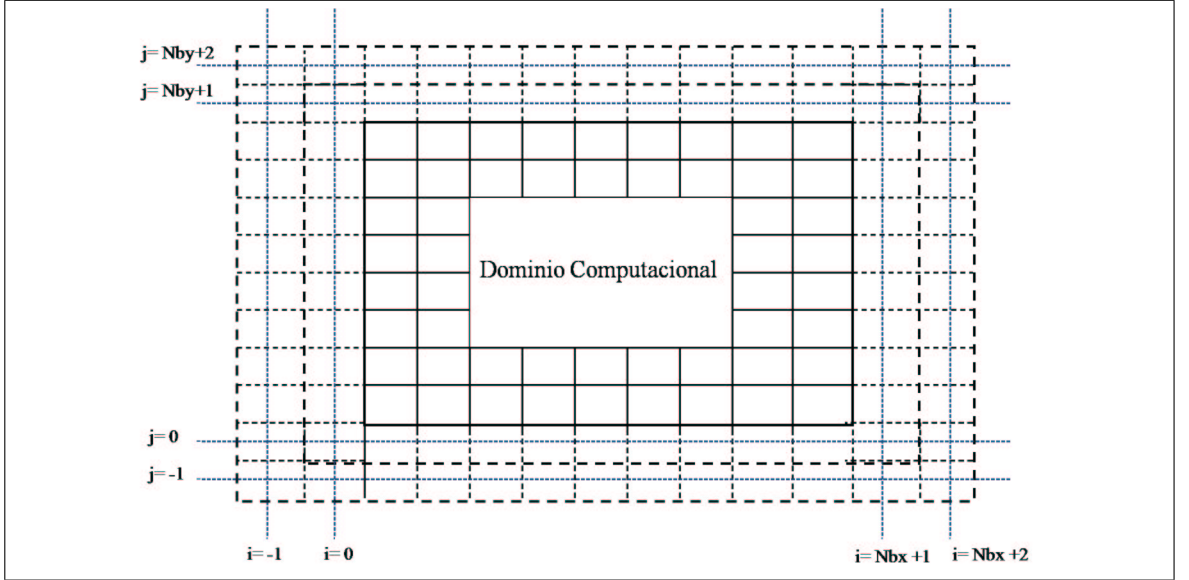


FIGURE F.1. Schematic computational domain including ghost cells, Marche (2005)

F.1. Reflective solid wall

This boundary condition represents the behavior of a solid wall that closes the domain and reflects any information that propagates over it. The condition is given by:

$$h_{N+1} = h_N, \quad u'_{N+1} = -u'_N, \quad v'_{N+1} = -v'_N, \quad (\text{F.1})$$

$$h_{N+2} = h_{N-1}, \quad u'_{N+2} = -u'_{N-1}, \quad v'_{N+2} = -v'_{N-1}, \quad (\text{F.2})$$

Where N and $N - 1$ denote the last two cells inside the computational domain, $N + 1$ and $N + 2$, the two cells outside of the domain, u' and v' are the normal and tangential components of the velocity to the boundary of the domain.

F.2. Transmissive boundary

This condition represents an open boundary. It provides a simple absorbing conditions that allows information to leave the domain as it was infinite.

$$h_{N+1} = h_N, \quad u'_{N+1} = u'_N, \quad v'_{N+1} = v'_N, \quad (\text{F.3})$$

$$h_{N+2} = h_{N-1}, \quad u'_{N+2} = u'_{N-1}, \quad v'_{N+2} = v'_{N-1}, \quad (\text{F.4})$$

F.3. Periodic boundary condition

This condition connects both ends of the domain and is equal to have no boundary.

$$h_{N+1} = h_1, \quad u'_{N+1} = u'_1, \quad v'_{N+1} = v'_1, \quad (\text{F.5})$$

$$h_{N+2} = h_2, \quad u'_{N+2} = u'_2, \quad v'_{N+2} = v'_2, \quad (\text{F.6})$$

Tangent and normal velocities correspond to the contravariant components of the velocity. Also, the metrics at the boundaries are needed, which are defined as:

$$(x_\xi)_{N+1} = (x_\xi)_N, \quad (y_\xi)_{N+1} = (y_\xi)_N \quad (\text{F.7})$$

$$(x_\xi)_{N+2} = (x_\xi)_{N-1}, \quad (y_\xi)_{N+2} = (y_\xi)_{N-1} \quad (\text{F.8})$$

$$(x_\eta)_{N+1} = (x_\eta)_N, \quad (y_\eta)_{N+1} = (y_\eta)_N \quad (\text{F.9})$$

$$(x_\eta)_{N+2} = (x_\eta)_{N-1}, \quad (y_\eta)_{N+2} = (y_\eta)_{N-1} \quad (\text{F.10})$$

$$(\text{F.11})$$

According to the latter, the boundary conditions are defined as:

Solid wall:

$$u_{N+1} = -u_N, \quad v_{N+1} = -v_N, \quad (\text{F.12})$$

$$u_{N+2} = -u_{N-1}, \quad v_{N+2} = -v_{N-1}, \quad (\text{F.13})$$

$$(\text{F.14})$$

Transmissive:

$$u_{N+1} = u_N, \quad v_{N+1} = v_N, \quad (\text{F.15})$$

$$u_{N+2} = u_{N-1}, \quad v_{N+2} = v_{N-1}, \quad (\text{F.16})$$

$$(\text{F.17})$$

Periodic:

$$u_{N+1} = u_1, \quad v_{N+1} = v_1, \quad (\text{F.18})$$

$$u_{N+2} = u_2, \quad v_{N+2} = v_2, \quad (\text{F.19})$$

$$(\text{F.20})$$

F.4. Absorbing/Generating Boundary Condition

This boundary condition allow us to introduce information to the domain, such as waves or hydrographs, and to evacuate back travelling waves. The implementation of this boundary condition is based in the work of Cienfuegos et al. (2007); Mignot and Cienfuegos (2009).

The methodology behind this boundary condition is to solve a Riemann problem at the boundary of the computational domain in order to determine the state variables at that place. Since a RK scheme is used to integrate in time the NSWE, the methodology is applied to each RK step, with the objective to find the state values at A' y A'' (Fig. (F.2)). At the $\xi = 0$ boundary, the following Riemann invariants and characteristic trajectories are

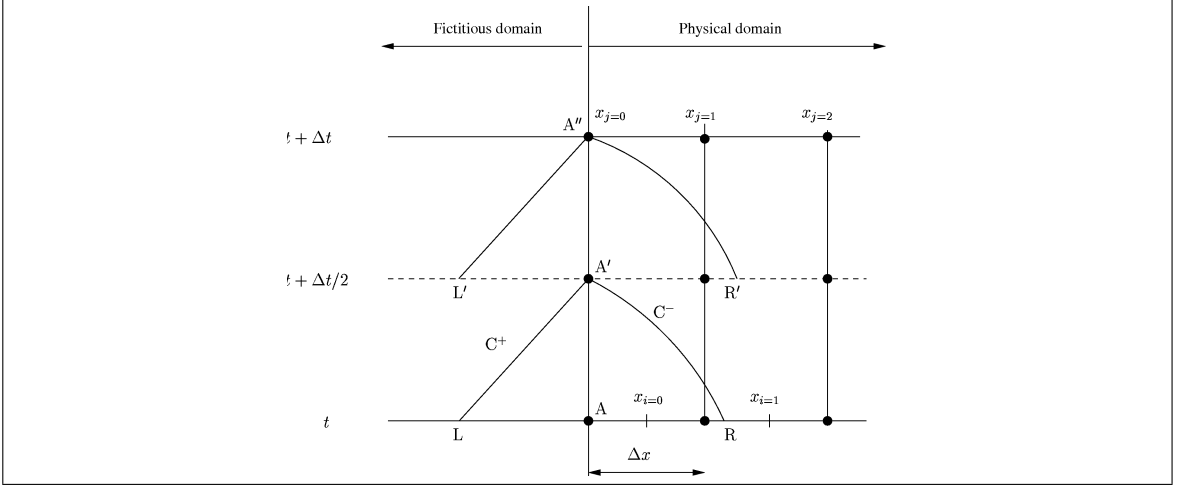


FIGURE F.2. Absorbing/Generating boundary condition scheme, Cienfuegos et al. (2007)

defined:

$$R^+ = U + 2C\sqrt{\xi_x^2 + \xi_y^2} \quad (\text{F.21})$$

$$R^- = U - 2C\sqrt{\xi_x^2 + \xi_y^2} \quad (\text{F.22})$$

$$\frac{dR^+}{dt} = -\frac{1}{Fr^2} z_\xi (\xi_x^2 + \xi_y^2) - \frac{\tau_{bx}}{\rho h} \xi_x \quad \text{sobre} \quad \frac{d\xi}{dt} = U^1 + C\sqrt{\xi_x^2 + \xi_y^2} \quad (\text{F.23})$$

$$\frac{dR^-}{dt} = -\frac{1}{Fr^2} z_\xi (\xi_x^2 + \xi_y^2) - \frac{\tau_{bx}}{\rho h} \xi_x \quad \text{sobre} \quad \frac{d\xi}{dt} = U^1 - C\sqrt{\xi_x^2 + \xi_y^2} \quad (\text{F.24})$$

The condition has been only implemented in the case of normal wave entering the domain and for uniform discretizations in the signal direction, in such way that in the boundary $\xi_y = 0$ and $v = 0$, which is shown in Fig. (F.3). Thus, the Riemann invariants and the characteristic trajectories are redefined as:

$$R^+ = U + 2C\xi_x \quad (\text{F.25})$$

$$R^- = U - 2C\xi_x \quad (\text{F.26})$$

$$\frac{dR^+}{dt} = -\frac{1}{Fr^2} z_\xi \xi_x^2 - \frac{\tau_{bx}}{\rho h} (\xi_x + \xi_y) \quad \text{sobre} \quad \frac{d\xi}{dt} = u\xi_x + C\xi_x \quad (\text{F.27})$$

$$\frac{dR^-}{dt} = -\frac{1}{Fr^2} z_\xi \xi_x^2 - \frac{\tau_{bx}}{\rho h} (\xi_x + \xi_y) \quad \text{sobre} \quad \frac{d\xi}{dt} = u^1 - C\xi_x \quad (\text{F.28})$$

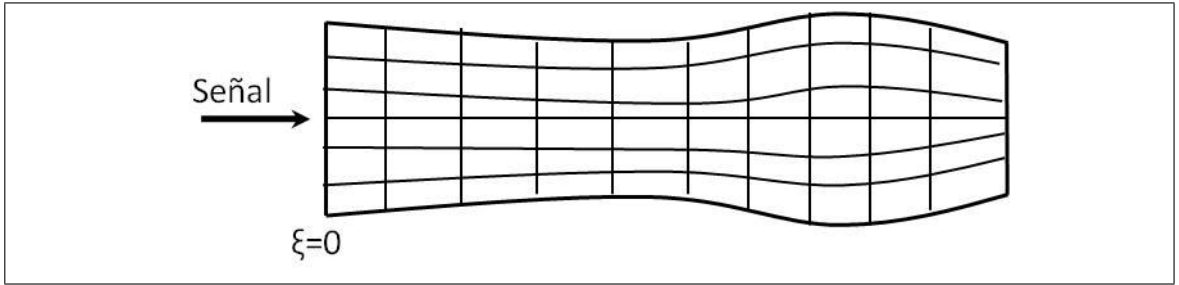


FIGURE F.3. Absorbing/Generating boundary condition meshes

F.4.0.1. First RK step

In this step, the state variables at the A' point are calculated integrating from t to $t + \Delta t/2$. From an outside point L a positive characteristic leaves to the A interface, R_L^+ , that arrives at $t + \Delta t/2$. The value of this characteristic is given by:

$$R_L^+ = \xi_{xL}(u_L + 2C_L) \quad (\text{F.29})$$

Where, depending of the information introduced to the domain, a wave or a given discharge, u_L , C_L and ξ_{xL} are calculated. At the same time, from an unknown point R inside the domain, a negative characteristic leaves, which value is calculated as:

$$R_R^- = \xi_{xR}(u_R - 2C_R) \quad (\text{F.30})$$

To find u_R , C_R and ξ_R , since the position of R is unknown, the following implicit trajectory problem is solved:

$$\int_R^{A'} d\xi = \int_{A'}^R \xi_x(u - C) dt \quad (\text{F.31})$$

Which can be approximately solved by:

$$0 = \xi|_R - \xi|_{A'} + (u - C)\xi_x|_R \frac{\Delta t}{2} \quad (\text{F.32})$$

After calculating R_L^+ y R_R^- , the values at A' are found by solving the following characteristic problems:

From L to A' :

$$\int_L^{A'} dR^+ = -\frac{1}{Fr^2} \int_L^{A'} z_\xi \xi_x^2 dt - \frac{1}{\rho} \int_L^{A'} \frac{\tau_{bx}}{h} \xi_x dt \quad (\text{F.33})$$

$$R_{A'}^+ = R_L^+ - \frac{1}{Fr^2} \frac{1}{2} (z_\xi \xi_x^2|_L + z_\xi \xi_x^2|_{A'}) \frac{\Delta t}{2} - \frac{1}{\rho} \frac{\tau_{bx}|_L}{h|_L} \xi_x|_L \frac{\Delta t}{2} \quad (\text{F.34})$$

From R to A' :

$$\int_R^{A'} dR^+ = -\frac{1}{Fr^2} \int_R^{A'} z_\xi \xi_x^2 dt - \frac{1}{\rho} \int_R^{A'} \frac{\tau_{bx}}{h} \xi_x dt \quad (\text{F.35})$$

$$R_{A'}^+ = R_R^+ - \frac{1}{Fr^2} \frac{1}{2} (z_\xi \xi_x^2|_R + z_\xi \xi_x^2|_{A'}) \frac{\Delta t}{2} - \frac{1}{\rho} \frac{\tau_{bx}|_R}{h|_R} \xi_x|_R \frac{\Delta t}{2} \quad (\text{F.36})$$

Then,

$$R_{A'}^+ = \xi_{xA'} (u_{A'} + 2C_{A'}) \quad (\text{F.37})$$

$$R_{A'}^- = \xi_{xA'} (u_{A'} - 2C_{A'}) \quad (\text{F.38})$$

$$C = \sqrt{\frac{h}{Fr^2}} \quad (\text{F.39})$$

Thus, the state variables at the A' point at time $t + \Delta t/2$ are calculated as:

$$h_{A'} = \frac{(R_{A'}^+ - R_A^-)^2}{16\xi_{xA'}^2} Fr^2 \quad (\text{F.40})$$

$$u_{A'} = \frac{R_{A'}^+ - R_A^-}{2\xi_{xA'}} \quad (\text{F.41})$$

F.4.0.2. Second RK step

In the second RK step, the estimation of the state variables at A' is improved. The values obtained for the first RK step are used, and the Riemann invariants and the trajectories are recalculated as:

$$R_{A'}^+ = R_L^+ - \frac{1}{Fr^2} \frac{1}{2} (z_\xi \xi_x^2|_L + z_\xi \xi_x^2|_{A'}) \frac{\Delta t}{2} - \frac{1}{\rho} \frac{1}{2} \left(\frac{\tau_{bx}|_L}{h|_L} \xi_x|_L + \frac{\tau_{bx}|_{A'*}}{h|_{A'*}} \xi_x|_L \right) \frac{\Delta t}{2} \quad (\text{F.42})$$

$$R_{A'}^+ = R_R^+ - \frac{1}{Fr^2} \frac{1}{2} (z_\xi \xi_x^2|_R + z_\xi \xi_x^2|_{A'}) \frac{\Delta t}{2} - \frac{1}{\rho} \frac{1}{2} \left(\frac{\tau_{bx}|_R}{h|R} \xi_x|R + \frac{\tau_{bx}|_{A'*}}{h|_{A'*}} \xi_x|R \right) \frac{\Delta t}{2} \quad (\text{F.43})$$

$$0 = \xi|R - \xi|_{A'} + \frac{1}{2} ((u - C)\xi_x|R + (u - C)\xi_x|_{A'*}) \frac{\Delta t}{2} \quad (\text{F.44})$$

Where A'^* corresponds to the state values found in the first RK step.

In the following RK steps, the same methodology is applied, from $t + \Delta t/2$ to $t + \Delta t$ (A' to A'').

Finally, for at each time step, state variables at the computational domain boundaries, which include outside information and inside information, are found.

F.5. Ghost Cells Bathymetry

The bathymetry of the ghost cells is set to be the same as the first, or last, cell of the real domain, in order to maintain the free surface elevation at the boundary for the transmissive, solid wall and periodic boundary conditions, since the depth is the same.

APPENDIX G. TIME INTEGRATION METHOD

In this section the methodology used to obtain the state variables at time t_{n+1} from the known variables at time t_n , considering the effects of friction and of the numerical fluxes.

First, the friction effect is calculated using the time step defined by the CFL condition. This process was explained in Chapter 2. Then, a 4th order Runge-Kutta (RK) scheme is applied to integrate in time the Hypervbolic NSWE step of the model. Considering the second order accuracy in space finite volume scheme:

$$\frac{\partial Q_{i,j}}{\partial t} = Sc_{i,j} - \frac{1}{\Delta\xi}(F_{i+\frac{1}{2}^-,j} - F_{i-\frac{1}{2}^+,j}) - \frac{1}{\Delta\xi}(G_{i,j+\frac{1}{2}^-} - G_{i,j-\frac{1}{2}^+}) = f(Q_{i,j}, t) \quad (\text{G.1})$$

Then, the applied RK method is defined as:

$$Q^{n+1} = Q^n + \frac{1}{6}(K_1 + 2K_2 + 2K_3 + K_4)\Delta t \quad (\text{G.2})$$

Where,

$$K_1 = f(t_n, Q^n) \quad (\text{G.3})$$

$$K_2 = f(t_n, Q^{n+\frac{1}{2}^*}) \quad (\text{G.4})$$

$$K_3 = f(t_n, Q^{n+\frac{1}{2}^{**}}) \quad (\text{G.5})$$

$$K_4 = f(t_n, Q^{n+1^*}) \quad (\text{G.6})$$

With,

$$Q^{n+\frac{1}{2}^*} = Q^n + \frac{\Delta t}{2}K_1 \quad (\text{G.7})$$

$$Q^{n+\frac{1}{2}^{**}} = Q^n + \frac{\Delta t}{2}K_2 \quad (\text{G.8})$$

$$Q^{n+1^*} = Q^n + \Delta t K_3 \quad (\text{G.9})$$

APPENDIX H. BENCHMARK CASES

In this appendix, various test cases simulated with the curvilinear model are presented. These test cases and the ones presented in Chapter 2, exemplify each one of the capabilities of the model.

H.1. Steady State at rest

This case considers a two-dimensional steady state flow over variable topography with dry zones. The objective of this test is to show the *well-balance* property of the model and the ability to preserve steady state.

The topography is defined by:

$$z(x, y) = 0.5 \exp(-(r/\sigma)^2) \quad (\text{H.1})$$

Where $r = \sqrt{(x - xo)^2 + (y - yo)^2}$, $\sigma = 0.5$ and $xo = yo = 5$. The initial condition of the free surface is such that a part of the domain is dry, it is defined as $h + z = \max(z, 0.3)$. Null flow and velocities is impose in the domain. In Fig. H.1 the topography and the free surface after 200 s of simulation is shown.

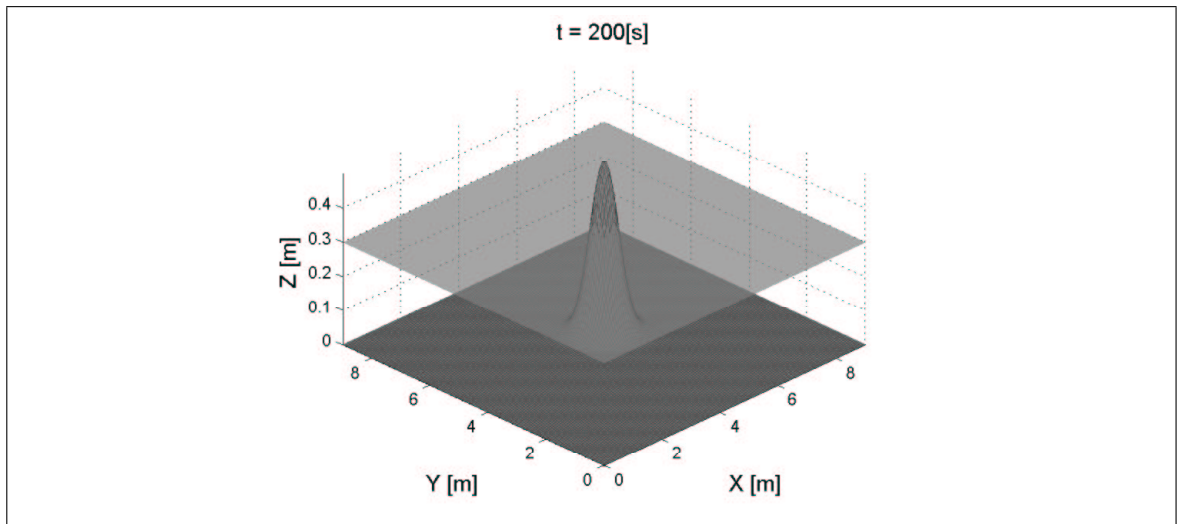


FIGURE H.1. Estado Estacionario: Batimetría y Condiciones Iniciales

In Fig. H.2(a) a center profile of the water depth and the topography at 200 s are presented, in Fig. H.2(b) the discharge evolution at point $(x, y) = (0, 0)$ is shown. Water depth maintains constant and no discharge is observed during the 200 s of simulation, thus, preserving the steady state at rest.

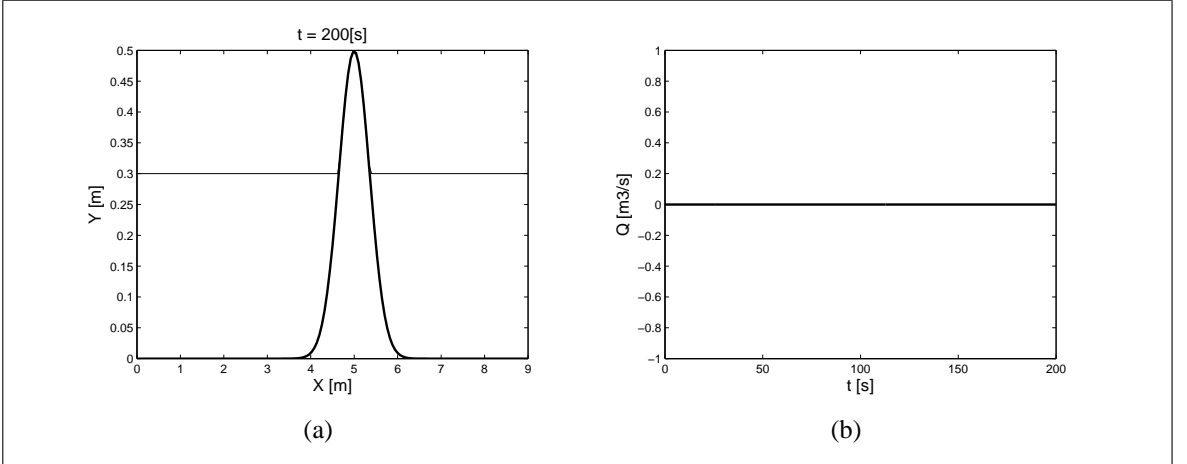


FIGURE H.2. Estado Estacionario $t=200$ s: (a) Corte transversal, (b) Serie de Tiempo de Caudal en $(x, y) = (0, 0)$

H.2. 1D Dam-break

This test has been classically used to validate NSWE numerical models. It consist in two different states, separated by a discontinuity: the dam. The dam is instantly removed at $t = 0$ s, and a shock-wave propagates downstream and a rarefaction wave propagates upstream. An schematic drawing of the 1D dam-break initial configuration is shown in Fig. H.3. The ratio between the water depths downstream the dam and upstream of it, h_t/h_r , is known as *depth ratio*, as this ratio decreases, the test becomes more demanding for the numerical model. In this case, the model was tested with a 0 depth ratio, meaning that $h_t = 0$ m. Water depth upstream the dam was settled to be $h_r = 1$ m. Numerical solutions were compared with the analytical solutions proposed in Stoker (1992).

A rectangular channel of 50 m length and 1 m width was considered for the simulations. It was discretized in a regular and uniform mesh of size $\Delta x = 0.05$ m. The discontinuity is located at the center of the channel. Fig. H.4 shows a comparison between

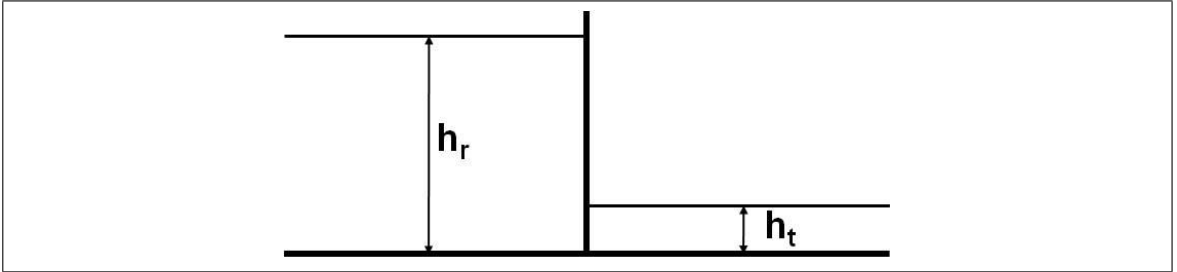


FIGURE H.3. 1D Dam-break: Schematic drawing of the initial conditions

numerical and analytical solutions of the evolution of the free surface after the breaking of the dam. Velocity evolution and discharge per unit width are shown in Fig. H.5. Excellent agreement is found between numerical and analytical solutions for the free surface elevation and for the discharge, small differences are found for the velocity. The model underestimates the velocity of the shock-wave front when wetting the dry zones. This could be improved with a thinner discretization of the domain. Other test were performed with coarser grids and results improved when using a refined discretization of the domain. This test shows the shock-capturing ability of the model and the capability to flood dry zones.

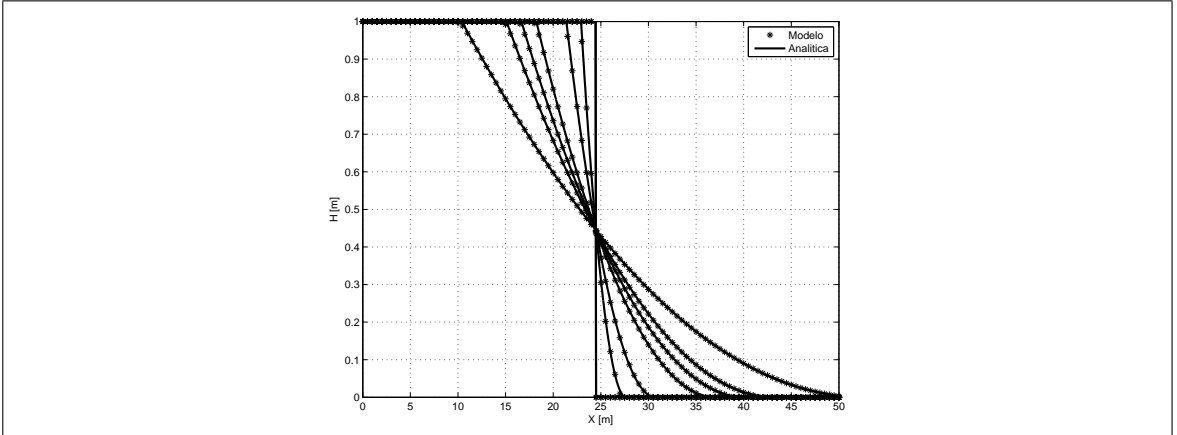


FIGURE H.4. 1D Dam-break: Free surfave profiles at different times

H.3. 2D Dam-break

In this case a partial 2D dam-break over a flat and frictionless bed is studied. No analytical solutions exist for this case, but the results can be compared with other numerical results, such as Alcrudo and García-Navarro (1993); Baghlan et al. (2008).

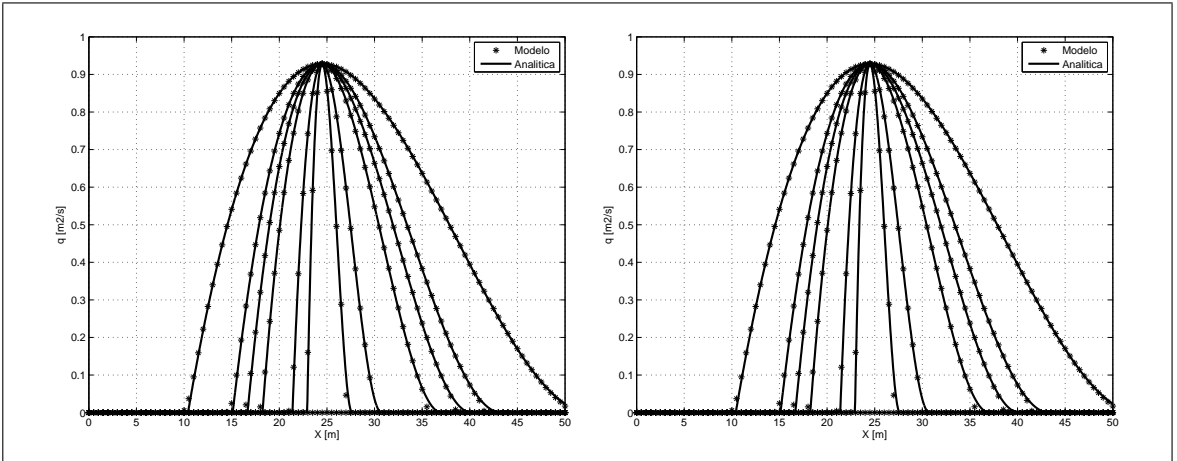


FIGURE H.5. 1D Dam-break: (a) Velocity profiles, (b) Discharge per unit width profiles

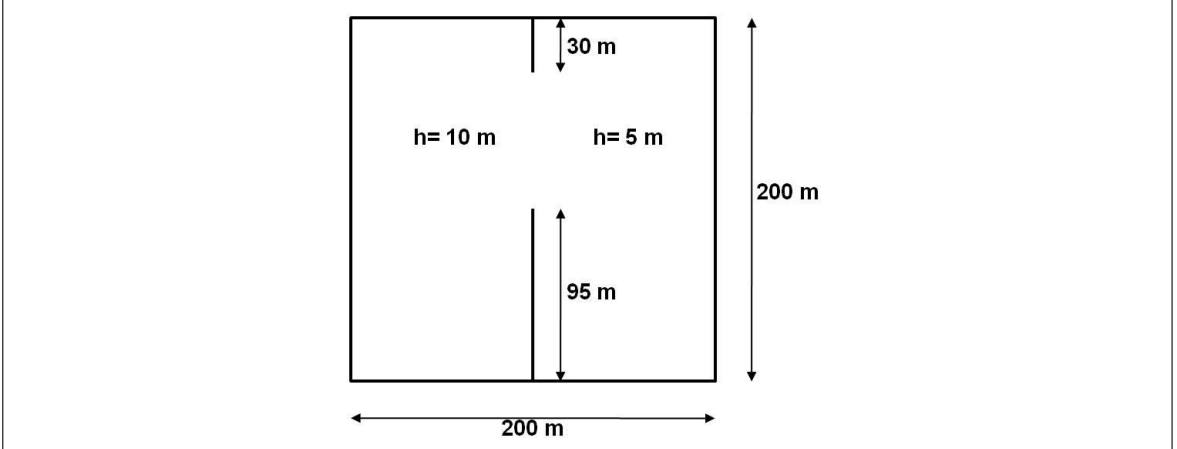


FIGURE H.6. 2D dam-break: Schematic plan view of the domain

The breaking occurs over a flat channel of 200 m long and 200 m width. The dam opening is 75 m width. A schematic drawing of the domain configuration is shown in Fig. H.6. Water depth upstream the dam is initially 10 m and downstream the dam is 5 m. At the breaking, a wave is propagated downstream that spreads to the sides of the channel, at the same time, a rarefaction wave propagates upstream of the channel decreasing the water depth. Free surface elevation 7.2 s after the break, using a uniform and regular grid of 40x40 cells, is shown in Fig. H.7(a). A contour map of the same result is shown in Fig. H.7(b). The propagation of a rarefaction wave involves high velocity gradients in the boundaries of the broken zone of the dam, which represent a demanding test for the numerical model. The numerical results presented in the latter figures show that the solution is stable and

smooth in the complicated zones. The velocity field at the same time is shown in Fig. H.8, where the two-dimensional character of the break is observed . The obtained numerical results are in agreement with those studied in the literature.

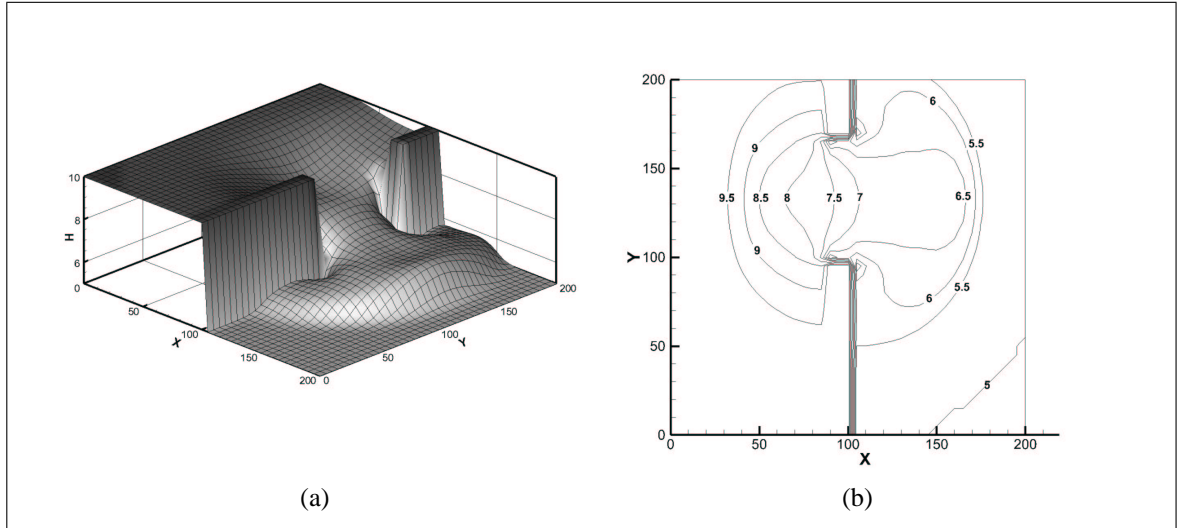


FIGURE H.7. 2D Dam-break, 7.2 s after de breaking: (a) 3D view of the free surface elevation, (b) Contour map of the free surface

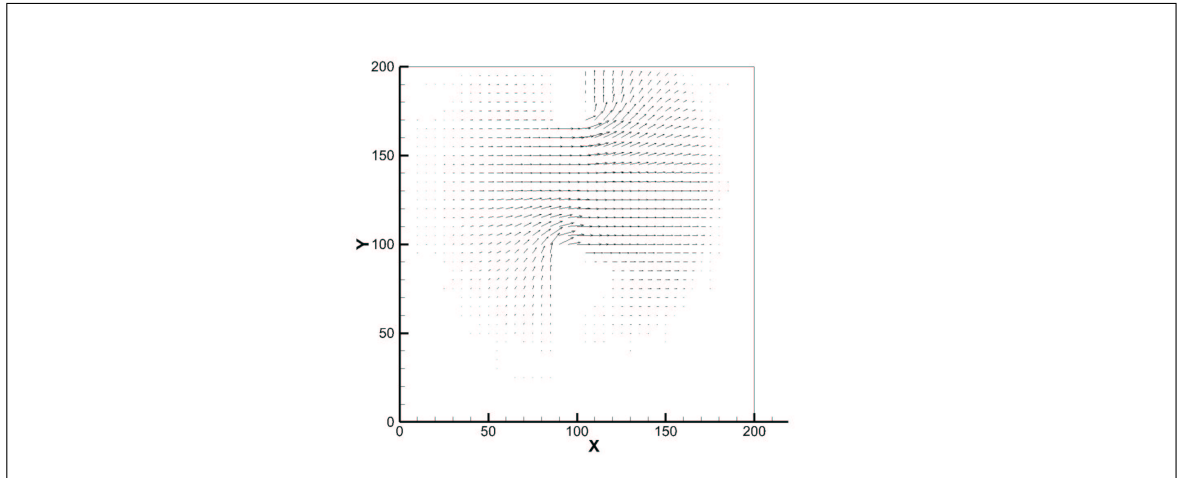


FIGURE H.8. 2D Dam-break: Velocity field

H.4. Thacker's curved solution

In Thacker (1981), some analytical solutions to shallow water flows are presented. One of them is the analytical solution for a bidimensional and symmetric oscillating flow over

a frictionless parabolic basin (see Fig. H.9). The basin is defined as:

$$z(r) = h_0 \left(1 - \frac{r^2}{a^2} \right) \quad (\text{H.2})$$

where, h_0 is the water depth at the center of the basin and a is the distance from the center point to the shoreline (see Fig. H.10). This test is interesting since one of the few cases that involves moving shoreline and wave *run-up* and *run-down* without applying any special boundary condition. Besides, since the basin is frictionless, no energy dissipation occurs, thus the solution is periodic and do not decay in time.

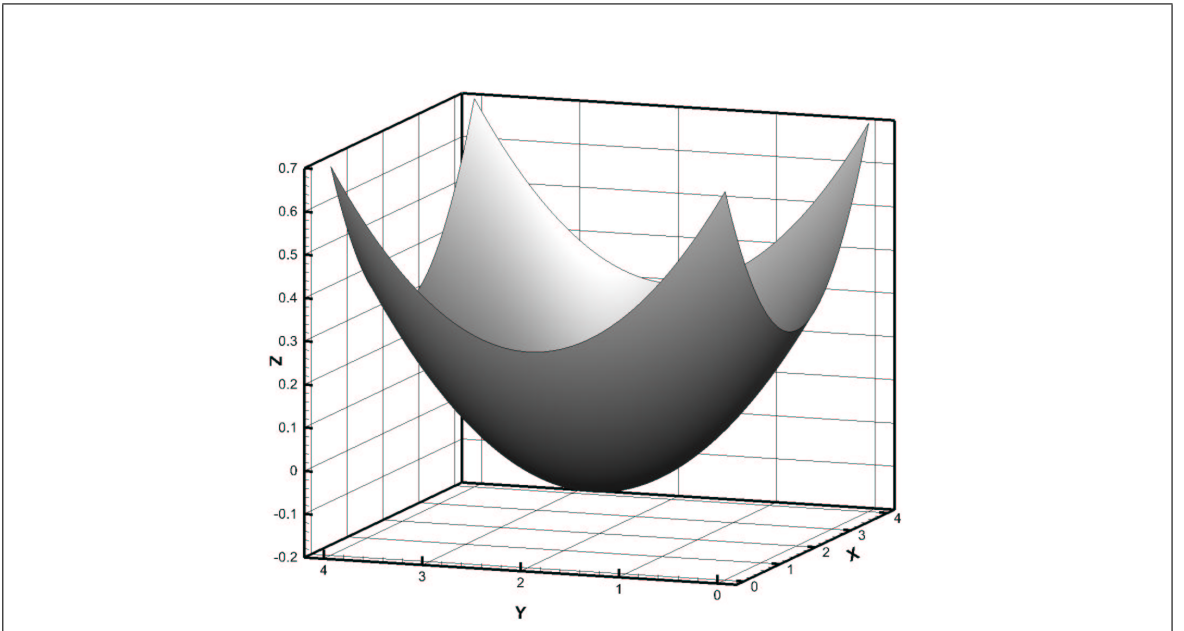


FIGURE H.9. Thacker's curved solution: Parabolic basin

The analytical solution of the problem is given by:

$$h(r, t) = h_0 \left[\frac{(1 - A^2)^{1/2}}{1 - Acos(\omega t)} - 1 - \frac{r^2}{a^2} \left(\frac{1 - A^2}{(1 - Acos(\omega t))^2} - 1 \right) \right] \quad (\text{H.3})$$

$$u(x) = \frac{1}{1 - Acos(\omega t)} \left(\frac{1}{2} \omega x A sin(\omega t) \right) \quad (\text{H.4})$$

$$v(y) = \frac{1}{1 - Acos(\omega t)} \left(\frac{1}{2} \omega y A sin(\omega t) \right) \quad (\text{H.5})$$

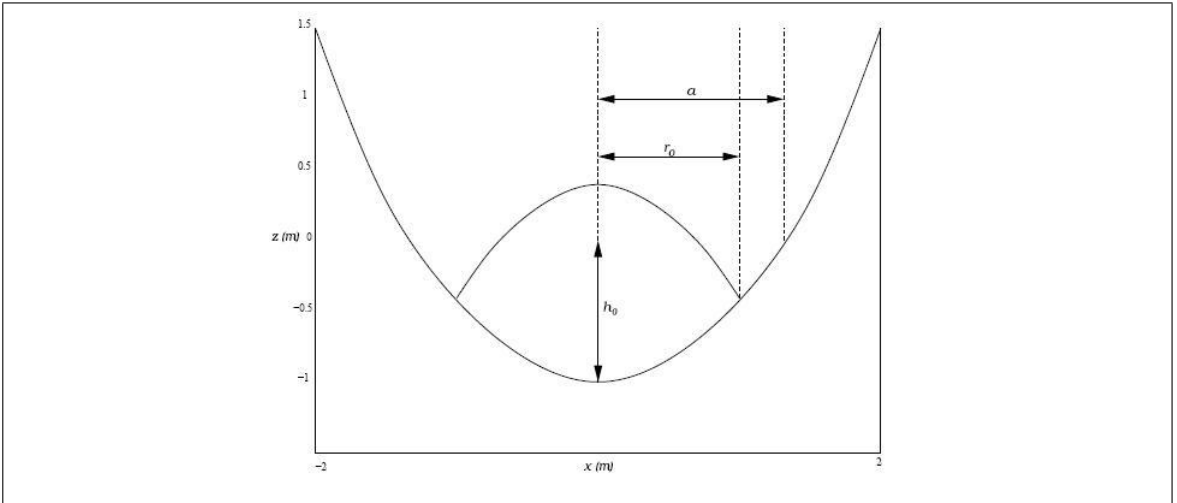


FIGURE H.10. Thacker's curved solution: Geometry of the problem, Marche et al. (2007)

where the angular frequency ω is defined as $\omega = \sqrt{8gh_0/a^2}$, r is the distance from the center, r_0 is the distance from the center to the initial shoreline and $A = (a^2 - r^2)/(a^2 + r^2)$. The initial conditions are defined by the analytical solution at time 0. The chosen parameters for this case are: $a = 1$, $r_0 = 0.8$ m and $h_0 = 0.1$ m. The domain is 4 m x 4 m, and it was discretized using a uniform and regular mesh of 400x400 cell of size $\Delta x = \Delta y = 0.01$ m.

Fig. H.11 shows free surface profile comparisons between analytical and numerical solution at different times for the center line of the parabolic basin in the x direction. Excellent agreement is obtained after three oscillation periods. The oscillations remain periodical and the amplitude do not decay in time, the *run-up* and *rundown* process is correctly represented.

In Fig. H.12 a zoom view of the free surface at the moving shoreline is shown. Small differences and oscillations are found, but the model is capable of eliminate them and they do not propagate.

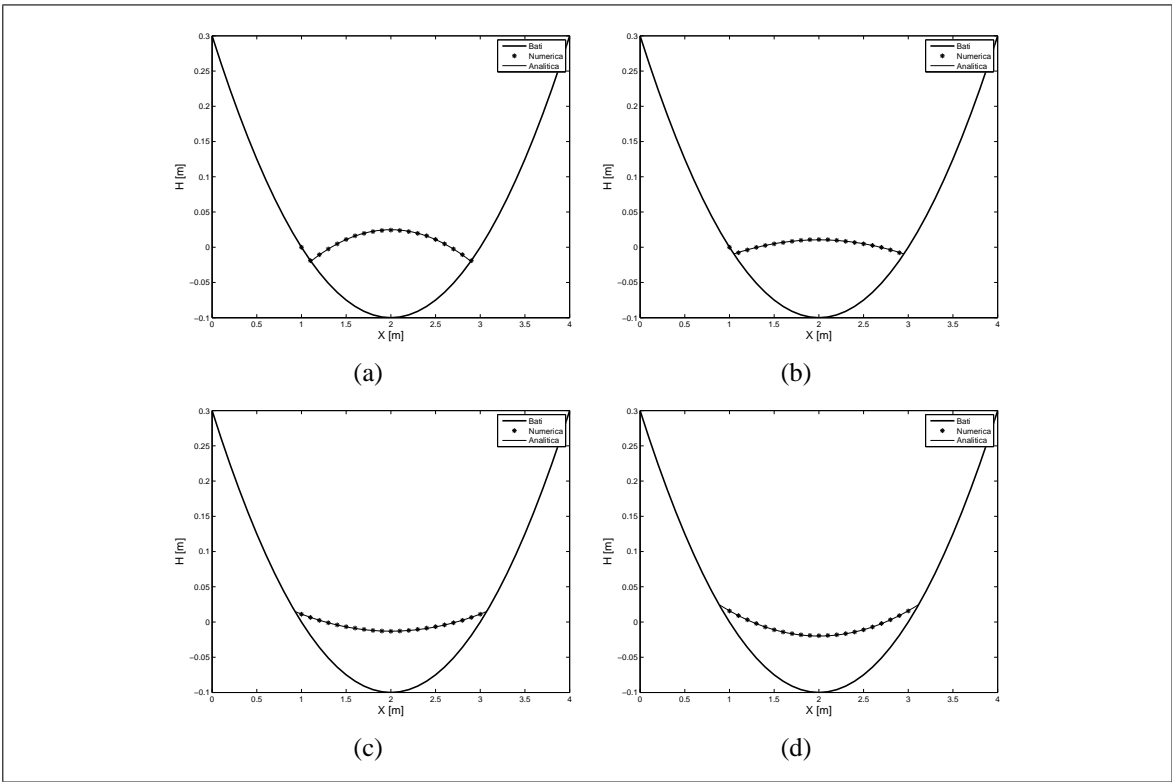


FIGURE H.11. Thacker's curved solution: Numerical and analytical solutions of the free surface in the center line of the basin at times: (a) $3T$, (b) $3T+T/6$, (c) $3T+T/3$, (d) $3T+T/2$

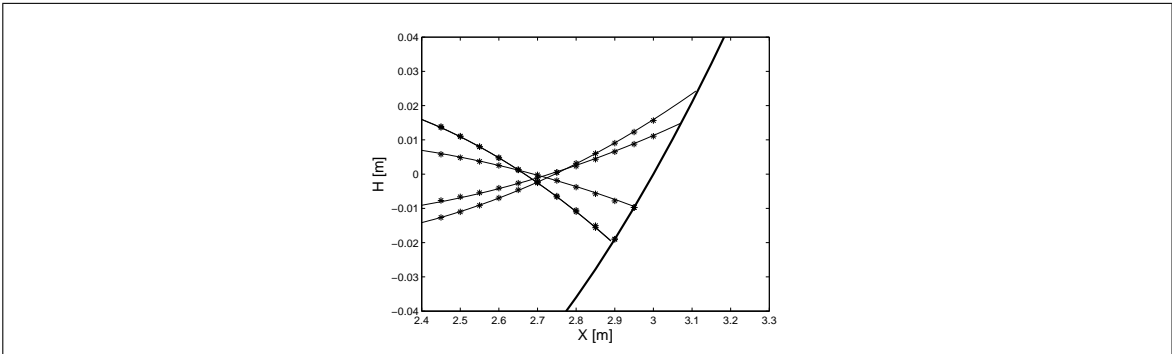


FIGURE H.12. Thacker's curved solution: Zoom view of the shoreline